

Diss. ETH No. 23067

Shape Sensitivity Analysis of Electromagnetic Scattering Problems

A thesis submitted to attain the degree of

DOCTOR OF SCIENCE of ETH ZURICH
(Dr. sc. ETH Zurich)

presented by

Sahar Sargheini

MSc, University of Tehran, Iran
born September 8, 1984
citizen of Iran

accepted on the recommendation of
Prof. Dr. C. Hafner, examiner
Prof. Dr. R. Hiptmair, co-examiner
Prof. Dr. L. Nannen, co-examiner

2016

Acknowledgments

This dissertation is written as a result of scientific research conducted at Seminar for applied Mathematics (SAM) and Institute of Electromagnetic Fields (IEF) of Swiss Federal Institute of Technology Zurich (Eidgenössische Technische Hochschule Zürich, ETH). The work was funded by ETH Grant CH1-02 11-1.

First of all, I would like to thank my supervisor and co-supervisor, Prof. Dr. Christian Hafner and Ralf Hiptmair for accepting me as a doctoral student, for their trust and for their continuous motivation. Furthermore, I am very grateful to Prof. Dr. Lothar Nannen for agreeing to be my co-examiner.

I would also like to thank my colleagues at SAM and IEF who made the years of my doctoral studies a great experience. I was very lucky to have three kind office mates, Alberto, Laura, and Pegah who always involved me in fruitful discussions and never rejected my interruptions to ask questions. I also would like to thank Somayeh, Cecilia and Elke (also helping me with translating the abstract) for being good friends and for numerous technical and non technical conversations we had.

A very special thanks goes to Michele Marcionelli and other members of ISG group at SAM for their great and continuous effort with IT support. Some times they had to spend hours on installing and updating software that I needed during my PhD.

Last but not least, I would like to thank my parents, my brother Ehsan, my sister in Law Bahar and My husband Araz for their unconditional support and kindness. Without their love and understanding I would not have made it this far.

April 2016

Sahar Sargheini

Abstract

Nano particles play a very significant role in the field of optics. Because of their small size, highly localized fields can be obtained. The interaction of light with metallic nano particles exhibits a unique phenomenon called plasmonic resonances, which is due to the coherent oscillation of free electrons. Thanks to advances in manufacturing methods, plasmon resonances have found many applications such as second harmonic generation and sensors. However, investigating them numerically is not straight forward. Due to their small size in comparison to the wavelength, local refinement is essential. Another issue is the dispersive material of nano particles. Dependency of optical constants on the frequency, makes time domain methods rather complicated. In this dissertation, we use finite element method (FEM) to solve Maxwell's equations in frequency domain. Using finite element method, one can simply apply local refinements. And, since it is a frequency domain approach, we can use it to model dispersive materials.

The performance of nano particles is measured using different techniques. One of the most popular measurement quantities is the light intensity at far distances. Far field can also be computed numerically. Since finite element method provides solutions for electromagnetic fields only within a limited domain around the scatterer, one needs to use Near-field to far-field mapping techniques to obtain field values at far distances. For structures located in free space, there are well known methods to evaluate the far field. In the presence of a substrate the far-field functional consists of different asymptotic terms including surface waves. In Chapter 2, we investigate all contributions closely and show that the spherical wave is the only important term at far distances. A closed form representation is given based on the Green's function of a dipole over a half space. The far-field functional is stated in terms of both volume and boundary integrals. When finite element methods are used to solve Maxwell's equations approximately, the volume-

based expression is more accurate than the boundary integral. We confirm the validity of our results by performing several numerical experiments and compare them with other numerical and experimental results.

Despite the rapid progress in the field of nano particles, they have not yet been very successful in commercialization due to losses and high sensitivity of plasmonic particles to fabrication based perturbations. Nano particles are always subject to defects which can significantly affect their behavior. Thus, it is important to know how much the performance of the particle is sensitive to changes in the shape. To study the sensitivity of the far-field pattern or of any other output functional which describes the performance of plasmonic nano-particles with respect to shape perturbations, one needs to perform shape sensitivity analysis. Shape sensitivity analysis is based on evaluating the shape gradient of the output functional with respect to the shape. Shape functionals in electromagnetic problems, e.g. the far-field pattern, depend on the shape of the domain and are constrained by Maxwell's equations. As discussed in Chapter 3, shape gradients of PDE constrained shape functionals can be stated in two equivalent ways. Both rely on solutions of state and adjoint boundary value problems (BVPs). One involves integrating their traces on the boundary of the domain, while the other one evaluates integrals over the volume. Since constraints in electromagnetic problems are vector fields, the procedure of evaluating shape gradients gets rather complex.

Usually, the state and adjoint problems can only be solved approximately, for instance, by finite element method. However, when used with finite element solutions, the equivalence of the two formulations of shape gradient, i.e. the volume form integral and the boundary form integral, breaks down. In Chapter 3, we proved that volume based expressions enjoy faster convergence rates than boundary integrals in a finite element setting. We also established some numerical experiment to confirm this statement.

In Chapter 4, we investigate how local perturbations affect the performance of nano-particles. So, we employ cubic B-splines to represent local deformations of the structure, and derive sensitivity probings over the surface of the scatterer. We also define a sensitivity representative function over the surface of the scatterer based on local sensitivity measurements. Several numerical experiments are conducted to investigate the shape sensitivity of different output functionals for different geometry settings.

Zusammenfassung

Nanopartikel spielen eine wichtige Rolle in der Optik. Aufgrund ihrer geringen Grösse können stark lokalisierte Felder erzeugt werden. Durch die Wechselwirkung von Licht mit metallischen Nanopartikeln wird das einzigartige Phänomen der plasmonischen Resonanzen hervorgerufen. Der Grund für dieses Phänomen liegt in der kohärenten Oszillation von freien Elektronen. Dank der Fortschritte bei Herstellungsprozessen werden plasmonische Resonanzen mittlerweile an vielen Orten eingesetzt. Zur Anwendung kommen sie zum Beispiel bei Frequenzverdopplungen und Sensoren. Dennoch ist die numerische Berechnung von plasmonischen Resonanzen anspruchsvoll. Aufgrund der kleinen Grösse der Partikel im Vergleich zur Wellenlänge sind lokale Verfeinerungen unumgänglich. Eine weitere Schwierigkeit stellt das dispersive Material der Nanopartikel dar. Die Frequenzabhängigkeit optischer Konstanten macht Methoden im Zeitbereich zu einer komplizierten Angelegenheit. In der vorliegenden Dissertation verwenden wir Finite Elemente Methoden (FEM) zur Lösung der Maxwell-Gleichungen im Frequenzbereich. Ein Vorteil der Verwendung von FEM ist die einfache Umsetzbarkeit lokaler Verfeinerungen. Die Betrachtung im Frequenzbereich ermöglicht die Modellierung dispersiver Materialien.

Die Güte von Nanopartikeln wird durch verschiedene Techniken gemessen. Eine der gängigsten Messgrössen ist die Lichtintensität in grosser Distanz, genannt Fernfeld. Das Fernfeld kann auch numerisch berechnet werden. Da mit FEM das elektromagnetische Feld nur innerhalb einer kleinen Umgebung um den Streukörper herum berechnet werden kann, werden Transformationstechniken vom Nah- auf das Fernfeld benötigt, um Auswertungen in grosser Distanz zu ermöglichen. Für Strukturen im freien Raum gibt es etablierte Auswertungsmethoden für das Fernfeld. Das Fernfeldfunktional besteht bei vorhandenem Substrat aus verschiedenen asymptotischen Termen, einschliesslich Oberflächenwellen. Im zweiten Kapitel betrachten wir die einzelnen Terme eingehend und zeigen, dass nur die Beiträge der

sphärischen Welle zum Fernfeld beitragen. Eine geschlossene Darstellung dieses Beitrages lässt sich basierend auf der Greenschen Funktion eines Dipols über einem Halbraum herleiten. Das Fernfeldfunktional besteht aus Volumen- sowie Randintegralen, wobei der volumenbasierte Ausdruck durch FEM genauer approximiert wird als der randwertbasierte. Wir bestätigen die Gültigkeit unseres Ansatzes anhand mehrerer numerischer Experimente und vergleichen die Resultate mit anderen Methoden sowie experimentellen Messungen.

Trotz der schnellen Fortschritte der Nanopartikelforschung konnten Nanopartikel bisher nicht erfolgreich kommerziell eingesetzt werden. Grund dafür sind Verluste beim Herstellungsprozess und die hohe Sensitivität von plasmonischen Partikeln gegenüber geringen Fabrikationsabweichungen. Nanopartikel unterliegen stets gewissen Störungen, welche ihr Materialverhalten stark beeinflussen. Deshalb ist es wichtig bestimmen zu können, welche Auswirkungen Veränderungen der Form des Partikels haben. Um die Sensitivität des Fernfeldes oder anderen Ausgabefunktionalen untersuchen zu können, muss eine Formsensitivitätsanalyse durchgeführt werden. Formsensitivitätsanalysen basieren auf der Berechnung des Formgradienten des Ausgabefunktionalen. Elektromagnetische Formfunktionale, wie zum Beispiel das Fernfeld, hängen von der Form des Gebietes ab und müssen die Maxwell'schen Gleichungen als Zwangsbedingung erfüllen. In Kapitel 3 zeigen wir, dass Formgradienten von Formfunktionalen mit PDE-Zwangsbedingungen auf zwei verschiedene Arten dargestellt werden können. Diese sind äquivalent und basieren auf Lösungen von state und adjoint Randwertproblemen (RWP). Für eines der RWP ist die Integration der Spur über den Rand des Gebietes vonnöten, während das andere RWP ein Volumenintegral beinhaltet. Da sich Zwangsbedingungen in elektromagnetischen Fragestellungen auf Vektorfelder beziehen, ist die Auswertung des Formgradienten aufwendig.

Im Allgemeinfall können die Lösungen der state und adjoint RWP nur näherungsweise bestimmt werden, zum Beispiel mit FEM. Dennoch müssen die beiden Darstellungsformen für den Formgradienten, genauer gesagt die Darstellung über das randbasierte bzw. das volumenbasierte Integral, für die diskretisierte FEM Lösung nicht mehr zwangsläufig äquivalent sein. In Kapitel 3 zeigen wir, dass die volumenbasierte Formel im Zusammenhang mit FEM zu höheren Konvergenzraten führt als die randbasierte Iden-

tität. Weiter führen wir numerische Experimente durch, welche den Beweis bestätigen.

In Kapitel 4 untersuchen wir den Einfluss von lokalen Störungen auf die Eigenschaften von Nanopartikeln. Wir verwenden kubische B-Splines um die lokalen Deformationen der Struktur zu beschreiben und erhalten Sensitivitätsmessungen auf der Oberfläche des Streukörpers. Weiter definieren wir eine repräsentative Sensitivitätsfunktion auf dessen Oberfläche, basierend auf lokalen Sensitivitätsmessungen. In mehreren numerischen Experimenten untersuchen wir die Formsensitivität verschiedener Ausgabefunktionale für diverse Geometrien.

Contents

1	Introduction	1
1.1	Maxwell's equations and weak forms	6
1.2	Outline of the dissertation	9
2	Far field investigation in the presence of substrate	11
2.1	Introduction	11
2.2	Basics	12
2.2.1	Potentials	12
2.2.2	Green's functions	13
2.2.2.1	Dipole in free space	14
2.2.2.2	Dipole over a semi-infinite surface	19
2.2.3	Branch cuts	23
2.3	Asymptotic analysis	26
2.3.1	saddle	29
2.3.2	Branch point contribution	31
2.3.3	Pole contribution	32
2.3.4	Integration end point contribution	35
2.3.5	Discussion	35
2.4	Far-field closed form	37
2.5	NGSolve implementation	42
2.6	Numerical results	49
2.6.1	Dipole over a substrate	49
2.6.2	Nanoparticle over a substrate	53
3	Shape Gradient: Evaluation and Approximation	59
3.1	Introduction	59
3.2	Shape gradients	60

3.3	Derivation of shape gradient	62
3.3.1	Scalar problems	62
3.3.2	Electromagnetic shape functional	70
3.4	Approximation of shape gradients	79
3.4.1	Scalar Problem	79
3.4.2	Maxwell problem	80
3.5	Numerical experiments	95
4	Sensitivity analysis for scattering problems	103
4.1	Introduction	103
4.2	Numerical Approximation of the Shape Gradient	104
4.3	Function Representative of the Shape Gradient	106
4.4	NGSolve implementation	107
4.5	Numerical results	112
4.5.1	Nano antenna consisting two gold spheres	112
4.5.2	Nano antenna consisting two rectangular blocks in free space	114
4.5.3	Nano antenna consisting two rectangular blocks over a substrate	116
4.5.4	Nano antenna consisting two rectangular blocks with displaced arms	117
4.5.5	Nano antenna consisting two rectangular blocks with gap along the longer edge	117
4.5.6	Groove antenna	118
4.5.7	Silver brick	119
4.6	Conclusion	123
5	Conclusion	125
5.1	Summary	125
5.2	Outlook	126
	Bibliography	135
	Curriculum Vitae	143

1 Introduction

Optics is the science of light and vision. Several optical devices such as mirrors, lenses, and prisms have been known and used since ancient times. It is said that Archimedes used giant mirrors to set fire to Romans ships in 212 B.C. [36]. Nero, the Roman Emperor, watched fights of gladiators through a lens magnifier [19]. Another interesting historic report of optical instruments is the Lycurgus cup [26]. The cup which is a Roman glass cup, shows different colors under the illumination of light (see Figure 1.1).

The behavior of most of the ancient optical devices was first explained by



Figure 1.1: Lycurgus cup (British Museum [26]) which is made by adding nano particles of gold and silver to the glass. Due to the interaction of light with tiny metal nano particles, the color of the glass changes under the natural light illumination.

Euclid in 300 B.C. [19, 36]. He stated that light travels along straight lines and will reflect from a smooth surface. His theory is known as basics of geometrical optics.

Geometrical optics was expanded by several scientists until the 17th century [44]. In 1670, Issac Newton proposed that light could be made of particles called corpuscles, i.e. light is composed of colored particles which can be separated using a prism. In his book on optics [52], he considered various concepts for describing the light, and also strongly improved the Euclid's concept. Newton's theorem was not accepted right away and there were criticisms. In 1690, Huygens proposed the wave behavior of light. He

1 Introduction

claimed that when light hits a surface, every point on the surface behaves like a point source emitting spherical wave [1]. Since he considered some sort of longitudinal scalar waves, he was not able to explain effects, e.g. polarization, that could be explained by Newton's optics.

Although various theories of Newton, Huygens and others could explain several effects and were useful constructing optical instruments, interesting observations such as Lyncurgus cup remained unexplained. In 1831, Michael Faraday introduced the electromagnetic field concept and found the law of electromagnetic induction [20]. In 1865, a Scottish mathematician, James Clerk Maxwell summarized Faraday's work in terms of mathematical formulas [45]. He showed that electromagnetic waves travel at the same speed as light, which means the light is also an electromagnetic wave. This phenomenon led to using radio frequency (RF) waves. Radio waves which are in the 3KHz-300GHz frequency range are mostly used for communication and broadcasting purposes. Several instruments, such as radio antennas, are used to send and receive RF waves. Still for large RF devices, one can use ray optics, but in resonance areas a study based on Maxwell's equations is unavoidable.

By rapid progress of technology, the need for higher data rates of communication revived the topic of optics. In 1966, optical fibers were first proposed by George Hockham from England based on the idea of total internal reflection [31]. In the field of optical imaging, however, classical optical instruments like lenses, microscopes, and telescopes were still suffering from the diffraction limit of resolution which is typically around half a wavelength. The diffraction limit exists as long as only the far-field behavior of the device is considered. Due to the existence of evanescent fields in the vicinity of an object, one can obtain more information in the near-field region. Based on this, a new era in Near-field scanning techniques started. The initial idea was proposed by Edward Hutchinson Synge in 1928 [67]. In 1972, Ash and Nicholas made the first scanning near field microscope using an electromagnetic wave with the wavelength of 3cm [5]. The first optical scanning near field microscope was patented by Pohl in 1984 [58]. To improve the performance of the near field microscopy, substantial field localization in the near field is needed. Near-field enhancement can be tuned by manipulating the shape and the material properties of particles.

Dielectric materials can exhibit high resonances when they are illuminated by light. The size of resonant dielectric particles is around half a wavelength. Much smaller particle size and consequently higher resolution can be achieved using metal nano particles.

Metal nano particles, can exhibit a very interesting phenomenon called plasmonic resonances. Plasmon resonances are due to the coherent oscillation of free electrons in the metal with the electromagnetic field. The behavior of the Lycurgus cup can be explained by this phenomenon. Within the glass of the cup, there are tiny sparkles of gold and silver which interact with light and exhibit plasmonic resonance effects.

The strange behavior of metals under the illumination of light remained unexplained until the 20th century. In 1902, an American physicist, Robert William Wood, observed a pattern of dark and light bands when shining polarized light on a metal-backed grating [74, 75]. Later in 1952, there were more experiments by Bohm and Pines on collective oscillations of free electrons in metals [8–10].

Matel nano particles can also be used as antennas. Similar to classical antennas, nano antennas are metal particles which are resonating. However, there are important differences between classical and plasmonic antennas. The main difference is the size. Plasmonic antennas can be much smaller than half a wavelength, whereas in classical antennas the size is around $\lambda/2$ for obtaining a good performance. The second difference arises from the fact that metals like gold and silver show plasmon resonances in a limited frequency range. Within the plasmon resonance spectra, metals are dispersive materials rather than a perfect electric conductor (PEC), i.e. their material properties depend on the frequency. Due to dispersive material properties, plasmonic nano antennas are not scalable. Consequently, the system of Maxwell's equations must be solved for each frequency.

Deriving simple formulas for the design of plasmonic antennas, similar to those in classical antenna books, is not possible. Numerical methods must be used to approximate the solution. There are two main categories of numerical methods for computational electromagnetics: time domain and frequency domain. Since the material properties are strongly frequency dependent in plasmonic particles, frequency domain approaches are more suitable.

There are several frequency domain methods like finite elements method

1 Introduction

(FEM) [48], method of moments (MoM) [30], boundary elements method (BEM) [66], and multiple multipole method (MMP) [4]. For optical nano particles, FEM is one of the most promising methods due to the following reasons

- Curved elements,
- Local mesh refinement,
- higher order finite elements,
- hp refinement.

In this dissertation we use FEM both in 2D and 3D to solve Maxwell's equations. In 2D we use Lehrfem which is a home made library of Seminar of Applied Math department at ETH, and it is based on Matlab. In 3D we use NGSolve developed by Joachim Schoeberl at Vienna University of Technology ¹. NGSolve is an open source C++ library. We developed our routines for far-field and shape sensitivity analysis based on NGSolve.

As mentioned before, the behavior of optical nano particles is highly dependent on their shape. Recent developments in nano fabrication, such as electron beam lithography (EBL) and focused ion beam (FIB) enable us to have good control over the shape of the fabricated structure. In EBL a focused beam of electrons are used to draw a specific pattern on the structure either by direct milling or through forming a mask and lithography techniques. FIB techniques use beams of ions which are accelerated and deflected in order to remove material on specific locations of the sample directly without using mask or a resist in order to pattern the substrate [60]. However, there are still production based perturbations which are inevitable. Figure 1.2, taken from PhD dissertation of Takumi Sannomia [59], shows SEM images of four fabricated particles from different angle and compares them with the original structure. The SEM images reveal how fabrication process introduces perturbations to the particle.

To study the effect of domain variations on the performance of the structure, one needs to perform sensitivity analysis [21–23, 63]. This can be don

¹<http://sourceforge.net/projects/ngsolve>

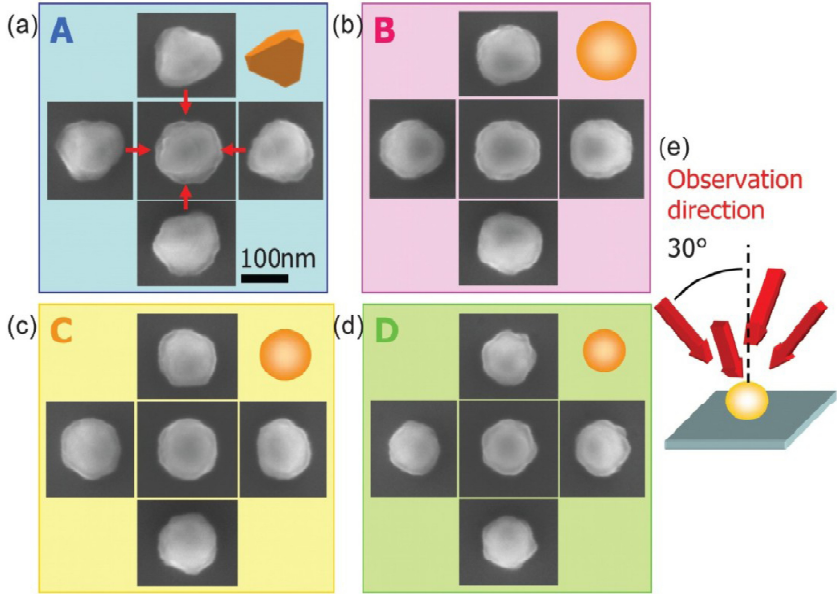


Figure 1.2: Magnified SEM images of four particles with different observation angles [59].

by calculating the shape gradient of a certain output functional. The output functional measures a physical quantity of the problem. In the case of nano optics, the performance of a structure is often studied using far-field measurements. In literature, the far field analysis is usually preformed for structures surrounded by air for the reason of simplicity. However, nanoparticles are mounted on a substrate in most cases. At optical frequencies, one cannot neglect the impact of the substrate on the performance of a nano antenna. In this dissertation, the far-field formula is derived in the presence of a substrate and contributions of different terms on the field at far distances are discussed. We also discussed derivation of shape gradients for Maxwell far-field pattern. The obtained expression is used to investigate the shape sensitivity of several optical nano particles

1.1 Maxwell's equations and weak forms

The optical properties of nano particles are described by Maxwell's equations [45]

$$\begin{aligned}
 \nabla \times \mathbf{e}(\mathbf{r}, t) &= -\partial_t \mathbf{b}(\mathbf{r}, t), \\
 \nabla \times \mathbf{h}(\mathbf{r}, t) &= \partial_t \mathbf{d}(\mathbf{r}, t) + \mathbf{j}(\mathbf{r}, t), \\
 \nabla \cdot \mathbf{b}(\mathbf{r}, t) &= 0, \\
 \nabla \cdot \mathbf{d}(\mathbf{r}, t) &= \rho_e(\mathbf{r}, t),
 \end{aligned} \tag{1.1}$$

where $\mathbf{e}(\mathbf{r}, t)$ and $\mathbf{h}(\mathbf{r}, t)$ represent the electric and magnetic fields at time t and position $\mathbf{r} = (x, y, z)$ in the space. We further introduce the electric flux density $\mathbf{d}(\mathbf{r}, t)$, the magnetic flux density $\mathbf{b}(\mathbf{r}, t)$, the electric current density $\mathbf{j}(\mathbf{r}, t)$, and the scalar electric charge density $\rho_e(\mathbf{r}, t)$.

In the simple case of linear, time independent, homogeneous, and isotropic materials (without chirality), material equations (also known as constitutive relations) are used to couple the system of equations above

$$\begin{aligned}
 \mathbf{d}(\mathbf{r}, t) &= \epsilon \mathbf{e}(\mathbf{r}, t), \\
 \mathbf{b}(\mathbf{r}, t) &= \mu \mathbf{h}(\mathbf{r}, t), \\
 \mathbf{j}(\mathbf{r}, t) &= \mathbf{j}_i(\mathbf{r}, t) + \sigma \mathbf{e}(\mathbf{r}, t),
 \end{aligned} \tag{1.2}$$

where ϵ , μ , and σ are the permittivity, permeability, and electric conductivity of the material, respectively. The impressed current density is denoted by $\mathbf{j}_i(\mathbf{r}, t)$.

All field components are assumed to exhibit a harmonic dependency on time. Then, time harmonic fields are introduced as

$$\mathbf{f}(\mathbf{r}, t) = \text{Re}(\mathbf{F}(\mathbf{r}, \omega) \exp(-i\omega t)), \tag{1.3}$$

where ω is the angular frequency, and $\mathbf{F}(\mathbf{r}, \omega)$ is a time harmonic field. Maxwell's equations for a piecewise constant material can then be rewritten in frequency domain in terms of time harmonic fields

$$\nabla \times \mathbf{E}(\mathbf{r}) = i\omega\mu(\mathbf{r}) \mathbf{H}(\mathbf{r}), \tag{1.4}$$

$$\nabla \times \mathbf{H}(\mathbf{r}) = -i\omega\epsilon_c(\mathbf{r}) \mathbf{E}(\mathbf{r}) + \mathbf{J}_i(\mathbf{r}), \tag{1.5}$$

$$\nabla \cdot (\mu(\mathbf{r}) \mathbf{H}(\mathbf{r})) = 0, \quad (1.6)$$

$$\nabla \cdot (\epsilon(\mathbf{r}) \mathbf{E}(\mathbf{r})) = -\frac{i}{\omega} \nabla \cdot \mathbf{J}_i(\mathbf{r}), \quad (1.7)$$

where $\epsilon_c = \epsilon + i\frac{\sigma}{\omega}$, i.e. the conductivity is included in a complex permittivity ϵ_c . For the reason of simplicity we henceforth write only ϵ which can be real or complex. Note that, in optics μ is usually real and equal to the permeability of free space μ_0 .

By coupling (1.4) and (1.5), the second order Maxwell system is obtained as follows

$$\nabla \times \nabla \times \mathbf{E} - k^2(\mathbf{r})\mathbf{E} = i\omega\mu\mathbf{J}_i, \quad (1.8)$$

where $k^2(\mathbf{r}) := \omega^2 \epsilon(\mathbf{r}) \mu$ is the wavenumber.

In scattering problems, the excitation occurs via an incident field \mathbf{E}_i , which means there are no impressed currents $\mathbf{J}_i = 0$. The scatterer is a bounded domain Ω_s with a Lipschitz boundary $\partial\Omega_s$. The incident field is a solution of the Maxwell's equations in the domain outside the scatterer. A typical example for the incident field in the free space is a plane wave

$$\mathbf{E}_i = \mathbf{p}_i e^{i\mathbf{k}_i \mathbf{r}}, \quad (1.9)$$

where \mathbf{p}_i and \mathbf{k}_i are the polarization and the wavevector of the incident field, respectively ($|\mathbf{k}_i| = k_0$ the wavenumber of free space).

The total electric field consists of the incident field \mathbf{E}_i and the scattered field \mathbf{E}_s

$$\mathbf{E} = \mathbf{E}_s + \mathbf{E}_i. \quad (1.10)$$

The final form of the boundary value problem (BVP) for the scattering problem is

$$\begin{cases} \nabla \times \nabla \times \mathbf{E} - k^2(\mathbf{r})\mathbf{E} = 0 & \mathbf{r} \in \mathbb{R}^3, \\ \llbracket \gamma_t(\mathbf{E}) \rrbracket = 0 & \mathbf{r} \in \partial\Omega_s, \\ \llbracket \gamma_t(\nabla \times \mathbf{E}) \rrbracket = 0 & \mathbf{r} \in \partial\Omega_s, \\ ((\nabla \times \mathbf{E}_s) \times \hat{r} - ik(\mathbf{r}) \mathbf{E}_s) = 0 & r \rightarrow \infty, \end{cases} \quad (1.11)$$

1 Introduction

where $r = |\mathbf{r}|$, $\hat{r} = \frac{\mathbf{r}}{r}$, and γ_t is the tangential trace [48, Page 57]. By $[[\cdot]]$ we denote the discontinuity across the interface $\partial\Omega_s$. The condition on the scattered field at infinity is called Silver Müller radiation condition [49].

To solve the frequency domain Maxwell's equations (1.11) using finite elements method, one needs to derive the variational form which is the stationary point of variational integrals. Since energy integrals are defined within a bounded domain, we define the domain Ω with a boundary $\partial\Omega$ such that $\Omega_s \subset \Omega := \{\mathbf{r} \in \mathbb{R}^3 : |\mathbf{r}| < R\}$, where $R > 0$ (see Figure 1.3). The natural function space for the electric field within domain Ω is $\mathbf{E} \in H(\text{curl}; \Omega)$ [48, Sec. 4.1].

The variational formulation of (1.11) is obtained by testing (1.11) with a function $\mathbf{W} \in H(\text{curl}; \Omega)$ and finding $\mathbf{E} \in H(\text{curl}, \Omega)$ as the solution to

$$\begin{aligned} \int_{\Omega} \nabla \times \mathbf{E} \cdot \nabla \times \overline{\mathbf{W}} - k^2(\mathbf{r}) \mathbf{E} \cdot \overline{\mathbf{W}} \, d\mathbf{r} \\ = \int_{\partial\Omega} ((\nabla \times \mathbf{E}) \times \hat{n}) \cdot \overline{\mathbf{W}} \, ds(\mathbf{r}) \quad \forall \mathbf{W} \in H(\text{curl}, \Omega), \end{aligned} \quad (1.12)$$

where $\overline{\mathbf{W}}$ is the complex conjugate of \mathbf{W} . By \hat{n} , we denote the unit vector outward normal to $\partial\Omega$.

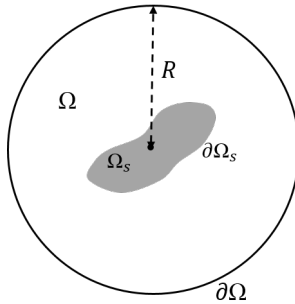


Figure 1.3: Domain definition for the scattering problem.

The boundary integral on the right hand side of (1.12) is not well defined on the finite element space. To fix this issue, the Dirichlet-to-Neumann

(DtN) operator (also named Calderon Map) is used [48, Ch. 9, Sec. 4]

$$\begin{cases} \text{DtN} : H^{-1/2}(\text{Div}; \partial\Omega) \rightarrow H^{-1/2}(\text{Div}; \partial\Omega), \\ \mathbf{g} \mapsto (\nabla \times \mathbf{E}_{\text{out}}) \times \hat{n}, \end{cases} \quad (1.13)$$

where \mathbf{E}_{out} denotes the electric field outside of Ω , i.e., it solves the exterior Dirichlet problem for the second order Maxwell's equation in the region $\{\mathbf{r} \in \mathbb{R}^3 : |\mathbf{r}| > R\}$ with $\hat{n} \times \mathbf{E}_{\text{out}}|_{\partial\Omega} = \mathbf{g}$. Substituting DtN in (1.12), we have

$$\begin{aligned} & \int_{\Omega} \nabla \times \mathbf{E} \cdot \nabla \times \overline{\mathbf{W}} - k^2(\mathbf{r}) \mathbf{E} \cdot \overline{\mathbf{W}} \, d\mathbf{r} - \int_{\partial\Omega} \text{DtN}[\mathbf{E}] \cdot \overline{\mathbf{W}} \, ds(\mathbf{r}) \\ &= \int_{\partial\Omega} ((\nabla \times \mathbf{E}_i) \times \hat{n}) \cdot \overline{\mathbf{W}} - \text{DtN}[\mathbf{E}_i] \cdot \overline{\mathbf{W}} \, ds(\mathbf{r}) \quad \forall \mathbf{W} \in H(\text{curl}, \Omega). \end{aligned} \quad (1.14)$$

1.2 Outline of the dissertation

In Chapter 2, a thorough investigation of the asymptotic behavior of the far-field functional in the presence of the substrate is presented. The Green's function in free space and in a half space is derived in Section 2.2. It is shown that the Green's function in the presence of a substrate can be obtained using an appropriate superposition of plane wave expansions. Each of the plane waves is reflected and transmitted in the presence of the substrate. The asymptotic form of the Green's function is then obtained at far distances in Section 2.3. It is shown that only spherical waves play a significant role in the far-field values, while surface waves decay exponentially. In Section 2.4, the final far-field functional is formulated in terms of Green's functions. Since volume integrals are better approximated in the finite elements space, we reformulate the far field formula in terms of volume integrals. In Section 2.6, far-field patterns of several plasmonic nano particles are analyzed.

In Chapter 3, the shape sensitivity analysis is discussed. In Section 3.3, shape gradients of 2D and 3D problems are obtained, and it is shown that shape gradients can be represented in terms of both boundary and volume integrals. In the following section, the effect of the finite element discretization on the approximation of shape gradients is discussed. It is shown that

1 Introduction

volume integrals often display a faster convergence than the boundary integrals. The numerical results in Section 3.5 also confirm the theory.

In Chapter 4, the shape sensitivity representative for Maxwell's equations is derived. B-spline basis functions are used to perturb the shape locally. Several numerical experiments are performed to show the sensitivity representative of far-field or near-field measurements. Finally Chapter 5, concludes the dissertation.

2 Far field investigation in the presence of substrate

This Chapter is partly published in SAM-report [35]. Ralf Hiptmair and Christian Hafner contributed in derivation of asymptotic forms and final volume formula.

2.1 Introduction

In many electromagnetic scattering problems, the key quantity of concern is the radiation pattern at far distances. For example, in antenna measurements the receiver is usually located far away from the sender. Numerical methods such as Finite Elements or Finite Differences provide the solution to Maxwell's equations within some finite region of space, i.e. the field inside the computational domain.

Field values at far distances can be obtained using a post-processing procedure called near-field to far-field mapping. This mapping is a linear functional of the near-field solution. Procedures of far-field calculations for structures in free space are well known. However, for structures located above a substrate, calculations are more challenging. There have been many investigations about dipole radiation above a half space [14, 16, 24, 38, 55]. Sommerfeld obtained the first formula for a dipole oriented vertically above a planar and lossy plane [64, 65]. The asymptotic evaluation for source and observation points located near the planar surface revealed the contribution of two terms: spherical waves and surface waves [76]. Sommerfeld claimed that surface waves can be used for long distance radio wave transmission due to their slower radial decay along the Earth's surface. However, considering other contributions to the far-field formula shows that surface waves decay exponentially along lossy interfaces. Sommerfeld's results were the

basis of many other investigations [70, 71, 73].

In this chapter we present an asymptotic analysis for outgoing electromagnetic waves and derive a closed form for the field of a dipole over a substrate at far distances. We generalize the dipole results to derive a final form for the near-field to far-field mapping using the Huygens principle.

Far-field functionals are stated in terms of a boundary integral over a surface surrounding the scatterer. Since boundary integrals are not well-defined on the natural variational space, we reformulate the far-field mapping in terms of a volume integral. Volume integrals are continuous on the energy space of the variational formulation. As a matter of fact, for Galerkin solutions, the formulation with the volume-based expression is more appropriate than boundary-integrals for calculating the far-field functional.

To investigate the validity of our results, we analyze the far-field and the near-field patterns of different structures and compare them with other numerical and experimental results.

2.2 Basics

2.2.1 Potentials

Maxwell's equations in (1.4)-(1.7) comprise of two unknown vector fields. In this section we reduce the number of unknowns to one vector and one scalar field by introducing potentials. The derivation of vector potential is based on the fact that $\mathbf{B}(\mathbf{r})$ is divergence free. A divergence free field can be expressed as the rotation of a vector field $\mathbf{A}(\mathbf{r})$

$$\mathbf{H} = \frac{1}{\mu} \nabla \times \mathbf{A}. \quad (2.1)$$

It can also be shown that:

$$\mathbf{E} = i\omega \mathbf{A} - \nabla \phi_e, \quad (2.2)$$

where $\phi_e(\mathbf{r}) : \mathbb{R}^3 \rightarrow \mathbb{C}$ is a scalar function. \mathbf{A} and ϕ_e are known as vector and scalar potentials of an electric source.

To define unique \mathbf{A} and ϕ_e , we need to put constraints on $\nabla \cdot \mathbf{A}$. We can

use the Lorenz gauge condition as following ([55], [16])

$$\nabla \cdot \mathbf{A} = i\omega\mu\epsilon\phi_e. \quad (2.3)$$

Hence, the electric field can be rewritten as:

$$\mathbf{E} = i\omega \left(\mathbf{A} + \frac{1}{k^2} \nabla (\nabla \cdot \mathbf{A}) \right), \quad (2.4)$$

where, $k^2 = \omega^2\mu\epsilon$ is the wavenumber.

By coupling equations (2.1) and (2.2), using (2.3), one can derive the vector Helmholtz equation for \mathbf{A}

$$\Delta \mathbf{A} + k^2 \mathbf{A} = -\mu \mathbf{J}_i. \quad (2.5)$$

There are three scalar Helmholtz equations embedded in (2.5). One standard technique to solve a second order inhomogeneous partial differential equation such as the scalar Helmholtz equation, is to integrate over the volume of source function using the solution to the point source (which is known as Green's function). In the next section, we will study the Green's function for the scalar Helmholtz equation.

2.2.2 Green's functions

The scalar Green's function g_0 for the scalar Helmholtz equation is obtained by considering a point source at $\mathbf{r}' = (x', y', z')$

$$\Delta g_0(\mathbf{r}, \mathbf{r}') + k^2 g_0(\mathbf{r}, \mathbf{r}') = \delta(\mathbf{r} - \mathbf{r}'). \quad (2.6)$$

Note that the Green's function has to satisfy radiation conditions.

Proposition 1. (*Sommerfeld radiation condition*) *The solution to (2.6) in unbounded free space must fulfill the radiation condition at infinity*

$$\lim_{r \rightarrow \infty} r \left(\frac{\partial g_0}{\partial r} - ik g_0 \right) = 0, \quad (2.7)$$

where $r = |\mathbf{r}|$.

2 Far field investigation in the presence of substrate

As soon as $g_0(\mathbf{r}, \mathbf{r}')$ is known, the vector potential can automatically be obtained by an integration over volume V , where the source term exists

$$\mathbf{A}(\mathbf{r}) = \int_V \mu \mathbf{J}_i(\mathbf{r}') g_0(\mathbf{r}, \mathbf{r}') d\mathbf{r}'. \quad (2.8)$$

The electromagnetic field distribution of an electric dipole oriented in the direction $\hat{\ell}$ ($|\hat{\ell}| = 1$) can be obtained by introducing the vector Green's function $\mathbf{G}_0(\mathbf{r}, \mathbf{r}', \hat{\ell}) = g_0(\mathbf{r}, \mathbf{r}')\hat{\ell}$ and using (2.1) and (2.4), we have

$$\mathbf{G}^{\mathbf{E}}(\mathbf{r}, \mathbf{r}', \hat{\ell}) = i\omega\mu \left(\mathbf{G}_0(\mathbf{r}, \mathbf{r}', \hat{\ell}) + \frac{1}{k^2} \nabla(\nabla \cdot \mathbf{G}_0(\mathbf{r}, \mathbf{r}', \hat{\ell})) \right), \quad (2.9)$$

$$\mathbf{G}^{\mathbf{H}}(\mathbf{r}, \mathbf{r}', \hat{\ell}) = -\nabla \times \mathbf{G}_0(\mathbf{r}, \mathbf{r}', \hat{\ell}),$$

where $\mathbf{G}^{\mathbf{E}}(\mathbf{r}, \mathbf{r}', \hat{\ell})$ and $\mathbf{G}^{\mathbf{H}}(\mathbf{r}, \mathbf{r}', \hat{\ell})$ are electric and magnetic fields observed at $\mathbf{r} = (x, y, z)$ from an electric dipole located at $\mathbf{r}' = (x', y', z')$.

Our main concern in this chapter is the far-field calculation of structures located either in free space or over a semi-infinite dielectric domain. In Section 2.3, it is shown that $\mathbf{G}^{\mathbf{E}}(\mathbf{r}, \mathbf{r}', \hat{\ell})$ is essential for far-field calculations. So, the rest of this section is dedicated to the derivation of Green's functions in free space and half space.

2.2.2.1 Dipole in free space

Theorem 1. *The fundamental solution to (2.6) in free space which has a physical interpretation is [16, Sec. 1.3.4],*

$$g_0(\mathbf{r}, \mathbf{r}') = \frac{\exp(ik|\mathbf{r} - \mathbf{r}'|)}{4\pi|\mathbf{r} - \mathbf{r}'|}. \quad (2.10)$$

Obviously, $g_0(\mathbf{r}, \mathbf{r}')$ satisfies the radiation condition (2.7).

The spatial Fourier transformation of (2.10) in x and y directions in Cartesian coordinate system can be obtained by the Weyl identity [73, Eqn.

1]

$$g_0(\mathbf{r}, \mathbf{r}') = \tag{2.11}$$

$$\frac{i}{8\pi^2} \int_{-\infty}^{+\infty} \int_{-\infty}^{+\infty} \exp(i(k_x(x-x') + k_y(y-y'))) \frac{e^{i k_z(k_x, k_y)|z-z'|}}{k_z(k_x, k_y)} dk_x dk_y,$$

where $\mathbf{k} = (k_x, k_y, k_z)$ is the wave vector such that $|\mathbf{k}| = k$, so $k_z(k_x, k_y) = \sqrt{k^2 - (k_x^2 + k_y^2)}$. The square root makes k_z a double valued number. The standard square root branch cut along the positive real axis is used to treat the double valued numbers (see Section 2.2.3).

In Cartesian coordinates, plane waves $e^{i\mathbf{k}\cdot\mathbf{r}}$ are the solutions of the homogeneous Helmholtz equation. As a matter of fact, (2.11) is usually called the plane-wave expansion of $g_0(\mathbf{r}, \mathbf{r}')$.

To reduce the number of integrals in (2.11), one can use cylindrical waves instead of plane waves. The cylindrical wave expansion of (2.10) is called the Sommerfeld identity [65, Page 242]

$$g_0(\mathbf{r}, \mathbf{r}') = \frac{i}{4\pi} \int_0^{+\infty} k_\rho J_0(k_\rho \bar{\rho}) \frac{\exp(ik_z(k_\rho)|z-z'|)}{k_z(k_\rho)} dk_\rho. \tag{2.12}$$

where $\bar{\rho} = |(x, y) - (x', y')|$, $k_z(k_\rho) = \sqrt{k^2 - k_\rho^2}$, and $J_0(k_\rho \bar{\rho})$ is the zero order Bessel function of the first kind. Similar to (2.11), $k_z(k_\rho)$ is double valued and is the source of branch points at $k_\rho = \pm k$ (see Section 2.2.3). For subsequent applications, it is more useful to have the integration range from $-\infty$ to $+\infty$ in (2.12). For this end, we put

$$J_0(k_\rho \bar{\rho}) = \frac{1}{2} \left(H_0^{(1)}(k_\rho \bar{\rho}) + H_0^{(2)}(k_\rho \bar{\rho}) \right) \tag{2.13}$$

where $H_0^{(1)}(k_\rho \bar{\rho})$ and $H_0^{(2)}(k_\rho \bar{\rho})$ are zero order Hankel functions of the first and the second kind, respectively. Using the change of variables $\hat{k}_\rho = -k_\rho$ and keeping in mind that $H_0^{(2)}(-k_\rho \bar{\rho}) = -H_0^{(1)}(k_\rho \bar{\rho})$, we have

$$\int_0^{+\infty} k_\rho H_0^{(2)}(k_\rho \bar{\rho}) \frac{\exp(ik_z(k_\rho)|z-z'|)}{k_z(k_\rho)} dk_\rho = \tag{2.14}$$

2 Far field investigation in the presence of substrate

$$\int_{-\infty}^0 \hat{k}_\rho H_0^{(1)}(\hat{k}_\rho \bar{\rho}) \frac{\exp(ik_z(\hat{k}_\rho)|z-z'|)}{k_z(\hat{k}_\rho)} d\hat{k}_\rho.$$

Remark 1. *If the range of k_ρ in (2.12) is to be extended to $k_\rho = -\infty$, one must take into account that a branch point singularity at $k_\rho = 0$ arises from the Bessel function. To preserve the integrand single valued in the complex k_ρ plane, we introduce a branch cut along the negative real k_ρ axis (see Figure 2.1).*

Finally, we obtain

$$g_0(\mathbf{r}, \mathbf{r}') = \frac{i}{8\pi} \int_{\bar{P}_\rho} k_\rho H_0^{(1)}(k_\rho \bar{\rho}) \frac{\exp(ik_z(k_\rho)|z-z'|)}{k_z(k_\rho)} dk_\rho. \quad (2.15)$$

By \bar{P}_ρ we denote the integration contour in the complex k_ρ plane as depicted in Figure 2.1. The integration contour is off the negative real axis due to the branch cut of Hankel function.

Remark 2. *Both integrals (2.11) and (2.15) are singular at branch point $k_z = 0$. To keep integrands analytic, the integration contour must avoid singular points. So, \bar{P}_ρ have to go around the branch cut for the sake of analyticity (see Sections 2.2.3 and 2.3.2).*

Remark 3. *The integrals in (2.11) and (2.15) are improper. They will converge only if $\exp(ik_z|z-z'|)$ converges to zero as the integration parameters approach $+\infty$ or $-\infty$. To fulfill this condition, it is necessary to impose $\text{Im } k_z > 0$. In Section 2.2.3, we discuss thoroughly how the selection of branch cuts helps us to keep the imaginary part of k_z always positive along the integration contour.*

The branch cuts in (2.15) can be removed by introducing the complex angle $w \in \mathbb{C}$:

$$k_\rho = k \sin w. \quad (2.16)$$

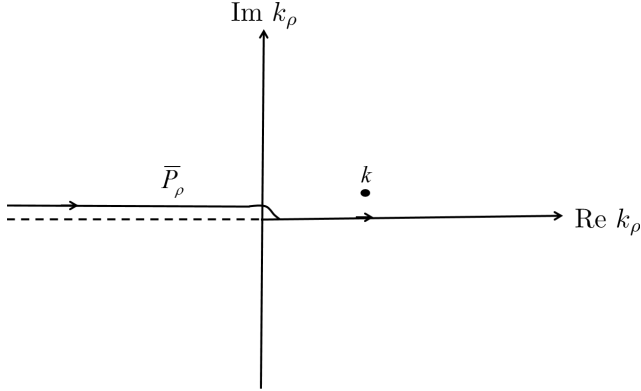


Figure 2.1: Integration contour in the complex k_ρ plane (avoiding singularity of Hankel function).

In Section 2.2.3 it is shown that $k_z(k_\rho)$ is no more double valued in the complex w plane

$$k_z(w) = \pm k \cos w. \quad (2.17)$$

Based on the discussion in Section 2.2.3, at $k_\rho = 0$ we have $k_z = k$. So, we choose $k_z(w) = +k \cos w$ to make $k_\rho = 0$ correspond to $w = 0$.

In terms of w , (2.15) is

$$g_0(\mathbf{r}, \mathbf{r}') = \frac{i k}{8\pi} \int_{\bar{P}_w} \sin w H_0^1(k\bar{\rho} \sin w) e^{(ik_z(w)|z-z'|)} dw, \quad (2.18)$$

where \bar{P}_w is the transformed integration path in the w plane. For real values of k we obtain from (2.16)

$$k_\rho = k(\sin(\operatorname{Re} w) \cosh(\operatorname{Im} w) + i \cos(\operatorname{Re} w) \sinh(\operatorname{Im} w)). \quad (2.19)$$

Thus, \bar{P}_w lies on

$$\operatorname{Im} k_\rho = k \cos(\operatorname{Re} w) \sinh(\operatorname{Im} w) = 0, \quad (2.20)$$

2 Far field investigation in the presence of substrate

which implies the following

$$\begin{cases} \text{If } \operatorname{Im} w = 0 \text{ then } \operatorname{Im} k_\rho = 0 \ \& \ -k \leq \operatorname{Re} k_\rho \leq k, \\ \text{If } \operatorname{Re} w = \frac{\pi}{2} \text{ then } \operatorname{Im} k_\rho = 0 \ \& \ \operatorname{Re} k_\rho \geq k, \\ \text{If } \operatorname{Re} w = \frac{-\pi}{2} \text{ then } \operatorname{Im} k_\rho = 0 \ \& \ \operatorname{Re} k_\rho \leq -k. \end{cases} \quad (2.21)$$

Similar to (2.11) and (2.15), the integral in (2.18) is improper. Consequently, the direction of \bar{P}_w must be chosen in such a way that $\operatorname{Im} k_z(w) > 0$. Using (2.17), one can simply show that $\operatorname{Im} k_z = -k \sin(\operatorname{Re} w) \sinh(\operatorname{Im} w)$ for real values of k . In order to keep the imaginary part of k_z always positive along \bar{P}_w we must have the followings

- If $\operatorname{Re} w = \frac{\pi}{2}$
the contour folds down towards $\operatorname{Im} w < 0$.
- If $\operatorname{Re} w = \frac{-\pi}{2}$
the contour folds up towards $\operatorname{Im} w > 0$.

The final form of \bar{P}_w is shown in Figure 2.2.

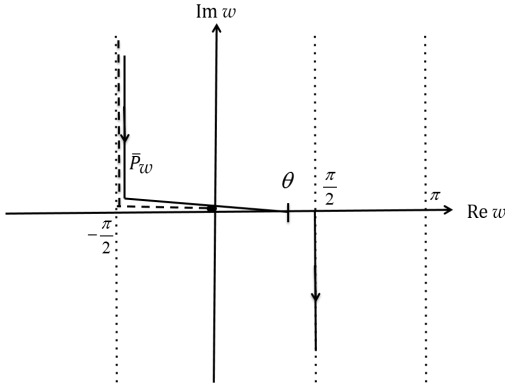


Figure 2.2: Integration contour in the complex w plane, avoiding the branch cut singularity of Hankel function.

2.2.2.2 Dipole over a semi-infinite surface

Figure 2.3 shows a dipole located at \mathbf{r}' over a semi-infinite domain (substrate). $\Omega_1 := \{\mathbf{r} \in \mathbb{R}^3 : z > 0\}$ and $\Omega_2 := \{\mathbf{r} \in \mathbb{R}^3 : z < 0\}$. (ϵ_1, μ_1) and (ϵ_2, μ_2) are the material properties of Ω_1 and Ω_2 , respectively.

Assumption 1. *In this dissertation, we consider non magnetic ($\mu_\alpha =$ permeability of free space μ_0), loss-free ($\text{Im } \epsilon_\alpha = 0$) or lossy ($\text{Im } \epsilon_\alpha > 0$) dielectrics. For the sake of simplicity, we assume $\text{Re } \epsilon_\alpha \geq 0$. $\alpha = 1, 2$ specifies different coefficients for different subdomains Ω_α*

We also introduce $k_1 = n_1 k_0$ and $k_2 = n_2 k_0$ as wavenumbers in Ω_1 and Ω_2 ($k_0 = \omega \sqrt{\epsilon_0 \mu_0}$ is the wavenumber in free space). By $n_1 = \sqrt{\frac{\epsilon_1}{\epsilon_0}}$ and $n_2 = \sqrt{\frac{\epsilon_2}{\epsilon_0}}$ we denote refraction indices of non-magnetic materials.

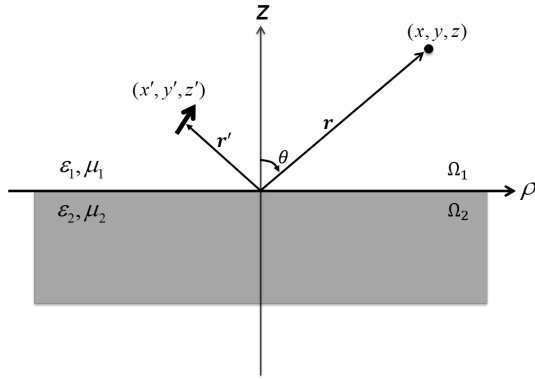


Figure 2.3: Dipole located over a semi-infinite dielectric domain.

The best way to find the solution to (2.6) in the presence of a substrate is to start with the solution in free space. As already mentioned, the integrand in (2.11) is a linear superposition of plane waves. Plane waves in the presence of a semi-infinite dielectric domain can be decomposed into transverse electric (TE) and transverse magnetic (TM) modes [16, Ch.2]. The electric field of a TE mode is perpendicular to the plane of incidence, whereas, the magnetic field of a TM mode is perpendicular to the plane of incidence. The plane of incidence is a plane spanned by vectors \mathbf{k} and \mathbf{n} ,

2 Far field investigation in the presence of substrate

where \mathbf{n} is the unit vector normal to the substrate. In the configuration shown in Figure 2.3 we have $\mathbf{n} = \hat{z}$. We also assume that \mathbf{k} is not parallel to \mathbf{n} .

A TM wave incidence on a half space is depicted in Figure 2.4. The z component of the incident electric field is $E_z^i = E_0 e^{i(k_x x + k_y y - k_{z_1} z)}$. $\mathbf{k}_1 = (k_x, k_y, k_{z_1})$ and $\mathbf{k}_2 = (k_x, k_y, k_{z_2})$ both belong to \mathbb{R}^3 such that $|\mathbf{k}_1| = k_1$ and $|\mathbf{k}_2| = k_2$.

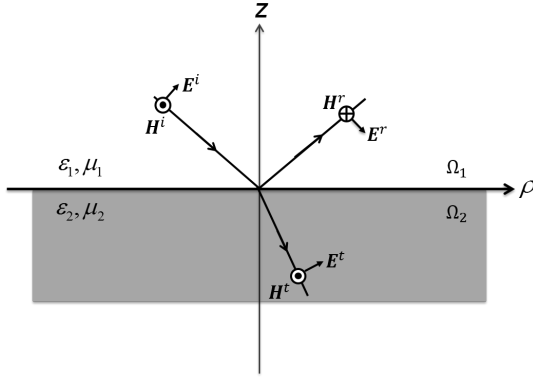


Figure 2.4: TM wave incidence on a semi-infinite dielectric half space. $(\mathbf{E}^i(\mathbf{r}), \mathbf{H}^i(\mathbf{r}))$, $(\mathbf{E}^r(\mathbf{r}), \mathbf{H}^r(\mathbf{r}))$, and $(\mathbf{E}^t(\mathbf{r}), \mathbf{H}^t(\mathbf{r}))$ are the incident, reflected, and transmitted fields, respectively.

Proposition 2. ([55, Sec. 2.8.1]) Consider an incident TM wave over a semi-infinite half space shown in Figure 2.3 with $E_z^i = E_0 e^{i(k_x x + k_y y - k_{z_1} z)}$. Then the longitudinal component of the total field is

$$TM : \begin{cases} E_z(\mathbf{r}) = E_0 e^{i(k_x x + k_y y - k_{z_1} z)} \\ \quad - R^{TM}(k_x, k_y) E_0 e^{i(k_x x + k_y y + k_{z_1} z)} & \mathbf{r} \in \Omega_1, \\ E_z(\mathbf{r}) = T^{TM}(k_x, k_y) E_0 e^{i(k_x x + k_y y - k_{z_2} z)} & \mathbf{r} \in \Omega_2, \\ H_z(\mathbf{r}) = 0 & \mathbf{r} \in \Omega_1 \cup \Omega_2, \end{cases} \quad (2.22)$$

where $R^{TM}(k_x, k_y)$ and $T^{TM}(k_x, k_y)$ are reflection and transmission coefficients of TM modes, respectively

$$\begin{aligned} R^{TM}(k_x, k_y) &= \frac{\epsilon_1 k_{z2} - \epsilon_2 k_{z1}}{\epsilon_1 k_{z2} + \epsilon_2 k_{z1}}, \\ T^{TM}(k_x, k_y) &= 1 + R^{TM}(k_x, k_y). \end{aligned} \quad (2.23)$$

Proposition 3. ([55, Sec. 2.8.1]), Consider an incident TE wave over a semi-infinite half space shown in Figure 2.3 with $H_z^i = H_0 e^{i(k_x x + k_y y - k_{z1} z)}$. Then the longitudinal component of the total field is

$$TE : \begin{cases} E_z(\mathbf{r}) = 0 & \mathbf{r} \in \Omega_1 \cup \Omega_2, \\ H_z(\mathbf{r}) = H_0 e^{i(k_x x + k_y y - k_{z1} z)} \\ \quad + R^{TE}(k_x, k_y) H_0 e^{i(k_x x + k_y y + k_{z1} z)} & \mathbf{r} \in \Omega_1, \\ H_z(\mathbf{r}) = T^{TE}(k_x, k_y) H_0 e^{i(k_x x - k_y y - k_{z2} z)} & \mathbf{r} \in \Omega_2, \end{cases} \quad (2.24)$$

with reflection and transmission coefficients R^{TE} and T^{TE} :

$$\begin{aligned} R^{TE}(k_x, k_y) &= \frac{k_{z1} - k_{z2}}{k_{z1} + k_{z2}}, \\ T^{TE}(k_x, k_y) &= 1 + R^{TE}(k_x, k_y). \end{aligned} \quad (2.25)$$

Note that $k_{z1}(k_x, k_y) = \sqrt{k_1^2 - k_x^2 - k_y^2}$ and $k_{z2}(k_x, k_y) = \sqrt{k_2^2 - k_x^2 - k_y^2}$ both are double valued functions and must be treated using branch cuts (see Section 2.2.3).

In order to expand the field of a dipole oriented in direction $\hat{\ell}$ above a substrate using plane waves, one must choose the correct mode of plane waves. Based on what discussed already the longitudinal component of the electric field of a dipole $\mathbf{G}^E(\mathbf{r}, \mathbf{r}', \hat{\ell}) \cdot \hat{z}$ must be expanded using TM waves, and similarly the longitudinal component of the magnetic field of a dipole $\mathbf{G}^H(\mathbf{r}, \mathbf{r}', \hat{\ell}) \cdot \hat{z}$ must be expanded in terms of TE waves.

Assumption 2. Green's functions derived in this chapter are for dipole located in upper half space, i.e. $\mathbf{r}' \in \Omega_1$. A similar procedure can be used to calculate $g_0(\mathbf{r}, \mathbf{r}')$ for $\mathbf{r}' \in \Omega_2$.

Using (2.11), one can derive the plane wave expansion of the scalar Green's function in the presence of a planar dielectric half space in terms of either TM or TE mode expansion for $|z| > z'$

$$g_0(\mathbf{r}, \mathbf{r}') = \begin{cases} \frac{i}{8\pi} \int_{-\infty}^{+\infty} \int_{-\infty}^{+\infty} \frac{e^{(i(k_x(x-x') + k_y(y-y') + k_{z_1}(k_x, k_y)z))}}{k_{z_1}(k_x, k_y)} & \mathbf{r} \in \Omega_1, \\ \left[e^{(-ik_{z_1}(k_x, k_y)z')} + f(k_x, k_y)e^{(ik_{z_1}(k_x, k_y)z')} \right] dk_x dk_y \\ \frac{i}{8\pi} \int_{-\infty}^{+\infty} \int_{-\infty}^{+\infty} \frac{e^{(i(k_x(x-x') + k_y(y-y') - k_{z_2}(k_x, k_y)z))}}{k_{z_1}(k_x, k_y)} & \mathbf{r} \in \Omega_2, \\ e^{k_{z_1}(k_x, k_y)z'} (1 + f(k_x, k_y)) dk_x dk_y \end{cases} \quad (2.26)$$

where $f(k_x, k_y) = -R^{TM}(k_x, k_y)$ for TM modes, and $f(k_x, k_y) = R^{TE}(k_x, k_y)$ for TE modes.

In terms of cylindrical waves (2.26) for $|z| > z'$ is (derivation procedure is similar to (2.15))

$$g_0(\mathbf{r}, \mathbf{r}') = \begin{cases} \frac{i}{8\pi} \int_{\bar{P}_\rho} \frac{k_\rho H_0^{(1)}(k_\rho \bar{\rho})}{k_{z_1}(k_\rho)} e^{(ik_{z_1}(k_\rho)z)} & \mathbf{r} \in \Omega_1, \\ \left[e^{(-ik_{z_1}(k_\rho)z')} + f(k_\rho)e^{(ik_{z_1}(k_\rho)z')} \right] dk_\rho \\ \frac{i}{8\pi} \int_{\bar{P}_\rho} \frac{k_\rho H_0^{(1)}(k_\rho \bar{\rho})}{k_{z_1}(k_\rho)} e^{-i(k_{z_2}(k_\rho)z)} & \mathbf{r} \in \Omega_2, \\ e^{(i(k_{z_1}(k_\rho)z'))} (1 + f(k_\rho)) dk_\rho \end{cases} \quad (2.27)$$

where $\bar{\rho} = |(x, y) - (x', y')|$, $k_{z_1}(k_\rho) = \sqrt{k_1^2 - k_\rho^2}$ and $k_{z_2}(k_\rho) = \sqrt{k_2^2 - k_\rho^2}$. Double valued functions $k_{z_1}(k_\rho)$ and $k_{z_2}(k_\rho)$ are the sources of branch cuts

at $k_\rho = \pm k_1$ and $k_\rho = \pm k_2$ in both half spaces (see Section 2.2.3). $f(k_\rho)$ is derived in a similar way to $f(k_x, k_y)$ just by considering $k_{z_1}(k_\rho)$ and $k_{z_2}(k_\rho)$ instead of $k_{z_1}(k_x, k_y)$ and $k_{z_2}(k_x, k_y)$, respectively.

In terms of the complex angle w , (2.27) $|z| > z'$ is

$$g_0(\mathbf{r}, \mathbf{r}') = \begin{cases} \frac{i k_1}{8\pi} \int_{\bar{P}_w} \sin w H_0^1(k_1 \bar{\rho} \sin w) e^{(ik_{z_1}(w) z)} \\ \quad \left[e^{(-ik_{z_1}(w) z')} + f(w) e^{(ik_{z_1}(w) z')} \right] dw & \mathbf{r} \in \Omega_1, \\ \frac{i k_2}{8\pi} \int_{\bar{P}_w} \sin w H_0^1(k_2 \bar{\rho} \sin w) e^{(-ik_{z_2}(w) z)} \\ \quad e^{(ik_{z_1}(w) z')} (1 + f(w)) dw & \mathbf{r} \in \Omega_2, \end{cases} \quad (2.28)$$

where

$$\begin{cases} k_{z_1}(w) = +k_1 \cos w \\ k_{z_2}(w) = k_1 \sqrt{\frac{\epsilon_2}{\epsilon_1} - \sin^2 w} \end{cases} \quad \mathbf{r} \in \Omega_1, \quad (2.29)$$

$$\begin{cases} k_{z_1}(w) = k_2 \sqrt{\frac{\epsilon_1}{\epsilon_2} - \sin^2 w} \\ k_{z_2}(w) = -k_2 \cos w \end{cases} \quad \mathbf{r} \in \Omega_2. \quad (2.30)$$

$k_{z_2}(w)$ and $k_{z_1}(w)$ are the origins of branch cuts in Ω_1 and Ω_2 , respectively (see Section 2.2.3). $f(w)$ is derived in a similar way to $f(k_x, k_y)$ just by considering $k_{z_1}(w)$ and $k_{z_2}(w)$ instead of $k_{z_1}(k_x, k_y)$ and $k_{z_2}(k_x, k_y)$, respectively.

2.2.3 Branch cuts

In this section we discuss some issues regarding branch point singularities and branch cuts within integrals (2.27) and (2.28).

2 Far field investigation in the presence of substrate

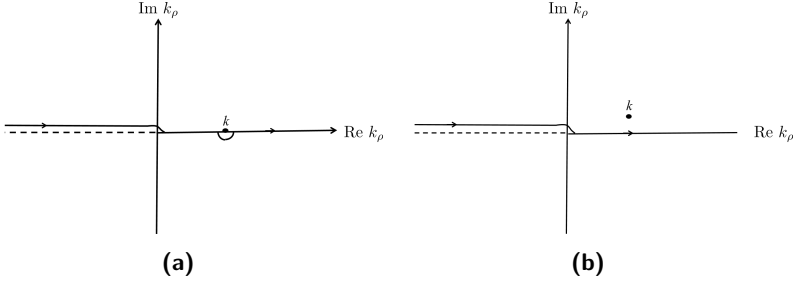


Figure 2.5: Integration path in the complex k_ρ plane for a (a) loss-less (b) lossy material.

The integrand in (2.27) contains branch point singularities at $k_\rho = \pm k_1$ and $k_\rho = \pm k_2$ which arise from $k_{z_1} = \sqrt{k_1^2 - k_\rho^2}$ and $k_{z_2} = \sqrt{k_2^2 - k_\rho^2}$, respectively [2]. In loss-less materials, the branch points in k_ρ plane lie on the integration path. Then the integration path must be displaced around singularities (see Figure 2.5a). By introducing a slight loss in materials, k_1 and k_2 have small positive imaginary parts, thus the branch points are no more on the real axis. Typical integration paths in the complex k_ρ plane for loss-less and lossy materials are shown in Figures 2.5a and 2.5b, respectively.

Branch cuts originating from double valued functions in a complex plane, e.g. k_{z_1} and k_{z_2} , provide a mean to pass from one Riemann sheet to the other [2]. Signs of $\text{Im } k_{z_1}$, and $\text{Im } k_{z_2}$ in different regions of the k_ρ plane depend on Riemann sheet junctions or branch cuts. To ensure the boundedness of integrands in (2.27) when $k_{z_1}|z - z'| \rightarrow \infty$ or $k_{z_2}|z - z'| \rightarrow \infty$, it is necessary to impose conditions $\text{Im } k_{z_1} > 0$ and $\text{Im } k_{z_2} > 0$. As a matter of fact, the boundedness of radiation integrals is closely related to branch cuts.

The selection of branch cuts is arbitrary, but cuts along contours $\text{Im } k_{z_\alpha} = 0$ or $\text{Re } k_{z_\alpha} = 0$ ($\alpha = 1, 2$) are very useful. If one chooses branch cuts along $\text{Im } k_{z_\alpha} = 0$, then $\text{Im } k_{z_\alpha} > 0$ in the whole top Riemann sheet, and the sign of $\text{Re } k_{z_\alpha}$ changes when k_ρ crosses the cuts. In [24, Sec. 5.3b], it has been thoroughly argued that $\text{Im } k_{z_\alpha} = 0$ and $\text{Re } k_{z_\alpha} = 0$ are along the hyperbola $\text{Re } k_\rho \text{Im } k_\rho = \text{Re } k_\alpha \text{Im } k_\alpha$ for $|\text{Re } k_\rho| < \text{Re } k_\alpha$ and $|\text{Re } k_\rho| > \text{Re } k_\alpha$, respectively. As depicted in Figure 2.6, selecting branch cuts along $\text{Im } k_{z_\alpha} > 0$ guaranties the boundedness of integrals.

Another issue concerning branch point cuts, is the integrand analyticity.

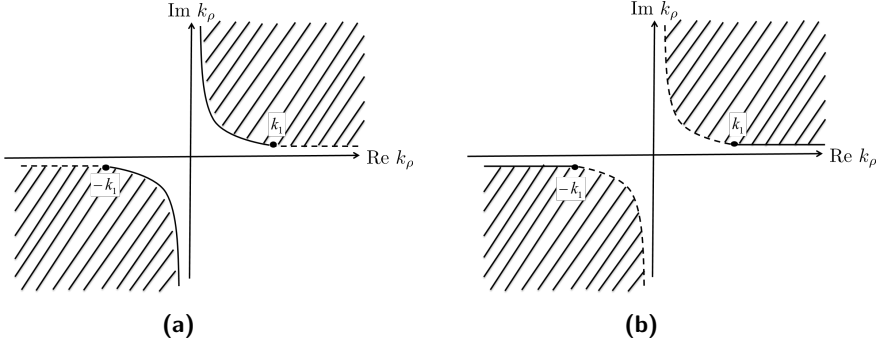


Figure 2.6: Different choices of branch cuts in the complex k_ρ plane. (a) Branch cuts are along $\text{Im } k_{z_1} = 0$. So, $\text{Im } k_{z_1} > 0$ on the entire top Riemann sheet, $\text{Re } k_{z_1} > 0$ on unshaded regions, $\text{Re } k_{z_1} < 0$ on shaded regions. (b) Branch cuts are along $\text{Re } k_{z_1} = 0$. So, $\text{Re } k_{z_1} > 0$ on the entire top Riemann sheet, $\text{Im } k_{z_1} > 0$ on shaded regions, $\text{Im } k_{z_1} < 0$ on unshaded regions.

To keep the integrand analytic over the integration contour, we must deform the contour such that it goes around branch cuts and does not intersect with cuts (see Figure 2.7a).

In w plane, we only have one branch point singularity. To discuss this more clearly, we focus on the first integration in (2.28). A similar procedure can be applied for the radiation integral in Ω_2 . The transformation (2.16) is 2π periodic with respect to $\text{Re } w$. Thus, the entire k_ρ plane can be mapped into various adjacent sections of width 2π in the w plane. For the sake of simplicity, we only consider the interval $-\pi < \text{Re } w < \pi$. For a loss-less material, (2.29) boils down to

$$\text{Im } k_{z_1} = -k_1 \sin(\text{Re } w) \sinh(\text{Im } w). \quad (2.31)$$

It is easy to see that $\text{Im } k_{z_1} > 0$ for $\begin{cases} -\pi < \text{Re } w < 0 & \text{and } \text{Im } w > 0 \\ 0 < \text{Re } w < \pi & \text{and } \text{Im } w < 0 \end{cases}$.

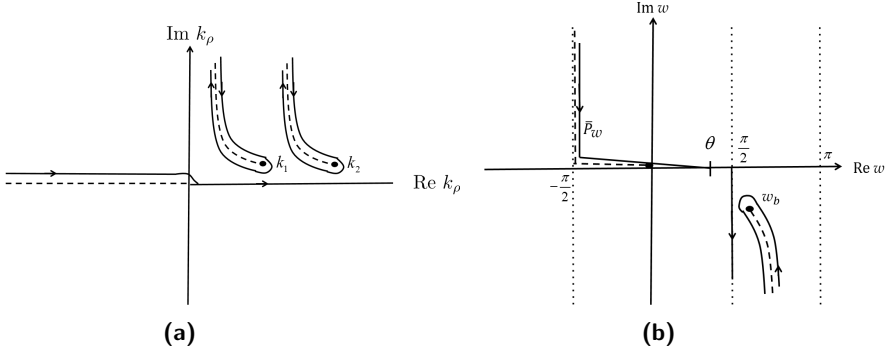


Figure 2.7: Integration path in the complex (a) k_ρ plane (b) w plane goes around branch cuts to avoid singularities and to guaranty that integrands are analytic.

As a matter of fact, (2.16) maps the two-sheeted k_ρ plane (with respect to k_{z_1}) into adjacent regions in the w plane, that is $k_{z_1} = \sqrt{k_1^2 - k_\rho^2} = 0$ is no more double valued and no branch cut arises from it. However, $k_{z_2} = k_1 \sqrt{\eta - \sin^2 w}$ is still a source of a branch cut which originates from the branch point $\sin w_b = \sqrt{\eta}$ ($\eta = \frac{\epsilon_2}{\epsilon_1}$). Similar to \bar{P}_ρ , the integration contour in w plane must avoid branch cuts to ensure that integrands are analytic. Figure 2.7b shows the deformation of \bar{P}_w along the branch cut.

2.3 Asymptotic analysis

Theorem 2. ([16, Sec. 1.4], Huygens' principle) *Let Ω_s be a finite domain which contains all the electromagnetic sources. Furthermore, consider a closed surface Γ which surrounds Ω_s (see Figure 2.8). Then the scattered field distribution on Γ can be extended to the scattered field outside the surface Γ*

$$\mathbf{E}(\mathbf{r}) \cdot \hat{\ell} = \frac{1}{i\omega\mu} \int_{\Gamma} (\nabla^{\mathbf{r}'} \times \mathbf{E}(\mathbf{r}')) \cdot \left(\mathbf{G}^{\mathbf{E}}(\mathbf{r}, \mathbf{r}', \hat{\ell}) \times \hat{n}(\mathbf{r}') \right) - \quad (2.32)$$

$$\left(\nabla^{\mathbf{r}'} \times \mathbf{G}^{\mathbf{E}}(\mathbf{r}, \mathbf{r}', \hat{\ell}) \right) \cdot (\mathbf{E}(\mathbf{r}') \times \hat{n}(\mathbf{r}')) \, ds(\mathbf{r}'),$$

where $\nabla^{\mathbf{r}'}$ denotes the derivatives with respect to \mathbf{r}' , and \hat{n} is the outward-pointing normal vector on Γ . By $\mathbf{G}^{\mathbf{E}}(\mathbf{r}, \mathbf{r}', \hat{\ell})$ we denote the electric field of an electric dipole, oriented in direction $\hat{\ell}$ and located at \mathbf{r}' , observed at point \mathbf{r} .

(2.32) is also known as representation formula [51, Ch. 3, Thm. 3.1.1]. In the case of a scattering problem Ω_s is the scatterer which contains all sources of the scattered field.

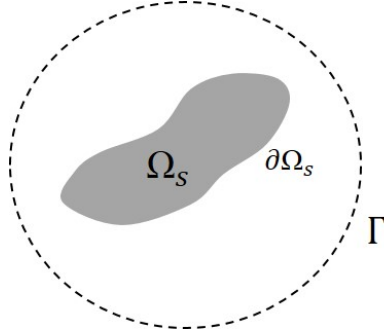


Figure 2.8: The scatterer Ω_s is shown as a shaded region bounded by $\partial\Omega_s$. The integral in (2.32) is calculated over the contour Γ

Equation (2.32) can be simplified when the observation point is located far away from the scatterer, i.e. $kr \rightarrow \infty$. Since (2.32) relies basically on the electric field distribution of an electric dipole $\mathbf{G}^{\mathbf{E}}(\mathbf{r}, \mathbf{r}', \hat{\ell})$, the primary emphasis is on investigating the far-field behavior of a single dipole in free space and in semi-infinite half space. The Green's function for free space is implicitly embedded inside the formulation for the half space. Henceforth, we mainly discuss the half-space problem. Among three forms of the scalar Green's function represented in (2.26), (2.27), and (2.28), we use (2.28), since it has a reduced number of branch cuts.

Remark 4. If the function $f(x)$ is asymptotically equivalent to $g(x)$ in the limit $x \rightarrow x_0$, that is $\lim_{x \rightarrow x_0} \frac{f(x)}{g(x)} = 1$, we write [50, Pgae 4]

$$f(x) \sim g(x) \text{ as } x \rightarrow x_0. \quad (2.33)$$

2 Far field investigation in the presence of substrate

To put (2.28) in a proper form for the asymptotic analysis, we do one more step of simplification and employ the large-argument approximation of the Hankel function for far-field observation points

$$H_n^1(z) = \sqrt{\frac{2}{\pi z}} \left(e^{i(z - \frac{n\pi}{2} - \frac{\pi}{4})} + O\left(\frac{1}{z}\right) \right) \text{ for } |z| \gg n \quad |\arg z| < \pi. \quad (2.34)$$

One can also show that

$$\bar{\rho} = |\rho - \rho'| \sim \rho - \rho' \cos(\phi - \phi') \quad \text{as } \rho \rightarrow \infty, \quad (2.35)$$

where $\rho = |(x, y)|$, $\rho' = |(x', y')|$, $(x, y) = \rho(\cos \phi, \sin \phi)$, and $(x', y') = \rho'(\cos \phi', \sin \phi')$.

Using (2.34) and (2.35), we rewrite (2.28) as

$$g_0(\mathbf{r}, \mathbf{r}') \sim C(\mathbf{r}, \mathbf{r}') \int_{\bar{P}_w} \mathcal{V}(w, \mathbf{r}, \mathbf{r}') e^{r\psi(w, \mathbf{r}, \mathbf{r}')} dw \text{ as } r \rightarrow \infty, \quad (2.36)$$

where $C(\mathbf{r}, \mathbf{r}') = \frac{e^{i\frac{\pi}{4}}}{8\pi} \sqrt{\frac{2k_\alpha}{\pi r \sin \theta}}$ ($\alpha = 1, 2$ specifies different coefficients for different subdomains Ω_α), and

$$\psi(w, \mathbf{r}, \mathbf{r}') = \begin{cases} ik_1 \cos(w - \theta) & \mathbf{r} \in \Omega_1, \\ ik_2 \cos(w - \theta) & \mathbf{r} \in \Omega_2, \end{cases} \quad (2.37)$$

$$\mathcal{V}(w, \mathbf{r}, \mathbf{r}') = \begin{cases} \sqrt{\sin w} e^{-ik_1 r' \sin w \sin \theta' \cos(\phi - \phi')} \\ \quad \left[e^{(-ik_1 \cos w z')} + f(w) e^{(ik_1 \cos w z')} \right] & \mathbf{r} \in \Omega_1, \\ \sqrt{\sin w} e^{-ik_2 r' \sin w \sin \theta' \cos(\phi - \phi')} \\ \quad e^{(ik_{z_1}(w) z')} (1 + f(w)) & \mathbf{r} \in \Omega_2. \end{cases} \quad (2.38)$$

Note that (r, θ, ϕ) and (r', θ', ϕ') are the spherical coordinates of \mathbf{r} and \mathbf{r}' , respectively, where $r = |\mathbf{r}|$, θ is the longitudinal angle with respect to the z axis, and ϕ is the azimuthal angle in the x - y plane. One must note that, the double valued square root $\sqrt{\sin w}$ has the same branch cut as the Hankel function.

Now that (2.36) has the suitable form for asymptotic evaluations, we discuss the following additive contributions to the asymptotic analysis of radiation integrals in the complex plane:

- Saddle point contribution

The stationary phase method is used to derive it [50, Ch. 4].

- Critical point contributions

There are three types of critical points:

- branch point singularity
- pole singularity
- integration end points.

The far-field asymptotics of each contribution can be determined using the method of steepest descent [50, Ch. 3] and [7, Ch. 7].

2.3.1 Saddle point contribution

To keep the procedure clear, we only discuss (2.36) in Ω_1 . Similar calculations can be used for the integration in Ω_2 .

The integral in Ω_1 has only one first order saddle point at $w_s = \theta$

$$\psi'(w_s) = 0 \text{ and } \psi''(w_s) \neq 0. \quad (2.39)$$

where ψ' and ψ'' mean the first and the second derivatives of ψ with respect to w , respectively. The steepest-descent path (\bar{P}_s) through the saddle point lies on $\text{Im } \psi(w) = \text{const}$, that is $\text{Im } \psi(w) = \text{Im } \psi(w_s)$. If the medium is loss-less, then the Steepest Descent Path (SDP) is:

$$\text{Im } \psi(w) = k_1 \cos(\text{Re } w - \theta) \cosh(\text{Im } w) = k_1. \quad (2.40)$$

Directions of the SDP at the saddle point are $-\frac{\pi}{4}$ and $\frac{3\pi}{4}$ [7, Sec. 7.2, table 7.1]. For this problem, integration contours must be along a direction which

2 Far field investigation in the presence of substrate

conserves the boundedness of integrands when $r \rightarrow \infty$. The phase term in (2.36) is

$$r \psi(w) = rk_1 [\sin(\operatorname{Re} w - \theta) \sinh(\operatorname{Im} w) + i \cos(\operatorname{Re} w - \theta) \cosh(\operatorname{Im} w)]. \quad (2.41)$$

In order to have bounded integrands for observation points located away from the scatterer we must have

$$\sin(\operatorname{Re} w - \theta) \sinh(\operatorname{Im} w) < 0, \quad (2.42)$$

which means

$$\begin{cases} 0 < \operatorname{Re} w - \theta < \frac{\pi}{2} & \rightarrow \operatorname{Im} w < 0, \\ -\frac{\pi}{2} < \operatorname{Re} w - \theta < 0 & \rightarrow \operatorname{Im} w > 0. \end{cases} \quad (2.43)$$

Consequently, we choose \bar{P}_s along $-\frac{\pi}{4}$ and keep \bar{P}_w and \bar{P}_s in those regions of the w plane that (2.42) is fulfilled (see Figure 2.9).

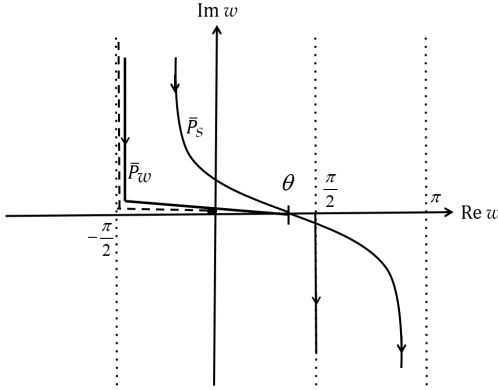


Figure 2.9: Integration contours in the complex w plane. \bar{P}_s is the steepest descent path (SDP).

Theorem 3. ([50, Ch. 3, Page 50]) *if $\mathcal{V}(w, \mathbf{r}, \mathbf{r}')$ does not have any singularity at $w = w_s$, then the asymptotic form of the radiation integral (2.36)*

along the SDP is

$$\begin{aligned}
 g_s(\mathbf{r}, \mathbf{r}') &= C(\mathbf{r}, \mathbf{r}') \int_{\bar{P}_s} \mathcal{V}(w, \mathbf{r}, \mathbf{r}') e^{r\psi(w, \mathbf{r}, \mathbf{r}')} dw \\
 &\sim C(\mathbf{r}, \mathbf{r}') \sqrt{\frac{-2\pi}{r\psi''(w_s)}} \mathcal{V}(w_s, \mathbf{r}, \mathbf{r}') e^{r\psi(w_s, \mathbf{r}, \mathbf{r}')} \quad \text{for } r \rightarrow \infty
 \end{aligned} \tag{2.44}$$

$$= \begin{cases} \frac{e^{ik_1 r}}{4\pi r} e^{-ik_1(\sin\theta \cos\phi x' + \sin\theta \sin\phi y')} \\ \quad \left[e^{-ik_1 \cos\theta z'} + f(\theta) e^{ik_1 \cos\theta z'} \right] & \mathbf{r} \in \Omega_1, \\ \\ \frac{e^{ik_2 r}}{4\pi r} e^{-ik_2(\sin\theta \cos\phi x' + \sin\theta \sin\phi y')} \\ \quad e^{-ik_2 \sqrt{\frac{\epsilon_1}{\epsilon_2} - \sin^2\theta} z'} (1 + f(\theta)) & \mathbf{r} \in \Omega_2. \end{cases}$$

The result obtained above is valid as far as no singularity exists in the vicinity of the saddle point. In Section 2.3.3, it will be shown that a pole singularity shows up near the saddle point under some special conditions. In this case, the final result for integrating along the SDP changes. More details are given in Section 2.3.3.

2.3.2 Branch point contribution

As explained in Section 2.2.3, the integrand in (2.36) has only one branch cut. In Ω_1 , $k_{z_2} = k_1 \sqrt{\eta - \sin^2 w}$ is the cause of a branch cut at $\sin(w_b) = \sqrt{\eta}$. For a special observation angle θ_b , the branch point w_b lies on \bar{P}_s . Using (2.40), we derive θ_b as

$$\theta_b = \text{Re } w_b - \cos^{-1} \left(\frac{1}{\cosh(\text{Im } w_b)} \right). \tag{2.45}$$

If $\theta > \theta_b$ the branch point intersects with the SDP. For an intersected w_b , we surround the branch cut with an appropriate contour \bar{P}_b in order to keep the integrand analytic (see Figure 2.10).

Theorem 4. *The asymptotic form of the radiation integral (2.36) along the contour \bar{P}_b is [38]:*

$$\begin{aligned} g_b(\mathbf{r}, \mathbf{r}') &= C(\mathbf{r}, \mathbf{r}') \int_{\bar{P}_b} \mathcal{V}(w, \mathbf{r}, \mathbf{r}') e^{r\psi(w, \mathbf{r}, \mathbf{r}')} dw \\ &\sim C(\mathbf{r}, \mathbf{r}') \frac{\mathcal{V}_0 \sqrt{\pi}}{(r|\psi'(w_b)|)^{\frac{3}{2}}} e^{r\psi(w_b)} \quad \text{for } r \rightarrow \infty, \end{aligned} \quad (2.46)$$

where $\mathcal{V} \sim \mathcal{V}_0 \sqrt{(w - w_b)}$, $w \rightarrow w_b$.

Using Theorem 4, one can derive $g_b(\mathbf{r}, \mathbf{r}')$ for TM modes as follows

$$g_b(\mathbf{r}, \mathbf{r}') = \begin{cases} \frac{e^{-i\frac{\pi}{4}}}{4\pi} \sqrt{\frac{k_1}{r \eta \sin \theta}} e^{-ik_2(\cos \phi x' + \sin \phi y')} & \mathbf{r} \in \Omega_1, \\ \frac{\exp(ik_1(\sqrt{1-\eta}(z+z') + \sqrt{\eta}\rho)) U(\theta - \theta_b)}{[k_1(\sqrt{1-\eta} r \sin \theta - \sqrt{\eta} r \cos \theta)]^{\frac{3}{2}} (1-\eta)^{\frac{1}{4}}} & \\ \frac{e^{i\frac{3\pi}{4}}}{4\pi} \sqrt{\frac{k_2}{r \eta \sin \theta}} e^{-ik_1(\cos \phi x' + \sin \phi y')} & \mathbf{r} \in \Omega_2. \\ \frac{\exp(ik_2(\sqrt{1-\eta^{-1}}z + \sqrt{\eta^{-1}}\rho)) U(\theta - \theta_b)}{[k_2(\sqrt{1-\eta^{-1}} r \sin \theta + \sqrt{\eta^{-1}} r \cos \theta)]^{\frac{3}{2}} (1-\eta^{-1})^{\frac{1}{4}}} & \end{cases} \quad (2.47)$$

where $U(x) = \begin{cases} 1 & x > 0 \\ 0 & x < 0 \end{cases}$, and $\eta = \frac{\epsilon_2}{\epsilon_1}$.

2.3.3 Pole contribution

In (2.36), $f(w)$ possesses one pole singularity which must be taken into account in the case that it intersects the SDP. For the TM mode, we have

$$f(w) = \frac{\eta \cos w - \sqrt{\eta - \sin^2 w}}{\eta \cos w + \sqrt{\eta - \sin^2 w}}. \quad (2.48)$$

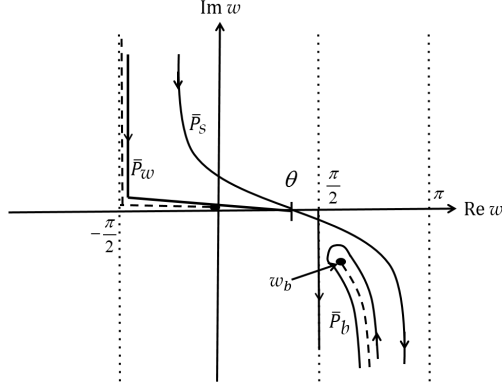


Figure 2.10: Integration contours in the complex w plane. w_b is the branch point and \bar{P}_b surrounds the branch cut.

Thus, the pole singularity for the radiation integral in Ω_1 lies on $\sqrt{\eta - \sin^2 w_p} = -\eta \cos w_p$. It can be shown that [24, Ch. 5]

$$\cos w_p = -\frac{1}{\sqrt{1 + \eta}} \quad (2.49)$$

and

$$\sin w_p = \sqrt{\frac{\eta}{1 + \eta}}. \quad (2.50)$$

Remark 5. w_p lies on the SDP for the special observation point θ_p which can be derived using the same procedure as for θ_b in Section 2.2.3

$$\theta_p = \text{Re } w_p - \cos^{-1} \left(\frac{1}{\cosh(\text{Im } w_p)} \right). \quad (2.51)$$

Theorem 5. As a result of residue theorem, the pole contribution in the radiation integral (2.36) under the condition $w_p \neq \theta_p$ is

$$g_p(\mathbf{r}, \mathbf{r}') = i2\pi C(\mathbf{r}, \mathbf{r}') \text{Res}_{w=w_p} (\mathcal{V}(w, \mathbf{r}, \mathbf{r}') e^{r\psi(w, \mathbf{r}, \mathbf{r}')} U(\theta - \theta_p)) \quad (2.52)$$

Remark 6. It can be shown that w_p crosses the contour only under the condition that the loss of substrate material is much bigger than that in Ω_1

2 Far field investigation in the presence of substrate

($|\eta| \gg 1$ and $\arg \eta \rightarrow \pi/2$), and also the observation point is located on the substrate $\theta = \pi/2$ [24, Ch. 5]. Under this condition and using (2.49), the pole is located at

$$w_p = \frac{\pi}{2} + \frac{1}{\sqrt{\eta}}. \quad (2.53)$$

The pole derived in (2.53) lies near the saddle point ($w_s = \theta = \frac{\pi}{2}$). Therefore, (2.44) is no more the correct form of integrating along the SDP. One must consider the effect of the singularity in the vicinity of the saddle point. For this end, we introduce a more generalized form of integration along the SDP, $g_s^*(\mathbf{r}, \mathbf{r}')$ which is different from $g_s(\mathbf{r}, \mathbf{r}')$ when $w_p = w_s$

$$g_s^*(\mathbf{r}, \mathbf{r}') = \begin{cases} g_s(\mathbf{r}, \mathbf{r}') & w_p \neq w_s, \\ g_{sp}(\mathbf{r}, \mathbf{r}') & w_p = w_s. \end{cases} \quad (2.54)$$

Theorem 6. ([24, Sec. 4.4]) *The asymptotic form of the radiation integral (2.36) along the SDP, when a pole singularity exists in the vicinity of the saddle point ($w_p = \theta$), is*

$$g_{sp}(\mathbf{r}, \mathbf{r}') \sim C(\mathbf{r}, \mathbf{r}') e^{r\psi(w_p, \mathbf{r}, \mathbf{r}')} \left[i2a\sqrt{\pi} e^{-rb^2} Q(ib\sqrt{r}) + \sqrt{\frac{\pi}{r}} T(0) \right] \text{ for } r \rightarrow \infty, \quad (2.55)$$

and

$$a = \lim_{w \rightarrow w_p} [(w - w_p)\mathcal{V}(w, \mathbf{r}, \mathbf{r}')], \quad b = \sqrt{\psi(w_s, \mathbf{r}, \mathbf{r}') - \psi(w_p, \mathbf{r}, \mathbf{r}')},$$

$$h = \sqrt{\frac{-2}{\psi''(w_s, \mathbf{r}, \mathbf{r}')}}, \quad T(0) = h\mathcal{V}(w_s, \mathbf{r}, \mathbf{r}') + \frac{a}{b},$$

$$Q(y) = \int_y^\infty e^{-x^2} dx.$$

Under the assumptions $\theta = \pi/2$, $|\eta| \gg 1$ and $\arg \eta = \pi/2$ (2.55) becomes

$$g_{sp}(\mathbf{r}, \mathbf{r}') \sim \begin{cases} \frac{e^{ik_1 r}}{2\pi r} e^{-ik_1(\cos \phi x' + \sin \phi y')} & \mathbf{r} \in \Omega_1, \\ \left(1 + i\sqrt{\pi} \frac{k_1 r}{2|\eta|} e^{-\frac{k_1 r}{2|\eta|}} - i2\sqrt{\frac{k_1 r}{2|\eta|}} \int_0^{-i\sqrt{\frac{k_1 r}{2|\eta|}}} e^{-x^2} dx \right) & \\ \frac{e^{ik_2 r}}{2\pi r} e^{-ik_1(\cos \phi x' + \sin \phi y')} & \mathbf{r} \in \Omega_2. \\ \left(1 + i\sqrt{\pi} \frac{k_2 r}{2|\eta|} e^{-\frac{k_2 r}{2|\eta|}} - i2\sqrt{\frac{k_2 r}{2|\eta|}} \int_0^{-i\sqrt{\frac{k_2 r}{2|\eta|}}} e^{-x^2} dx \right) & \end{cases} \quad (2.56)$$

2.3.4 Integration end point contribution

Equation (2.37) in Ω_1 shows that

$$\text{Im } \psi(w, \mathbf{r}, \mathbf{r}') = \cos(\text{Re } w) \sinh(\text{Im } w) \sin(\theta) - \sin(\text{Re } w) \sinh(\text{Im } w) \cos(\theta). \quad (2.57)$$

Using (2.57) and Figure 2.10, one can easily see that the end points of contours \bar{P} , \bar{P}_s , and \bar{P}_b at $|w| \rightarrow \infty$ are situated in regions wherein $e^{ik_1 \psi(w, \mathbf{r}, \mathbf{r}')} \rightarrow 0$. In other words no contributions arise from end points. The same argument applies to the integration in Ω_2 .

2.3.5 Discussion

The final form of the scalar Green's function far away from the dipole source in the presence of a substrate is obtained by putting together all the contributions discussed earlier

$$g_0(\mathbf{r}, \mathbf{r}') = g_s^*(\mathbf{r}, \mathbf{r}') + g_b(\mathbf{r}, \mathbf{r}'). \quad (2.58)$$

Each term on the right hand side of (2.58) decays with a different rate with respect to the distance of the observation point \mathbf{r} from \mathbf{r}' . Using (2.44) and (2.47), one can see that $g_s(\mathbf{r}, \mathbf{r}')$ and $g_b(\mathbf{r}, \mathbf{r}')$ decay according to $\frac{1}{r}$ and $\frac{1}{r^2}$,

respectively. In the case of having the pole contribution, there is a term decreasing as $\frac{1}{\sqrt{r}}$ (see Equation (2.56)).

- **Saddle point contribution**

Taking a closer look at (2.44) reveals that $g_s(\mathbf{r}, \mathbf{r}')$ comprises direct wave and reflected wave contributions in Ω_1 and the transmitted wave in Ω_2 . The first term on the right hand side of (2.44) in Ω_1 is the spherical wave propagating directly from the source point to the observation point. This term is identical with the field of a dipole located in free space observed at far distances. The second term on the right hand side of (2.44) in Ω_1 can be interpreted as the reflected wave from the interface which is multiplied by the reflection coefficient. Finally, the saddle point contribution in Ω_2 resembles a transmitted wave through the interface. The amplitude of the transmitted wave contains the factor $1 + f(\theta)$ which is identical to the transmission coefficient. $g_s(\mathbf{r}, \mathbf{r}')$ can also be obtained directly through ray optics, which means that the direct and the reflected waves are observed at points located in the same half space as the source, whereas the transmitted wave is received inside the other half space.

- **Branch point contribution**

The result shown in (2.47) reveals that $g_b(\mathbf{r}, \mathbf{r}')$ does not have that much effect on the final Green's function due to the faster decay of $\frac{1}{r^2}$ in comparison with $g_s(\mathbf{r}, \mathbf{r}')$. If the material is lossy, $g_b(\mathbf{r}, \mathbf{r}')$ even decays exponentially. However, there are some exceptions, worth being taken into account:

- medium 1 loss-less, medium 2 lossy and $\theta \rightarrow \frac{\pi}{2}$
 $g_s(\mathbf{r}, \mathbf{r}')$ has no exponential decay in Ω_1 whereas $g_b(\mathbf{r}, \mathbf{r}')$ decreases in both lateral and longitudinal directions in Ω_1 . As a result, $g_s(\mathbf{r}, \mathbf{r}')$ dominates $g_b(\mathbf{r}, \mathbf{r}')$.
 In Ω_2 , $g_s(\mathbf{r}, \mathbf{r}')$ has exponential decay in radial direction, however, $g_b(\mathbf{r}, \mathbf{r}')$ decreases only in z direction. This means that $g_b(\mathbf{r}, \mathbf{r}')$ dominates $g_s(\mathbf{r}, \mathbf{r}')$ in Ω_2 when $\rho \gg z$ or in other words $\theta \rightarrow \frac{\pi}{2}$.

- medium 1 lossy, medium 2 loss-less and $\theta \rightarrow \frac{\pi}{2}$
 $g_s(\mathbf{r}, \mathbf{r}')$ has exponential decay in Ω_1 , while $g_b(\mathbf{r}, \mathbf{r}')$ decays only in longitudinal direction. As a result, $g_b(\mathbf{r}, \mathbf{r}')$ dominates $g_s(\mathbf{r}, \mathbf{r}')$ in Ω_1 when $\rho \gg z$ or in other words $\theta \rightarrow \frac{\pi}{2}$. In Ω_2 , it is only $g_b(\mathbf{r}, \mathbf{r}')$ which features from exponential decay.
- $\theta \rightarrow \frac{\pi}{2}$ and $z' \rightarrow 0$

In this case, the ray-optical part vanishes and lower order terms, $O(\frac{1}{r^2})$, in the asymptotic expansion of $g_s(\mathbf{r}, \mathbf{r}')$ become important. Under this condition, the $g_b(\mathbf{r}, \mathbf{r}')$ contribution is comparable to the contribution of $g_s(\mathbf{r}, \mathbf{r}')$.

- **Pole contribution**

The Equation (2.56) has different terms with different decay rates on the right hand side. As explained in Section 2.3.3, the effect of pole singularity only matters when the medium 2 is highly lossy and the medium 1 is loss-less. So, the first term on the right hand side of (2.56) is the same as (2.44) when the substrate is highly lossy. The second term on the right hand side of (2.56) resembles surface-waves because it decays as $\frac{1}{\sqrt{r}}$. However, this term does not play any significant role in the field observed at far distances because of the fast exponential decay.

2.4 Far-field closed form

In this section, we use the results obtained in the previous section and derive a closed form formulation for far-field value for scattering problems.

As explained in Section 2.3, the dominant contribution to $g_0(\mathbf{r}, \mathbf{r}')$ at far distances when $\theta \neq 0$, $\theta \neq \frac{\pi}{2}$ arises from the saddle point contribution (2.44), which means that the Green's function decays according to $\frac{1}{r}$ as $r \rightarrow \infty$.

Based on (2.32), we need $\mathbf{G}^{\mathbf{E}}(\mathbf{r}, \mathbf{r}', \hat{\ell})$ to derive the scattered field at far distances in the direction $\hat{\ell}$. Using (2.44), one can easily show that for $\hat{\ell} = \hat{r}$ the value of $\mathbf{G}^{\mathbf{E}}$ at $r \rightarrow \infty$ decays with the order $\frac{1}{r^2}$, i.e. the radial component of the far-field pattern decays faster than other terms. Consequently, electromagnetic fields at far distances have only components in polar and

2 Far field investigation in the presence of substrate

azimuthal directions ($\hat{\theta}$ and $\hat{\phi}$), that is the energy flux in the far-field area propagates only along the radial direction.

Proposition 4. *The electric field observed at far distances when $\theta \neq 0$ and $\theta \neq \frac{\pi}{2}$, has the following asymptotic form in direction $\hat{\ell}$*

$$\mathbf{E}(\mathbf{r}) \cdot \hat{\ell} = \frac{\exp(ik_\alpha r)}{r} \left(\mathbf{E}_\infty(\hat{\mathbf{r}}) \cdot \hat{\ell} + O\left(\frac{1}{r}\right) \right) \quad \text{as } r \rightarrow \infty, \quad (2.59)$$

where $\alpha = 1, 2$, $\hat{\mathbf{r}} = \mathbf{r}/r$, and

$$\begin{aligned} \mathbf{E}_\infty(\hat{\mathbf{r}}) \cdot \hat{\ell} &= \int_\Gamma (\nabla^{\mathbf{r}'} \times \mathbf{E}(\mathbf{r}')) \cdot \left(\mathbf{G}_\infty(\hat{\mathbf{r}}, \mathbf{r}', \hat{\ell}) \times \hat{\mathbf{n}}(\mathbf{r}') \right) ds(\mathbf{r}') \\ &\quad - \int_\Gamma (\nabla^{\mathbf{r}'} \times \mathbf{G}_\infty(\hat{\mathbf{r}}, \mathbf{r}', \hat{\ell})) \cdot (\mathbf{E}(\mathbf{r}') \times \hat{\mathbf{n}}(\mathbf{r}')) ds(\mathbf{r}'), \end{aligned} \quad (2.60)$$

$$\mathbf{G}_\infty(\hat{\mathbf{r}}, \mathbf{r}', \hat{\ell}) = \begin{cases} \frac{\hat{\ell}}{4\pi} e^{-ik_1(\sin\theta \cos\phi x' + \sin\theta \sin\phi y')} \\ \quad \left[e^{-ik_1 \cos\theta z'} + f(\theta) e^{ik_1 \cos\theta z'} \right] & \mathbf{r} \in \Omega_1, \\ \frac{\hat{\ell}}{4\pi} e^{-ik_2(\sin\theta \cos\phi x' + \sin\theta \sin\phi y')} \\ \quad e^{-ik_2 \sqrt{\frac{\epsilon_1}{\epsilon_2} - \sin^2\theta} z'} (1 - f(\theta)) & \mathbf{r} \in \Omega_2. \end{cases} \quad (2.61)$$

We must note that $\mathbf{E}_\infty(\hat{\mathbf{r}})$, which is independent of the observation distance r , is known as the far-field pattern.

As mentioned already, the electric field at far distances, has no component in the radial direction, i.e. $\mathbf{E}_\infty(\hat{\mathbf{r}})$ has only components in $\hat{\theta}$ and $\hat{\phi}$ directions. For $\hat{\ell} = \hat{\theta}$, (2.9) shows that $\mathbf{G}^{\mathbf{H}}(\mathbf{r}, \mathbf{r}', \hat{\ell}) \cdot \hat{z} = 0$, which means that only the TM wave expansion must be used. Similarly, for $\hat{\ell} = \hat{\phi}$, $\mathbf{G}^{\mathbf{E}}(\mathbf{r}, \mathbf{r}', \hat{\ell}) \cdot \hat{z} = 0$, then the TE wave expansion must be applied.

Proposition 5. (2.60) is valid for any Lipschitz surface Γ around the scatterer.

Proof. Consider a subregion Ω_f between two closed paths Γ_i and Γ_o around the scatterer (see Figure 2.11). Using Green's formula we have

$$\begin{aligned} & \int_{\Omega_f} (\nabla^{\mathbf{r}'} \times \nabla^{\mathbf{r}'} \times \mathbf{E}(\mathbf{r}')) \cdot \mathbf{G}_\infty(\hat{\mathbf{r}}, \mathbf{r}', \hat{\ell}) \, d\mathbf{r}' = \\ & \int_{\Omega_f} (\nabla^{\mathbf{r}'} \times \mathbf{E}(\mathbf{r}')) \cdot (\nabla^{\mathbf{r}'} \times \mathbf{G}_\infty(\hat{\mathbf{r}}, \mathbf{r}', \hat{\ell})) \, d\mathbf{r}' \\ & - \int_{\partial\Omega_f} (\nabla^{\mathbf{r}'} \times \mathbf{E}(\mathbf{r}')) \cdot (\mathbf{G}_\infty(\hat{\mathbf{r}}, \mathbf{r}', \hat{\ell}) \times \hat{\mathbf{n}}(\mathbf{r}')) \, ds(\mathbf{r}'), \end{aligned} \quad (2.62)$$

and

$$\begin{aligned} & \int_{\Omega_f} (\nabla^{\mathbf{r}'} \times \nabla^{\mathbf{r}'} \times \mathbf{G}_\infty(\hat{\mathbf{r}}, \mathbf{r}', \hat{\ell})) \cdot \mathbf{E}(\mathbf{r}') \, d\mathbf{r}' = \\ & \int_{\Omega_f} (\nabla^{\mathbf{r}'} \times \mathbf{E}(\mathbf{r}')) \cdot (\nabla^{\mathbf{r}'} \times \mathbf{G}_\infty(\hat{\mathbf{r}}, \mathbf{r}', \hat{\ell})) \, d\mathbf{r}' \\ & - \int_{\partial\Omega_f} (\nabla^{\mathbf{r}'} \times \mathbf{G}_\infty(\hat{\mathbf{r}}, \mathbf{r}', \hat{\ell})) \cdot (\mathbf{E}(\mathbf{r}') \times \hat{\mathbf{n}}(\mathbf{r}')) \, ds(\mathbf{r}'). \end{aligned} \quad (2.63)$$

We also know that

$$\begin{aligned} \nabla^{\mathbf{r}'} \times \nabla^{\mathbf{r}'} \times \mathbf{E}(\mathbf{r}') - k_\alpha^2 \mathbf{E}(\mathbf{r}') &= 0, \\ \nabla^{\mathbf{r}'} \times \nabla^{\mathbf{r}'} \times \mathbf{G}_\infty(\hat{\mathbf{r}}, \mathbf{r}', \hat{\ell}) - k_\alpha^2 \mathbf{G}_\infty(\hat{\mathbf{r}}, \mathbf{r}', \hat{\ell}) &= 0. \end{aligned} \quad (2.64)$$

Subtracting (2.63) from (2.62) and using (2.64), we have

$$\begin{aligned} & \int_{\partial\Omega_f} (\nabla^{\mathbf{r}'} \times \mathbf{E}(\mathbf{r}')) \cdot (\mathbf{G}_\infty(\hat{\mathbf{r}}, \mathbf{r}', \hat{\ell}) \times \hat{\mathbf{n}}(\mathbf{r}')) \, ds(\mathbf{r}') \\ & - \int_{\partial\Omega_f} (\nabla^{\mathbf{r}'} \times \mathbf{G}_\infty(\hat{\mathbf{r}}, \mathbf{r}', \hat{\ell})) \cdot (\mathbf{E}(\mathbf{r}') \times \hat{\mathbf{n}}(\mathbf{r}')) \, ds(\mathbf{r}') = 0. \end{aligned} \quad (2.65)$$

Since $\partial\Omega_f = \Gamma_o \cup \Gamma_i$, we can rewrite the identity above as follows

$$\begin{aligned}
 & \int_{\Gamma_o} (\nabla^{\mathbf{r}'} \times \mathbf{E}(\mathbf{r}')) \cdot (\mathbf{G}_\infty(\hat{\mathbf{r}}, \mathbf{r}', \hat{\ell}) \times \hat{\mathbf{n}}(\mathbf{r}')) \, ds(\mathbf{r}') \\
 & - \int_{\Gamma_o} (\nabla^{\mathbf{r}'} \times \mathbf{G}_\infty(\hat{\mathbf{r}}, \mathbf{r}', \hat{\ell})) \cdot (\mathbf{E}(\mathbf{r}') \times \hat{\mathbf{n}}(\mathbf{r}')) \, ds(\mathbf{r}') \\
 & = \int_{\Gamma_i} (\nabla^{\mathbf{r}'} \times \mathbf{E}(\mathbf{r}')) \cdot (\mathbf{G}_\infty(\hat{\mathbf{r}}, \mathbf{r}', \hat{\ell}) \times \hat{\mathbf{n}}(\mathbf{r}')) \, ds(\mathbf{r}') \\
 & - \int_{\Gamma_i} (\nabla^{\mathbf{r}'} \times \mathbf{G}_\infty(\hat{\mathbf{r}}, \mathbf{r}', \hat{\ell})) \cdot (\mathbf{E}(\mathbf{r}') \times \hat{\mathbf{n}}(\mathbf{r}')) \, ds(\mathbf{r}').
 \end{aligned} \tag{2.66}$$

□

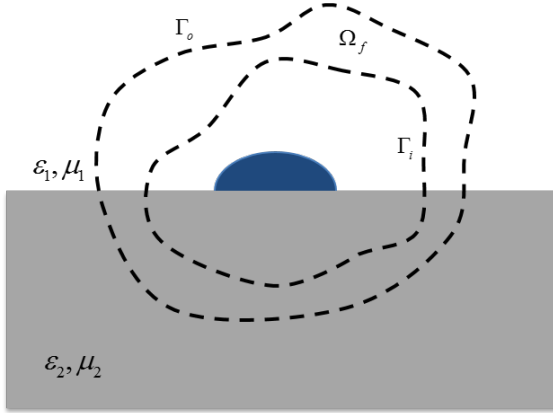


Figure 2.11: Volume-based far-field integration region.

Proposition 6. *The far-field pattern representation using a volume integral is [48, Section 13.6]*

$$\begin{aligned}
 \mathbf{E}_\infty(\hat{\mathbf{r}}) \cdot \hat{\ell} &= \int_{\Omega_f} \nabla^{\mathbf{r}'} \times \mathbf{E}(\mathbf{r}') \cdot \nabla^{\mathbf{r}'} \times (\Psi(\mathbf{r}') \mathbf{G}_\infty(\hat{\mathbf{r}}, \mathbf{r}', \hat{\ell})) \, d\mathbf{r}' \\
 & - \int_{\Omega_f} \nabla^{\mathbf{r}'} \times (\Psi(\mathbf{r}') \mathbf{E}(\mathbf{r}')) \cdot \nabla^{\mathbf{r}'} \times \mathbf{G}_\infty(\hat{\mathbf{r}}, \mathbf{r}', \hat{\ell}) \, d\mathbf{r}',
 \end{aligned} \tag{2.67}$$

where Ω_f is a subregion between two closed paths Γ_i and Γ_o around the scatterer (see Figure 2.11), and $\Psi \in H^1(\Omega_f)$ is a cutoff function such that

$$\Psi|_{\Gamma_i} \equiv 1, \text{ and } \Psi|_{\Gamma_o} \equiv 0. \quad (2.68)$$

Proof. Considering $\Gamma = \Gamma_i$, one can write (2.60) in the following way

$$\begin{aligned} \mathbf{E}_\infty(\hat{\mathbf{r}}) \cdot \hat{\boldsymbol{\ell}} &= \int_{\Gamma_i} (\hat{\mathbf{n}}(\mathbf{r}') \times \nabla^{\mathbf{r}'} \times \mathbf{E}(\mathbf{r}')) \cdot (\Psi(\mathbf{r}') \mathbf{G}_\infty(\hat{\mathbf{r}}, \mathbf{r}', \hat{\boldsymbol{\ell}})) ds(\mathbf{r}') \\ &\quad - \int_{\Gamma_i} (\hat{\mathbf{n}}(\mathbf{r}') \times \nabla^{\mathbf{r}'} \times \mathbf{G}_\infty(\hat{\mathbf{r}}, \mathbf{r}', \hat{\boldsymbol{\ell}})) \cdot (\Psi(\mathbf{r}') \mathbf{E}(\mathbf{r}')) ds(\mathbf{r}'). \end{aligned} \quad (2.69)$$

The first term on the right hand side of (2.69) can be rewritten as

$$\begin{aligned} &\int_{\Gamma_i} (\hat{\mathbf{n}}(\mathbf{r}') \times \nabla^{\mathbf{r}'} \times \mathbf{E}(\mathbf{r}')) \cdot (\Psi(\mathbf{r}') \mathbf{G}_\infty(\hat{\mathbf{r}}, \mathbf{r}', \hat{\boldsymbol{\ell}})) ds(\mathbf{r}') = \\ &\quad \int_{\Omega_f} (\nabla^{\mathbf{r}'} \times \nabla^{\mathbf{r}'} \times \mathbf{E}(\mathbf{r}')) \cdot (\Psi(\mathbf{r}') \mathbf{G}_\infty(\hat{\mathbf{r}}, \mathbf{r}', \hat{\boldsymbol{\ell}})) d\mathbf{r}' \\ &\quad - \int_{\Omega_f} (\nabla^{\mathbf{r}'} \times \mathbf{E}(\mathbf{r}')) \cdot (\nabla^{\mathbf{r}'} \times (\Psi(\mathbf{r}') \mathbf{G}_\infty(\hat{\mathbf{r}}, \mathbf{r}', \hat{\boldsymbol{\ell}}))) d\mathbf{r}'. \end{aligned} \quad (2.70)$$

In the same way the second term is

$$\begin{aligned} &\int_{\Gamma_i} (\hat{\mathbf{n}}(\mathbf{r}') \times \nabla^{\mathbf{r}'} \times \mathbf{G}_\infty(\hat{\mathbf{r}}, \mathbf{r}', \hat{\boldsymbol{\ell}})) \cdot (\Psi(\mathbf{r}') \mathbf{E}(\mathbf{r}')) ds(\mathbf{r}') = \\ &\quad \int_{\Omega_f} (\nabla^{\mathbf{r}'} \times \nabla^{\mathbf{r}'} \times \mathbf{G}_\infty(\hat{\mathbf{r}}, \mathbf{r}', \hat{\boldsymbol{\ell}})) \cdot (\Psi(\mathbf{r}') \mathbf{E}(\mathbf{r}')) d\mathbf{r}' \\ &\quad - \int_{\Omega_f} (\nabla^{\mathbf{r}'} \times \mathbf{G}_\infty(\hat{\mathbf{r}}, \mathbf{r}', \hat{\boldsymbol{\ell}})) \cdot (\nabla^{\mathbf{r}'} \times (\Psi(\mathbf{r}') \mathbf{E}(\mathbf{r}'))) d\mathbf{r}'. \end{aligned} \quad (2.71)$$

Subtracting (2.71) from (2.70) and keeping in mind that $\nabla \times \nabla \times \mathbf{E} - k^2 \mathbf{E} = 0$ and $\nabla^{\mathbf{r}'} \times \nabla^{\mathbf{r}'} \times \mathbf{G}_\infty(\hat{\mathbf{r}}, \mathbf{r}', \hat{\boldsymbol{\ell}}) - k^2 \mathbf{G}_\infty(\hat{\mathbf{r}}, \mathbf{r}', \hat{\boldsymbol{\ell}}) = 0$ we retrieve (2.67). \square

Formula (2.67) is based on volume integral which is continuous on the energy space $H(\text{curl})$ [48, Page 387]. Since continuous functions enjoy the super convergence, we use (2.67) for our numerical experiments.

2.5 NGSolve implementation

Our experiments are based on the finite element library **NGSolve** developed by Joachim Schoeberl at the Vienna University of Technology. We use NETGEN, which is a mesh generating library embedded in NGSolve, to make our meshes. The unbounded computational region is truncated using a box Perfectly Matched Layer (PML)[48, 69]. Figure 2.12 shows a typical geometry setting that we use in our simulations. We divide the solution domain Ω to two subdomains. The PML domain Ω_{PML} , which contains the outer layer to truncate the solution domain, and the physical domain $\Omega_p = \Omega \setminus \Omega_{PML}$. We use the PML layer with the thickness of $70nm$, and the absorption coefficient $\alpha = 1$ [17]. The far-field integration region Ω_f is considered to be the domain between two spheres around the scatterer, such that r_o and r_i are radii of the outer and the inner spheres, respectively (see Figure 2.12). We also consider the cutoff function as following

$$\Psi = \begin{cases} \frac{r^2 - r_o^2}{r_i^2 - r_o^2} & \mathbf{r} \in \Omega_f, \\ 0 & \mathbf{r} \notin \Omega_f. \end{cases} \quad (2.72)$$

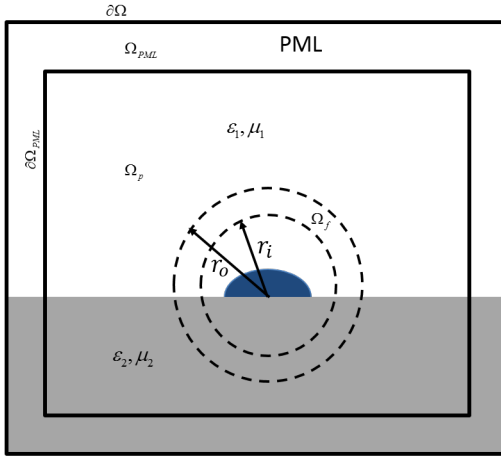


Figure 2.12: A typical solution domain used to model scattering problems.

Since inside the PML we can only have the scattered field, the Maxwell's equations are

$$\begin{cases} \tilde{\nabla} \times \tilde{\nabla} \times \mathbf{E} - k^2(\mathbf{r})\mathbf{E} = 0 & \mathbf{r} \in \Omega_p \cup \Omega_{PML}, \\ \llbracket \gamma_t(\mathbf{E}) \rrbracket = \gamma_t(\mathbf{E}_i) & \mathbf{r} \in \partial\Omega_{PML}, \\ \llbracket \gamma_t(\tilde{\nabla} \times \mathbf{E}) \rrbracket = \gamma_t(\tilde{\nabla} \times \mathbf{E}_i) & \mathbf{r} \in \partial\Omega_{PML}, \\ \gamma_t(\tilde{\nabla} \times \mathbf{E}) = 0 & r \in \partial\Omega, \end{cases} \quad (2.73)$$

where $\tilde{\nabla}$ denotes the derivative with respect to the complex system of coordinates which is used to absorb the wave inside the PML [48, Sec. 13.5.3]. By testing (2.73) with $\mathbf{W} \in H(\text{curl}, \Omega)$, we find \mathbf{E} as the solution to

$$\begin{aligned} \int_{\Omega} \tilde{\nabla} \times \mathbf{E} \cdot \tilde{\nabla} \times \overline{\mathbf{W}} - k^2(\mathbf{r}) \mathbf{E} \cdot \overline{\mathbf{W}} \, d\mathbf{r} & \quad (2.74) \\ & = \int_{\partial\Omega_{PML}} \left((\tilde{\nabla} \times \mathbf{E}_i) \times \hat{n} \right) \cdot \overline{\mathbf{W}} \, ds(\mathbf{r}) \quad \forall \mathbf{W} \in H(\text{curl}, \Omega). \end{aligned}$$

Since \mathbf{E} is discontinuous along $\partial\Omega_{PML}$, we introduce an offset function $\mathbf{E}_o \in H(\text{curl}, \Omega)$ such that

$$\gamma_t(\mathbf{E}_o) = \gamma_t(\mathbf{E}_i) \quad \mathbf{r} \in \partial\Omega_{PML}, \quad (2.75)$$

and consider $\mathbf{E} = \mathbf{E}_q + \alpha(\mathbf{r})\mathbf{E}_o$, where $\mathbf{E}_q \in H(\text{curl}, \Omega)$ and $\alpha(\mathbf{r}) = \begin{cases} 1 & \mathbf{r} \in \Omega_p \\ 0 & \mathbf{r} \in \Omega_{PML} \end{cases}$.

So, \mathbf{E}_q is the solution to the following equation

$$a_0(\mathbf{E}_q, \mathbf{W}) = \ell_0(\mathbf{W}) - a_1(\mathbf{E}_o, \mathbf{W}), \quad (2.76)$$

where $a_0, a_1 : H(\text{curl}, \Omega) \times H(\text{curl}, \Omega) \mapsto \mathbb{C}$ and $\ell_0 : H(\text{curl}, \Omega) \mapsto \mathbb{C}$ are sesquilinear and linear forms defined on $H(\text{curl}, \Omega_p \cup \Omega_{PML})$ such that

$$a_0(\mathbf{u}_1, \mathbf{u}_2) = \int_{\Omega_p \cup \Omega_{PML}} \tilde{\nabla} \times \mathbf{u}_1 \cdot \tilde{\nabla} \times \overline{\mathbf{u}_2} - k^2(\mathbf{r}) \mathbf{u}_1 \cdot \overline{\mathbf{u}_2} \, d\mathbf{r}, \quad (2.77)$$

2 Far field investigation in the presence of substrate

$$a_1(\mathbf{u}_1, \mathbf{u}_2) = \int_{\Omega_p \cup \Omega_{PML}} \alpha(\mathbf{r}) \left(\tilde{\nabla} \times \mathbf{u}_1 \cdot \tilde{\nabla} \times \bar{\mathbf{u}}_2 - k^2(\mathbf{r}) \mathbf{u}_1 \cdot \bar{\mathbf{u}}_2 \right) d\mathbf{r}, \quad (2.78)$$

$$\ell_0(\mathbf{u}_2) = \int_{\partial\Omega_{PML}} \left((\tilde{\nabla} \times \mathbf{E}_i) \times \hat{\mathbf{n}} \right) \cdot \bar{\mathbf{u}}_2 ds(\mathbf{r}). \quad (2.79)$$

Let $X_h \subset H(\text{curl}, \Omega)$ be the finite element space such that $\mathbf{b}_j \in X_h$ are basis functions of X_h , $j = 1, \dots, N$, with $N = \dim X_h$. Any function $\mathbf{u} \in H(\text{curl}, \Omega_p \cup \Omega_{PML})$ can be interpolated in X_h as the following

$$\mathbf{u}_h(\mathbf{r}) = \sum_{j=1}^N g^j \mathbf{b}_j(\mathbf{r}). \quad (2.80)$$

We also define the coefficient-vector of \mathbf{u}_h and the stiffness-matrix of the sesquilinear form a_0 with respect to the basis $\{\mathbf{b}_j\}_{j=1}^N$ as $\mathbf{g} = (g^1, \dots, g^N)^T$ and $\tilde{\mathbf{A}}_0 = (a_0(\mathbf{b}_j, \mathbf{b}_i))_{i,j=1}^N$, respectively ¹. The identity (2.76) can be written in discrete setting as follows

$$\begin{aligned} \tilde{\mathbf{A}}_0 \mathbf{g}_q &= \mathbf{f}_0, \\ \mathbf{f}_0 &= \mathbf{f}_1 - \tilde{\mathbf{A}}_1 \mathbf{g}_o, \end{aligned} \quad (2.81)$$

where $\mathbf{f}_1 = (\ell_0(\mathbf{b}_j))_{j=1}^N$, and $\tilde{\mathbf{A}}_1$ is the stiffness matrix of the sesquilinear form a_1 . By \mathbf{g}_q and \mathbf{g}_o we denote coefficient vectors of \mathbf{E}_q^h and \mathbf{E}_o^h , respectively.

We use 3rd order Nedelec finite elements on a quasi-uniform tetrahedral mesh to solve (2.76) using NGSolve. To assemble the Galerkin matrices $\tilde{\mathbf{A}}_0$ and $\tilde{\mathbf{A}}_1$, we use the sesquilinear-form integrators of NGSolve *PML_curlcurl*edge and *PML_mass*edge, respectively. Similarly, to assemble \mathbf{f}_1 , we use the linear form integrator of NGSolve *neumann*edge.

```
#Interpolating coef_ui = E_i
#within the coefficient vector
#(gridfunction) "uinc"
numproc setvalues npSV
```

¹From now on, all the coefficient vectors and stiffness matrices in this section are with respect to the basis $\{\mathbf{b}_j\}_{j=1}^N$.


```

-gridfunction=uinc -coefficient=coef_ui

#Interpolating "coef_ui_bd = \gamma_t E_i"
#on the boundary of PML within
#the coefficient vector (gridfunction) "go".
numproc setvalues npSV2
-gridfunction=go -coefficient=coef_ui_bd
-boundary

#Defining the sesquilinear form a0.
#The coefficient "lam" is equal to one in
#the whole solution domain.
#The piecewise constant coefficient "rho"
#is equal to values of wavenumbers
#in each subdomain.
define sesquilinearform a0 -fespace=v -noprint
-noprintelmat
PML_curlcurledge lam
PML_massedgedge rho

#Defining the sesquilinear form a1.
#The piecewise constant coefficient "lam1"
#is equal to zero in PML region and equal
#to one in the rest of the solution domain.
#The piecewise constant coefficient "rho1"
#is equal to zero in PML region and equal
#to values of wavenumbers in the rest of
#subdomains.
define sesquilinearform a1 -fespace=v -noprint
-noprintelmat
PML_curlcurledge lam1
PML_massedgedge rho1

```

```

#Defining th right hand side vector "f"
#(the linear form):
#Adding "f1" to f using neumannedge integrator
#"F_neumann=(\curl \VE_i)\times \hat n" on
#the boundary of PML
define linearform f -fespace=v
    neumannedge F_neumann

#Using numproc "JumpDiriUpdate" to add the term
#"A1*go" to "f"
numproc JumpDiriUpdate npD
    -sesquilinearform=a1 -gridfunction=go
    -linearform=f

#Defining the "multigrid" preconditioner
define preconditioner c
    -type=multigrid -sesquilinearform=a
    -ds_order=1 -smoother=block -blocktype=21

numproc bvp np1
    -sesquilinearform=a -linearform=f
    -gridfunction=u -maxsteps=20000
    -noprint -solver=cg -prec=1e-10
    -preconditioner=c

```

To calculate the far-field integral (2.67), we use the sesquilinear form $a_f : H(\text{curl}, \Omega) \times H(\text{curl}, \Omega) \mapsto \mathbb{C}$, which is defined as follows

$$a_f(\mathbf{u}_1, \mathbf{u}_2) = \int_{\Omega_f} \nabla \times \mathbf{u}_1 \cdot \nabla \times \bar{\mathbf{u}}_2 \, d\mathbf{r}. \quad (2.82)$$

Based on (2.67), the far field is

$$\mathbf{E}_\infty \cdot \hat{\ell} = \mathbf{g}_1^T \tilde{\mathbf{A}}_f \mathbf{g}_2 - \mathbf{g}_3^T \tilde{\mathbf{A}}_f \mathbf{g}_4, \quad (2.83)$$

where \mathbf{g}_1 , \mathbf{g}_2 , \mathbf{g}_3 , and \mathbf{g}_4 are coefficient vectors of $\mathbf{E}_s^h = \mathbf{E}_q^h - \mathbf{E}_t^h$, $\Psi^h \mathbf{G}_\infty^h$, $\Psi^h \mathbf{E}^h$, and \mathbf{G}_∞^h , respectively. By $\tilde{\mathbf{A}}_f$ we denote the Galerkin matrix of a_f in (2.82).

The computation cost of our algorithm is mainly due to computing \mathbf{E}_q . Particularly costly are assembling Galerkin matrix $\tilde{\mathbf{A}}_0$ and solving (2.81). The complexity of the matrix inversion depends on the dimension of finite element space but it can be reduced by preconditioning \mathbf{A}_0 and then using iterative solvers. We use conjugate gradient method together with multigrid preconditioner to solve the linear system of equations.

To compute far-field within an aperture, we only need to assemble $\tilde{\mathbf{A}}_f$ and \mathbf{g}_1 once, and update \mathbf{g}_2 , \mathbf{g}_3 , and \mathbf{g}_4 for each value of θ and ϕ . However, when iterating over a range of frequencies, one needs to solve (2.81) for each frequency. We use the Message Passing Interface (MPI) for parallel computation of far-field within a frequency range.

Here is a part of our C++ code to calculate the far field

```

Complex FF_Calculation()
{
  /*Getting the vector of grid functions g1 and
  g2*/
  BaseVector & Vg1=g1->GetVector();
  BaseVector & Vg2=g2->GetVector();

  /*Multiplying the matrix of a_f sesquilinear
  form by Vg2
  ==> temp_B=a_f*Vg2 */
  BaseVector & temp_B=*Vg2.CreateVector();
  a_f->GetMatrix().Mult(Vg2,temp_B);

  /* FF1 = Vg1^T * temp_B */
  Complex FF1 =
    S_InnerProduct<Complex>(Vu_Scattered,temp_B);

```

2 Far field investigation in the presence of substrate

```
/* Getting the vector of grid functions g3 and
   g4 */
   BaseVector & Vg3=g3->GetVector();
   BaseVector & Vg4=g4->GetVector();

/*Multiplying the matrix of a_f sesquilinear
   form by Vg4
   ==> temp_A=a_f*Vg4 */
   BaseVector & temp_A=*Vg4.CreateVector();
   a_F->GetMatrix().Mult(Vg4,temp_A);

/* FF2 = Vg3^T * temp_A */
   Complex FF2 =
       S_InnerProduct<Complex>(Vg3,temp_A);

   Complex FF=FF1-FF2;
   return FF;
}
```

2.6 Numerical results

2.6.1 Dipole over a substrate

In the first numerical experiment, we consider an electric dipole, oriented in the direction normal to the substrate and located at the distance $z' = 0.5\lambda$ from the substrate (see Figure 2.3). By λ we denote the wavelength in free space. The material properties are $(\frac{\epsilon_1}{\epsilon_0}, \frac{\mu_1}{\mu_0}) = (1, 1)$ and $(\frac{\epsilon_2}{\epsilon_0}, \frac{\mu_2}{\mu_0}) = (2, 1)$ in domains $z > 0$ and $z < 0$, respectively (ϵ_0 and μ_0 are the permittivity and permeability of free space). To avoid the singularity of the dipole field solution at the position of the dipole, we consider a sphere around the dipole and solve Maxwell's equations for the total field in the exterior region (see Figure 2.13a).

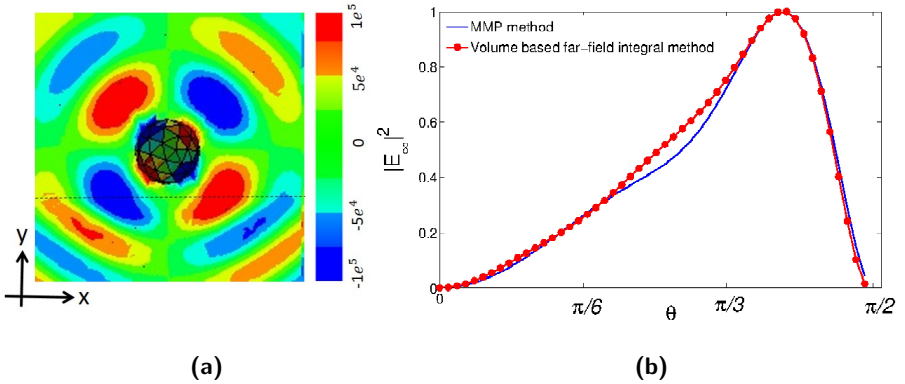


Figure 2.13: An electric dipole located at $z' = 0.5\lambda$, perpendicular to the substrate. $\frac{\epsilon_1}{\epsilon_0} = 1$ and $\frac{\epsilon_2}{\epsilon_0} = 2$ are the relative permittivities for $z > 0$ and $z < 0$, respectively. (a) The finite element solution to the electric field component in the \hat{x} direction. (b) The far-field pattern for $\phi = 0$ and $0 < \theta < \frac{\pi}{2}$.

Figure 2.13b shows a close agreement between the far-field pattern calculated by (2.67) and the method of multiple multipoles (MMP) [4]. MMP is a boundary discretization method based on the field expansion using a series of basis fields. Since the far-field pattern calculation has not been implemented in MMP, we put the observation point at far distances, e.g.

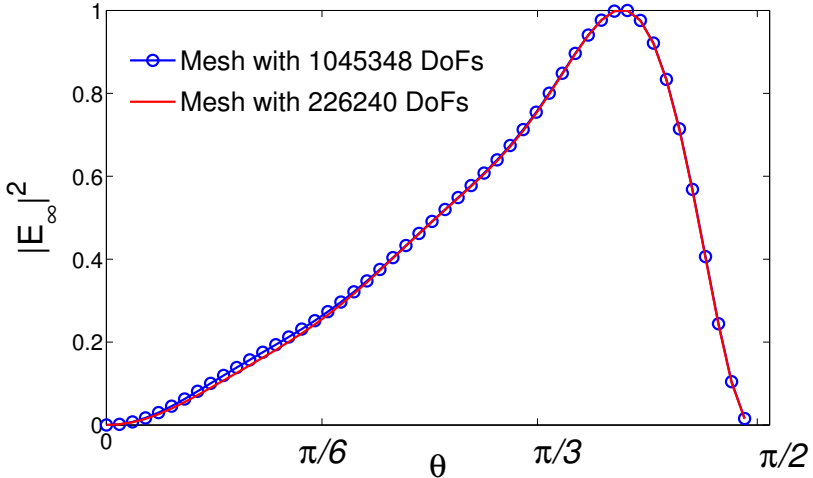


Figure 2.14: Comparison of the far-field pattern calculated within two different finite element meshes. The electric dipole is perpendicular to the substrate ($\frac{\epsilon_1}{\epsilon_0} = 1$ and $\frac{\epsilon_2}{\epsilon_0} = 2$).

$r = 1000\lambda$. The finite element method used to solve Maxwell's equations employs 226246 degrees of freedom (DoFs). Differences between two results decrease asymptotically by refining the finite element mesh and increasing the number of expansions and matching points in the MMP method.

We repeat the calculations for the dipole over the substrate using a different mesh. This time we use a finer mesh with 1045348 DoFs. Based on results shown in Figure 2.14, the far-field pattern is almost independent of the mesh size. The volume based far-field expression is a smooth functional which averages errors over the integration region. Consequently, the local errors arising from the mesh do not have a significant effect on the final result. This fact is due to the higher order convergence of continuous linear output functionals of Galerkin solutions.

Based on Proposition 5 the far-field pattern must be independent of the integration path. To investigate this fact, we consider three different an-

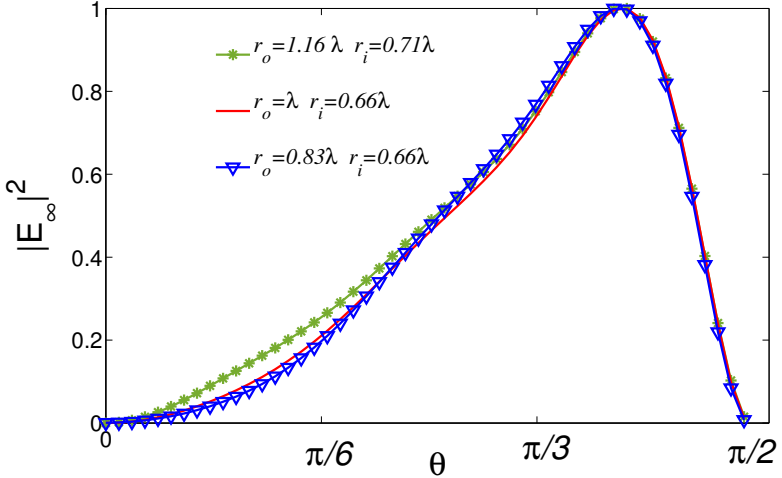


Figure 2.15: The far-field pattern calculated using three different integration regions. Integration domains are annuli with inner radius r_i and the outer radius r_o . The electric dipole is perpendicular to the substrate ($\frac{\epsilon_1}{\epsilon_0} = 1$ and $\frac{\epsilon_2}{\epsilon_0} = 2$), and the mesh has 226246 DoFs.

nuli with $(r_o, r_i) = (1.16\lambda, 0.71\lambda)$, $(\lambda, 0.66\lambda)$ and $(0.83\lambda, 0.66\lambda)$ as far-field integration regions (r_o and r_i are the outer and inner radii of the annulus, respectively) and simulate the structure using a mesh with 226246 DoFs. The results confirm our expectation and are close to each other (see Figure 2.15). The slight differences between results arise from the fact that we plug in the FEM solution in (2.67). When the finite element solution is employed instead of the exact solution to evaluate the far-field formula, the path independence breaks down.

For code validation, we consider the same material properties for the substrate as free space, $(\frac{\epsilon_1}{\epsilon_0}, \frac{\mu_1}{\mu_0}) = (\frac{\epsilon_2}{\epsilon_0}, \frac{\mu_2}{\mu_0}) = (1, 1)$. Under this assumption, we have the well-known problem of a dipole in free-space (see Figure 2.16a). For a dipole in free-space there exists an analytic solution $\mathbf{E}_\infty(\hat{\mathbf{r}}) = -\frac{i\omega\mu}{4\pi} \sin\theta \hat{\theta}$ (see [28, Page 447]). Figure 2.16b compares the far-field pattern of a dipole

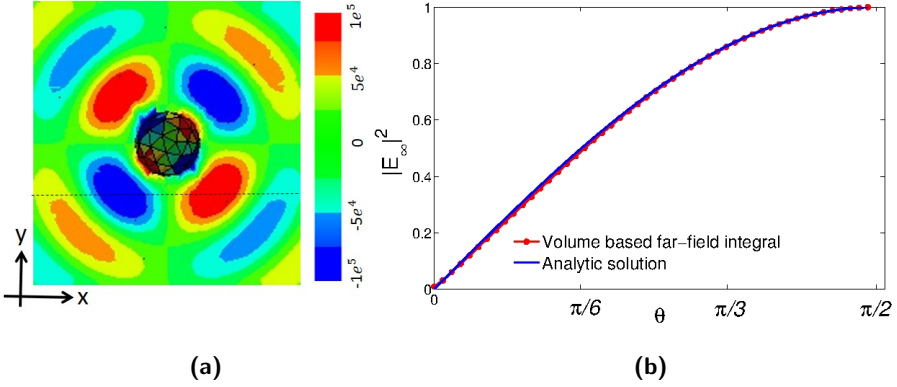


Figure 2.16: An electric dipole in free-space, located at $z' = 0.5\lambda$ and oriented in direction \hat{z} . (a) The finite element solution to the electric field component in the \hat{x} direction. (b) The far-field pattern for $\phi = 0$ and $0 < \theta < \frac{\pi}{2}$.

in free-space derived by (2.67) with the analytic solution for $\phi = 0$ and $0 < \theta < \frac{\pi}{2}$.

2.6.2 Nanoparticle over a substrate

In this section, we analyze plasmon resonances of gold nanoparticles in the presence of a glass substrate (see Figure 2.17a). Reto Gianini in his dissertation had measured the scattering spectra of several cylindrical gold NPs (nanoparticles)[27]. In the first part of this section, we try to reproduce the results discussed in [27, Section 3.2]. The nanoparticle is an elliptical gold cylinder. The three principal axes of the cylinder are a , b , and h (see Figure 2.17b).

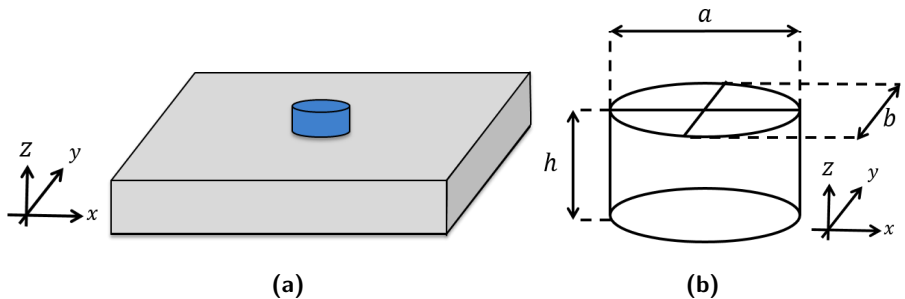


Figure 2.17: (a) Cylindrical nanoparticle mounted on a glass substrate with (b) 3 principal axes a , b , and h .

As shown in [27, Section 3.1], the dipolar resonance of the structure depends on the direction of the excitation. To investigate this phenomenon, we illuminate the structure with an incident electric field parallel to one of the in-plane axes (a -axis or b -axis).

As mentioned earlier, the NP and the substrate are made of gold and glass, respectively. The refractive index of glass is $n_2 \approx 1.5$. However, gold is a dispersive material within the spectrum of visible light. There have been several measurements to derive the optical constants of gold [39, 56]. In this thesis, we use the data given in [39].

In [27], the field is collected through an objective lens with the opening angle of $\alpha = 74^\circ$ and centered on the z -axis. In order to come close to this experiment, we consider the following integration as the far-field measure-

ment

$$Q(\lambda) = \int_{\Omega_{lens}} |\mathbf{E}_{\infty}(\mathbf{r}, \lambda)|^2 d\mathbf{r} \quad (r \rightarrow \infty). \quad (2.84)$$

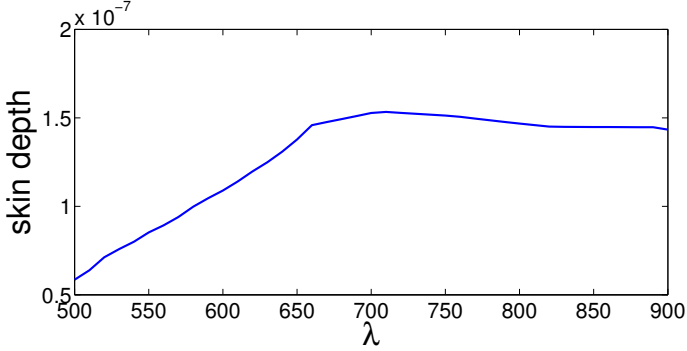


Figure 2.18: Skin depth of gold.

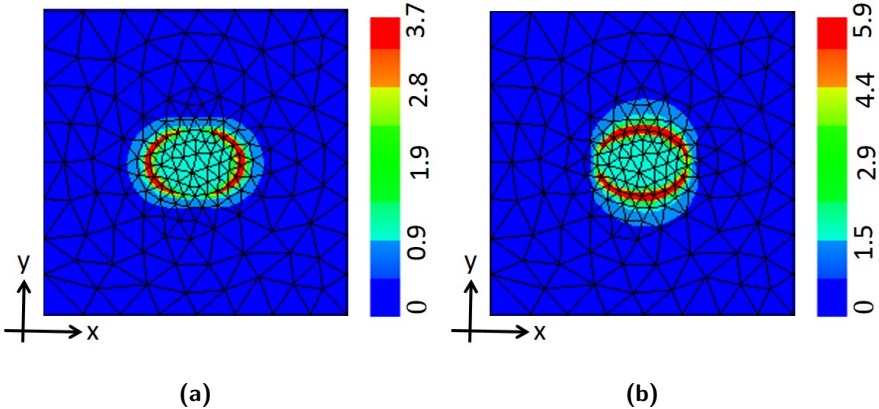


Figure 2.19: The absolute value of the scattered field of a cylindrical NP with elliptical footprint $(a, b, h) = (132, 95, 110)nm$. The incident electric field is parallel to (a) a-axis (b) b-axis.

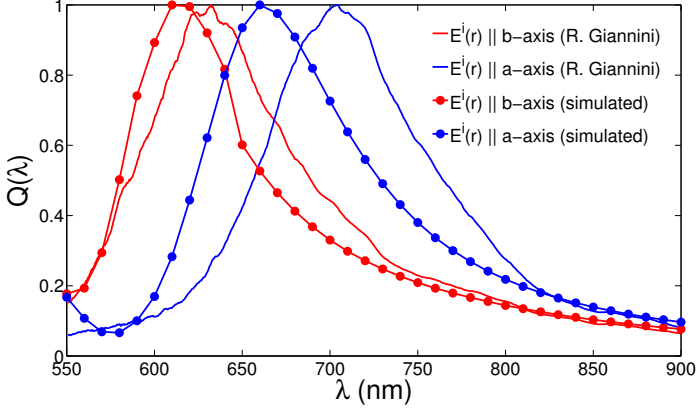


Figure 2.20: Normalized energy flux of a cylindrical NP with an elliptical footprint $(a, b, h) = (132, 95, 110) \text{ nm}$. The incident electric field $\mathbf{E}^i(\mathbf{r})$ is either parallel to the a -axis or b -axis. The measurement results are obtained from [27, Figure 3.1].

where Ω_{lens} is the area of the objective, λ is the wavelength in free space and $Q(\lambda)$ is the energy flux through the lens. To determine the mesh size, we keep in mind that gold is a lossy material, and the electromagnetic field decays rapidly inside it. There is a measure called skin depth to show how deep the electromagnetic field can penetrate inside the conductor [40, Section 5.14]. The mesh size must be small enough to model the wave attenuation within the skin depth. The smallest skin depth of gold in the range of $\lambda = [500 : 900] \text{ nm}$ is 59 nm (see Figure 2.18). So, we choose the biggest mesh size $\Delta h \approx 50 \text{ nm}$ in our simulations (see Figure 2.19).

Figure 2.20 shows the normalized $Q(\lambda)$ of a cylindrical NP with elliptical footprint, $(a, b, h) = (132, 95, 110) \text{ nm}$. The Figure compares the results calculated by (2.67) with measurement results reported in [27, Figure 3.1]. Both measurements and calculations show the resonance-frequency shift by changing the direction of the incident electric field. Based on calculations, $\lambda_a = 660 \text{ nm}$ and $\lambda_b = 610 \text{ nm}$ correspond to plasmon resonance frequencies when the incident electric field is parallel to a -axis or b -axis, respectively. As it is shown in Figure 2.20, shapes of resonance curves are the same for measurements and simulation results. However, there is a frequency shift

2 Far field investigation in the presence of substrate

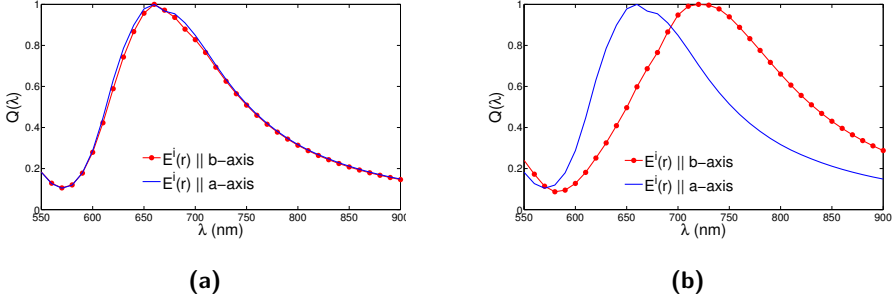


Figure 2.21: Normalized energy flux of a cylindrical NP with an elliptical footprint (a) $(a, b, h) = (132, 132, 110) \text{ nm}$ and (b) $(a, b, h) = (132, 160, 110) \text{ nm}$. The incident electric field $\mathbf{E}^i(\mathbf{r})$ is either parallel to the a -axis or b -axis.

between them. The disagreement between measurements and simulations can be due to different facts:

- The shape inaccuracy of fabricated NPs:
Shape uncertainty is inevitable during the fabrication procedure. This causes changes in the size of NPs which has a direct effect on the resonance frequency. To investigate the effect of the axis size on the performance of NP, we change the size of b -axis to 132 nm and 160 nm while the sizes of a and h axes are fixed. λ_b shifts to the right by increasing the axis size, whereas λ_a remains almost constant (see Figures 2.21a and 2.21b). Based on this experiment, any changes in the the shape of NP has a direct effect on the resonance frequency.
- Material properties of gold:
Material properties of gold depend on the sample preparation procedure. The data given by [39, 56] are based on measurements on specific conditions which are not fully adequate in our experiments. To see how sensitive $Q(\lambda)$ is to the gold characteristics, we repeat the calculations for the elliptical footprint $(a, b, h) = (132, 95, 110) \text{ nm}$ using the data given by Palik [56] and compare them with the results based on Johnson and Christy [39]. As one can see, the resonance frequency is not affected significantly by the changes in the gold data

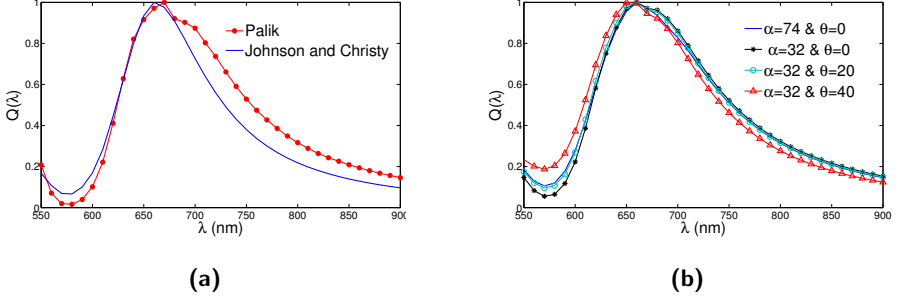


Figure 2.22: Normalized energy flux of a cylindrical NP with elliptical footprint $(a, b, h) = (132, 95, 110)nm$ calculated (a) using different databases for optical constants of gold (b) by lenses with different opening angle (α) and centered at different angles with respect to the z -axis (β).

obtained from different measurements, but the shape of the resonance curve changes (see Figure 2.22a). From the curve obtained using Palik’s data, one even might think that a second resonance is present near $700nm$. But this is only because of material properties.

- The size and the location of the objective:
The effect of the size and the position of the objective on the normalized energy flux is investigated using lenses centered at different angles with respect to the z -axis β , and with different opening angles α . The results show that $Q(\lambda)$ is almost independent of the objective lens parameters (see Figure 2.22b).

Based on the discussion above, the shape inaccuracy of fabricated NPs plays the most significant role in causing differences between simulation and measurement results.

The size effect has been studied even more closely in [27, Figure 6.1]. It shows how the resonance frequency of different cylindrical NPs depends on the size of the in-plane axis. The b -axis is kept constant and the a -axis changes $80 < a < 190nm$. We repeat the same experiment with the elliptical foot print, $b = 120nm$ and $h = 20nm$ and compare them with measurements (see Figure 2.23). As one can see, a good agreement between simulations and measurements is observed. λ_b reduces rapidly for small

2 Far field investigation in the presence of substrate

values of in-plane axial ratio ($\frac{a}{b} < 1$), but it remains almost constant for axial ratios bigger than 1 (See Figure 2.23a). However, λ_a increases by increasing the a -axis size (see Figure 2.23b).

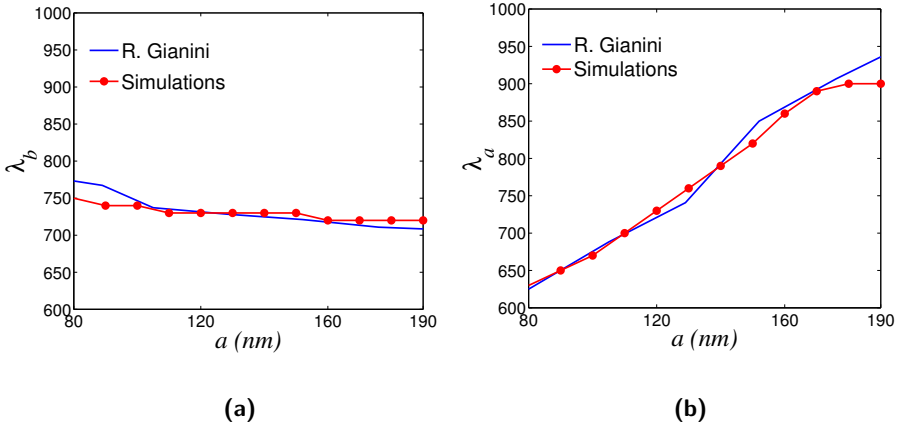


Figure 2.23: Dependence of the resonance frequency on the size of principal axis. The footprint is elliptical and $(a, b, h) = (80 : 190, 120, 20)$ nm. The incident electric field is parallel to (a) b -axis and (b) a -axis. The measurement results are from [27, Figure 6.1].

3 Shape Gradient: Evaluation and Approximation

This chapter has been partly published in BIT journal [34]. Ralf Hiptmair had contributed in the theory part to derive shape gradients and prove Theorem 9. Alberto Paganini contributed closely in the simulation part.

3.1 Introduction

Shape calculus studies the differentiation of shape functionals with respect to the variation of a domain they depend upon. Derivations of shape gradients for scalar problems have been studied thoroughly during the last decades [21–23, 61, 63]. Shape calculus has also become important as a key tool in the field of optimization, where it supplies the so-called shape gradient, i.e. the first derivative of a functional with respect to a shape, for use in the framework of descent methods [12, 42, 57, 63].

The first part of this chapter, is associated to the derivation of shape gradients for PDE constraint shape functionals. The PDE constraint which is called the state problem, can be any boundary value problem. We restrict ourselves to second order-elliptic BVPs, and in the 3D case we specifically consider Maxwell’s equations for scattering problems which is the main focus of this thesis. We use the Lagrangian approach to derive the shape gradient based on solutions of adjoint and state problems.

Derivation of shape gradients for Maxwell’s equations gets more complicated due to the regularity preservation [13, 15]. In Section 3.3.2, it is discussed that we need to use the covariant transformation in order to guarantee that solutions of adjoint and state problems in the mapped domain are still $H(\text{curl}; \Omega)$ functions.

We obtain shape gradients in two equivalent ways, (i) as expressions involving traces of state and adjoint solutions on the boundary of the domain, and (ii) by means of volume integrals on the domain. The situation resembles the result for far-field functional in Chapter 2. In equation (2.60) and (2.67) we represent the far-field functional in terms of boundary and volume integrals, respectively. There are other examples of output functionals depending on solutions of BVPs for second-order elliptic PDEs which can be stated as integrals either over boundaries or over parts of the domain, e.g lift functionals for potential flow [29] and electromagnetic force functionals [46]. Both formulas give the same result if exact solutions of BVPs are inserted, but when applied to discrete solutions, they fail to give the same answer. More strikingly, the volume integrals often display much faster convergence and provide superior accuracy compared to their boundary based counterparts. This makes a crucial difference, because we can benefit from superb convergence, when evaluating continuous functionals for Galerkin solutions [6, Sec. 2]. This made us suspect that similar effects could be observed for the different expressions for shape gradients and their use with finite element solutions. Hence, in the second part of this chapter, we investigate the a priori convergence estimates for boundary and volume integrals in both 2D and 3D problems. We also conduct some numerical experiments to study convergence rates of different representations of the shape gradient within different geometries in 2D. The numerical results confirm the theoretical expectations.

3.2 Shape gradients

Let $\Omega \subset \mathbb{R}^d$, $d = 2, 3$, be an open bounded domain with piecewise smooth boundary $\partial\Omega$, and let $\mathcal{J}(\Omega) \in \mathbb{R}$ be a real-valued quantity of interest associated to it. One is often interested in the shape sensitivity, which quantifies the impact of small perturbations of the domain shape on the value $\mathcal{J}(\Omega)$.

For this purpose, we model perturbations of the domain Ω through maps of the form

$$T_{\mathcal{V}}(\mathbf{r}) : \begin{cases} \mathbb{R}^d \rightarrow \mathbb{R}^d \\ \mathbf{r} \rightarrow \mathbf{r} + \mathcal{V}(\mathbf{r}), \end{cases} \quad (3.1)$$

where $\mathbf{r} \in \mathbb{R}^d$ denotes the location and \mathcal{V} is a vector field in $C^1(\mathbb{R}^d; \mathbb{R}^d)$. It can be proven that the map (3.1) is a diffeomorphism for $\|\mathcal{V}\|_{C^1} < 1$ [3, Lemma 6.13]. Therefore, it is natural to consider $\mathcal{J}(\Omega)$ as the realization of a shape functional, a real map

$$\mathcal{J} : \mathcal{A} \rightarrow \mathbb{R},$$

defined on the family of admissible domains

$$\mathcal{A} := \{T_{\mathcal{V}}(\Omega) ; \mathcal{V} \in C^1(\mathbb{R}^d; \mathbb{R}^d), \|\mathcal{V}\|_{C^1} < 1\}.$$

The sensitivity of $\mathcal{J}(\Omega)$ with respect to the perturbation direction \mathcal{V} can be expressed through the *Eulerian derivative* of the shape functional \mathcal{J} in the direction \mathcal{V} , that is,

$$d\mathcal{J}(\Omega; \mathcal{V}) := \lim_{s \searrow 0} \frac{\mathcal{J}(T_{s, \mathcal{V}}(\Omega)) - \mathcal{J}(\Omega)}{s}. \quad (3.2)$$

It goes without saying that it is desirable that (3.2) exists for all possible perturbation directions \mathcal{V} . It is therefore natural to define a shape functional \mathcal{J} to be *shape differentiable* at Ω if the mapping

$$d\mathcal{J}(\Omega; \cdot) : C^1(\mathbb{R}^d; \mathbb{R}^d) \rightarrow \mathbb{R}, \quad \mathcal{V} \mapsto d\mathcal{J}(\Omega; \mathcal{V})$$

defined by (3.2) is linear and bounded on $C^1(\mathbb{R}^d; \mathbb{R}^d)$.

Remark 7. *In literature, perturbations as in (3.1) are known as perturbations of the identity. From a differential geometry point of view, this approach is less general than the so called velocity method, which is, for instance, introduced in [21, Ch. 4]. However, both methods lead to the same formula for the shape gradient, which merely takes into account first order perturbations of the shape functional \mathcal{J} [21, Ch. 9, Thm 3.2].*

We are particularly interested in PDE constrained shape functionals of the form

$$\mathcal{J}(\Omega) = \int_{\Omega} j(u) \, d\mathbf{x}, \quad (3.3)$$

where u is the solution to the *state problem*, an elliptic equation with Neumann, Dirichlet, or transmission boundary conditions.

3.3 Derivation of shape gradient

A PDE constrained shape functional can be treated as an equality constraint control problem. Using Lagrangian multipliers to derive the shape gradient yields a dual variable which is the solution to the adjoint problem [21, Ch. 10]. In this section, we concentrate on the derivation of shape gradients for two generic examples. The first one considers a shape functional constrained with an scalar state problem. We discuss the procedure for equations with Dirichlet and Neumann boundary conditions. The second example deals with 3D Maxwell's equations. In this case, we treat a physical scattering problem with transmission boundary condition.

3.3.1 Scalar problems

Let the scalar function u be the solution to the *state problem*, a scalar elliptic equation with Neumann or Dirichlet boundary conditions

$$\begin{cases} \mathcal{L}(u) = f & \text{in } \Omega, \\ u = g \text{ or } \frac{\partial u}{\partial \mathbf{n}} = g & \text{on } \partial\Omega. \end{cases} \quad (3.4)$$

Functions f and g are assumed to belong to $L^2(\mathbb{R}^d)$ ($H^1(\mathbb{R}^d)$ in the case of the Neumann BVP) and $H^2(\mathbb{R}^d)$, respectively, and they are identified with their restrictions onto Ω and $\partial\Omega$.

We consider the following PDE constrained shape functional

$$\mathcal{J}(\Omega) = \int_{\Omega} j(u) \, d\mathbf{r}, \quad (3.5)$$

where $j : \mathbb{R} \rightarrow \mathbb{R}$.

Explicit formulas for the Eulerian derivative of $\mathcal{J}(\Omega)$ can be derived. It can be shown that the obtained formulas involve integrals of u , the solution to (3.4), and of p , the solution to the adjoint problem¹

$$\begin{cases} \mathcal{L}(p) = j'(u) & \text{in } \Omega, \\ p = 0 \text{ or } \frac{\partial p}{\partial \mathbf{n}} = 0 & \text{on } \partial\Omega, \end{cases} \quad (3.6)$$

¹For simplicity, we assume that the operator \mathcal{L} is self-adjoint.

where j' is the derivative of j with respect to u . As different \mathcal{L} results in different shape gradients, we provide $d\mathcal{J}$ for a model state problem in proposition 7.

Proposition 7. *Let u be the solution to the following PDE*

$$\begin{cases} -\Delta u + u &= f & \text{in } \Omega, \\ u &= g \text{ or } \frac{\partial u}{\partial \mathbf{n}} = g & \text{on } \partial\Omega. \end{cases} \quad (3.7)$$

then the shape gradients of the PDE constrained shape functional (3.5) for Dirichlet and Neumann BVPs read

$$\begin{aligned} d\mathcal{J}(\Omega; \mathcal{V}) &= \int_{\Omega} \left(\nabla u \cdot (\mathbf{D}\mathcal{V} + \mathbf{D}\mathcal{V}^T) \nabla p - f\mathcal{V} \cdot \nabla p \right. \\ &\quad \left. + \operatorname{div} \mathcal{V}(j(u) - \nabla u \cdot \nabla p - up) \right. \\ &\quad \left. + (j'(u) - p)(\nabla g \cdot \mathcal{V}) - \nabla p \cdot \nabla(\nabla g \cdot \mathcal{V}) \right) d\mathbf{x}, \end{aligned} \quad (3.8)$$

and

$$\begin{aligned} d\mathcal{J}(\Omega; \mathcal{V}) &= \int_{\Omega} \left((\nabla f \cdot \mathcal{V})p + \nabla u \cdot (\mathbf{D}\mathcal{V} + \mathbf{D}\mathcal{V}^T) \nabla p \right. \\ &\quad \left. + \operatorname{div} \mathcal{V}(fp + j(u) - \nabla u \cdot \nabla p - up) \right) d\mathbf{x} \\ &\quad + \int_{\partial\Omega} (\nabla g \cdot \mathcal{V})p + gp \operatorname{div}_{\Gamma} \mathcal{V} ds(\mathbf{r}), \end{aligned} \quad (3.9)$$

respectively. By p we denote the solution to the following adjoint problem

$$\begin{cases} -\Delta p + p &= j'(u) & \text{in } \Omega, \\ u &= 0 \text{ or } \frac{\partial u}{\partial \mathbf{n}} = 0 & \text{on } \partial\Omega. \end{cases} \quad (3.10)$$

Proof. We start the proof with Dichlet BVP.

Similar to the procedure in [21, Ch. 10, Sec. 5], we define the following Lagrangian form

$$\mathcal{L}(\Omega, v, q, \xi) := \int_{\Omega} j(v) + (\Delta v - v + f)q d\mathbf{r} + \int_{\partial\Omega} \xi(g - v) ds(\mathbf{r}), \quad (3.11)$$

3 Shape Gradient: Evaluation and Approximation

where functions v , q and ξ are in $H^2(\mathbb{R}^d)$. Performing integration by parts, the Lagrangian can be rewritten as

$$\begin{aligned} \mathcal{L}(\Omega, v, q, \xi) &= \int_{\Omega} j(v) - \nabla v \cdot \nabla q - v q + f q \, d\mathbf{r} + \int_{\partial\Omega} \frac{\partial v}{\partial \mathbf{n}} q + \xi(g - v) \, ds(\mathbf{r}), \\ &= \int_{\Omega} j(v) + (\Delta q - q)v + f q \, d\mathbf{r} + \int_{\partial\Omega} \frac{\partial v}{\partial \mathbf{n}} q - \frac{\partial q}{\partial \mathbf{n}} v + \xi(g - v) \, ds(\mathbf{r}), \end{aligned}$$

where \mathbf{n} is the unit normal vector to the surface $\partial\Omega$.

The saddle point of $\mathcal{L}(\Omega, \cdot, \cdot, \cdot)$ is characterized by setting the Frechet derivative of \mathcal{L} with respect to v , q and ξ to zero

$$\left\langle \frac{\partial \mathcal{L}(\Omega, v, q, \xi)}{\partial v}, \phi \right\rangle_{\Omega} = \left\langle \frac{\partial \mathcal{L}(\Omega, v, q, \xi)}{\partial q}, \phi \right\rangle_{\Omega} = \left\langle \frac{\partial \mathcal{L}(\Omega, v, q, \xi)}{\partial \xi}, \phi \right\rangle_{\partial\Omega} = 0 \quad (3.12)$$

for all $\phi \in H^2(\mathbb{R}^d)$, which, leads to

$$\begin{cases} -\Delta v + v = f & \text{in } \Omega, \\ v = g & \text{on } \partial\Omega, \end{cases} \quad (3.13a)$$

$$\begin{cases} -\Delta q + q = j'(v) & \text{in } \Omega, \\ q = 0 & \text{on } \partial\Omega, \end{cases} \quad (3.13b)$$

$$\xi = -\frac{\partial q}{\partial \mathbf{n}} \quad \text{on } \partial\Omega. \quad (3.13c)$$

Thus, for Ω fixed we have

$$\mathcal{J}(\Omega) = \inf_{v \in H^2(\mathbb{R}^d)} \sup_{q, \xi \in H^2(\mathbb{R}^d)} \mathcal{L}(\Omega, v, q, \xi), \quad (3.14)$$

because

$$\mathcal{J}(\Omega) = \mathcal{L}(\Omega, u, q, \xi) \quad \forall q, \xi \in H^2(\mathbb{R}^d).$$

Recall that the material derivative of a generic scalar function f with respect to the deformation $T_{\mathbf{v}}$ is defined as

$$\dot{f} := \lim_{s \searrow 0} \frac{f^s - f}{s}.$$

where $f^s = f \circ T_{s,\mathcal{V}}$.

To compute the Eulerian derivative of $\mathcal{J}(\Omega)$, the Correa-Seeger theorem can be applied on the right-hand side of (3.14) [21, Ch. 10, Sec. 6.3], so that a formula for $d\mathcal{J}(\Omega)$ can be obtained by evaluating the Eulerian derivative of the Lagrangian (3.11) in its saddle point. For $T_{\mathcal{V}}(\mathbf{r}) := \mathbf{r} + \mathcal{V}(\mathbf{r})$, the Lagrangian in the transformed domain reads

$$\begin{aligned} \mathcal{L}(T_{s,\mathcal{V}}(\Omega), v, q, \xi) = & \int_{T_{s,\mathcal{V}}(\Omega)} j(v) - \nabla v \cdot \nabla q - v q + f q \, d\mathbf{r} + \int_{T_{s,\mathcal{V}}(\partial\Omega)} \frac{\partial v}{\partial \mathbf{n}} q + \xi(g - v) \, ds(\mathbf{r}) = \\ & \int_{\Omega} (j(v^s) - \nabla v^s \cdot DT_{s,\mathcal{V}}^{-1} DT_{s,\mathcal{V}}^{-T} \nabla q^s - v^s q^s + f^s q^s) |\det DT_{s,\mathcal{V}}| \, d\mathbf{r} \\ & + \int_{\partial\Omega} \left(\frac{\partial v^s}{\partial \mathbf{n}} q^s + \xi^s (g^s - v^s) \right) \|M(T_{s,\mathcal{V}}) \cdot \mathbf{n}\|_{\mathbb{R}^d} \, ds(\mathbf{r}), \end{aligned} \quad (3.15)$$

where $DT_{s,\mathcal{V}}$ is the Jacobian matrix of $T_{s,\mathcal{V}}$, and $M(T_{s,\mathcal{V}})$ is the cofactor matrix of the Jacobian.

It can be shown that [63, Ch. 2]

$$\begin{cases} (\det DT_{s,\mathcal{V}}) = 1 + s \nabla \cdot \mathcal{V} + O(s^2) \\ \|M(T_{s,\mathcal{V}}) \cdot \mathbf{n}\|_{\mathbb{R}^d} = 1 + s \nabla_t \mathcal{V} + O(s^2) \end{cases} \quad s \rightarrow 0, \quad (3.16)$$

where $\nabla_t \mathcal{V} = \nabla \cdot \mathcal{V} - \langle D\mathcal{V} \cdot \mathbf{n}, \mathbf{n} \rangle$.

Plugging (3.16) into (3.15), one can derive the Eulerian derivative of \mathcal{L} as follows

$$\begin{aligned} \lim_{s \searrow 0} \frac{\mathcal{L}(T_{s,\mathcal{V}}(\Omega), v, q, \xi) - \mathcal{L}(\Omega, v, q, \xi)}{s} = & \int_{\Omega} (j'(v)\dot{v} - \nabla \dot{v} \cdot \nabla q - \nabla v \cdot \nabla \dot{q} + \nabla v \cdot (D\mathcal{V} + D\mathcal{V}^T)\nabla q \\ & - \dot{v} q - v \dot{q} + \dot{f}q + f\dot{q} + \nabla \cdot \mathcal{V} (j(v) - \nabla v \cdot \nabla q - v q + f q)) \, d\mathbf{r} \\ & + \int_{\partial\Omega} \frac{\partial \dot{v}}{\partial \mathbf{n}} q + \frac{\partial v}{\partial \mathbf{n}} \dot{q} + \xi(\dot{g} - \dot{v}) + \dot{\xi}(g - v) + \nabla_t \mathcal{V} \left(\frac{\partial v}{\partial \mathbf{n}} q + \xi(g - v) \right) \, ds(\mathbf{r}) \end{aligned}$$

3 Shape Gradient: Evaluation and Approximation

$$\begin{aligned}
&= \int_{\Omega} j'(v)\dot{v} + \Delta q \dot{v} - q \dot{v} \, d\mathbf{r} + \int_{\Omega} \Delta v \dot{q} - v \dot{q} + f \dot{q} \, d\mathbf{r} \\
&\quad + \int_{\partial\Omega} \frac{\partial \dot{v}}{\partial \mathbf{n}} q + \xi(g - v) + \nabla_t \mathcal{V} \left(\frac{\partial v}{\partial \mathbf{n}} q + \xi(g - v) \right) ds(\mathbf{r}) \\
&\quad + \int_{\Omega} \nabla v \cdot (D\mathcal{V} + D\mathcal{V}^T) \nabla q + \dot{f} q + \nabla \cdot \mathcal{V} (j(v) - \nabla v \cdot \nabla q - v q + f q) \, d\mathbf{r} \\
&\quad + \int_{\partial\Omega} \xi(\dot{g} - \dot{v}) - \frac{\partial q}{\partial \mathbf{n}} \dot{v} \, ds(\mathbf{r}).
\end{aligned}$$

So, in the saddle point defined by (3.13), we have

$$\begin{aligned}
&\lim_{s \searrow 0} \frac{\mathcal{L}(T_s \cdot \mathcal{V}(\Omega), v, q, \xi) - \mathcal{L}(\Omega, v, q, \xi)}{s} = \tag{3.17} \\
&= \int_{\Omega} \nabla v \cdot (D\mathcal{V} + D\mathcal{V}^T) \nabla q + \dot{f} q + \nabla \cdot \mathcal{V} (j(v) - \nabla v \cdot \nabla q - v q + f q) \, d\mathbf{r} \\
&\quad + \int_{\partial\Omega} - \frac{\partial q}{\partial \mathbf{n}} \dot{g} \, ds(\mathbf{r}) \\
&= \int_{\Omega} (\nabla v \cdot (D\mathcal{V} + D\mathcal{V}^T) \nabla q + \dot{f} q + (j'(v) - q) \dot{g} - \nabla q \cdot \nabla \dot{g} \\
&\quad + \nabla \cdot \mathcal{V} (j(v) - \nabla v \cdot \nabla q - v q + f q)) \, d\mathbf{r}.
\end{aligned}$$

Given that $\dot{f} = \nabla f \cdot \mathcal{V}$ and $\dot{g} = \nabla g \cdot \mathcal{V}$ [63, Page 99], we apply an additional integration by parts on $\dot{f} q$ and rewrite (3.17) as follows

$$\begin{aligned}
&\lim_{s \searrow 0} \frac{\mathcal{L}(T_s \cdot \mathcal{V}(\Omega), v, q, \xi) - \mathcal{L}(\Omega, v, q, \xi)}{s} = \\
&\int_{\Omega} \left(\nabla v \cdot (D\mathcal{V} + D\mathcal{V}^T) \nabla q - f \mathcal{V} \cdot \nabla q + \operatorname{div} \mathcal{V} (j(v) - \nabla v \cdot \nabla q - v q) \right. \\
&\quad \left. + (j'(v) - q)(\nabla g \cdot \mathcal{V}) - \nabla q \cdot \nabla (\nabla g \cdot \mathcal{V}) \right) d\mathbf{x}.
\end{aligned}$$

For Neumann BVPs, we use a similar approach as the Dirichlet BVP and define the following Lagrangian form

$$\mathcal{L}(\Omega, v, q) := \int_{\Omega} j(v) + (\Delta v - v + f)q \, d\mathbf{r} + \int_{\partial\Omega} \left(g - \frac{\partial v}{\partial \mathbf{n}} \right) q \, ds(\mathbf{r}),$$

$$\begin{aligned}
 &= \int_{\Omega} j(v) - \nabla v \cdot \nabla q - v q + f q \, d\mathbf{r} + \int_{\partial\Omega} g q \, ds(\mathbf{r}), \quad (3.18) \\
 &= \int_{\Omega} j(v) + (\Delta q - q)v + f q \, d\mathbf{r} + \int_{\partial\Omega} g q - \frac{\partial q}{\partial \mathbf{n}} v \, ds(\mathbf{r}).
 \end{aligned}$$

Its saddle point is characterized by

$$\begin{cases} -\Delta v + v &= f & \text{in } \Omega, \\ \frac{\partial v}{\partial \mathbf{n}} &= g & \text{on } \partial\Omega, \end{cases} \quad (3.19a)$$

$$\begin{cases} -\Delta q + q &= j'(v) & \text{in } \Omega, \\ \frac{\partial q}{\partial \mathbf{n}} &= 0 & \text{on } \partial\Omega. \end{cases} \quad (3.19b)$$

The Lagrangian in the transformed domain reads

$$\begin{aligned}
 \mathcal{L}(T_{s,\mathcal{V}}(\Omega), v, q, \xi) &= \\
 &\int_{T_{s,\mathcal{V}}(\Omega)} j(v) - \nabla v \cdot \nabla q - v q + f q \, d\mathbf{r} + \int_{T_{s,\mathcal{V}}(\partial\Omega)} g q \, ds(\mathbf{r}) \\
 &= \int_{\Omega} (j(v^s) - \nabla v^s \cdot DT_{s,\mathcal{V}}^{-1} DT_{s,\mathcal{V}}^{-T} \nabla p^s - v^s q^s + f^s q^s) |\det DT_{s,\mathcal{V}}| \, d\mathbf{r} \\
 &\quad (3.20) \\
 &+ \int_{\partial\Omega} g^s q^s \|M(T_{s,\mathcal{V}}) \cdot \mathbf{n}\|_{\mathbb{R}^d} \, ds(\mathbf{r}).
 \end{aligned}$$

Using (3.39), we obtain the Eulerian derivative of (3.18) in the saddle point defined by (3.19) as follows

$$\begin{aligned}
 &\lim_{s \searrow 0} \frac{\mathcal{L}(T_{s,\mathcal{V}}(\Omega), v, q, \xi) - \mathcal{L}(\Omega, v, q, \xi)}{s} = \\
 &\int_{\Omega} \nabla v \cdot (D\mathcal{V} + D\mathcal{V}^T) \nabla q + \dot{f} q + \nabla \cdot \mathcal{V} (j(v) - \nabla v \cdot \nabla q - v q + f q) \, d\mathbf{r} \\
 &\quad + \int_{\partial\Omega} \dot{g} q + \nabla_t \mathcal{V} (g q) \, ds(\mathbf{r}),
 \end{aligned}$$

which after exploiting the identity $\dot{f} = \nabla f \cdot \mathcal{V}$ reads

$$\lim_{s \searrow 0} \frac{\mathcal{L}(T_{s,\mathcal{V}}(\Omega), v, q, \xi) - \mathcal{L}(\Omega, v, q, \xi)}{s} =$$

3 Shape Gradient: Evaluation and Approximation

$$\int_{\Omega} \left((\nabla f \cdot \mathcal{V})q + \nabla u \cdot (\mathbf{D}\mathcal{V} + \mathbf{D}\mathcal{V}^T)\nabla q + \operatorname{div} \mathcal{V}(fq + j(u) - \nabla u \cdot \nabla q - uq) \right) d\mathbf{x} \\ + \int_{\partial\Omega} (\nabla g \cdot \mathcal{V})q + gq \operatorname{div}_{\Gamma} \mathcal{V} ds(\mathbf{r}).$$

□

Proposition 8. ([21, Ch. 9, Thm 3.6], Hadamard structure theorem) *Let J be a real-valued shape functional within domain $\Omega \in \mathbb{R}^d$ with smooth boundary $\partial\Omega$. Then $d\mathcal{J}(\Omega; \cdot)$ admits a representative $\mathbf{g}(\Omega)$ in the space of distributions $\mathcal{D}^k(\partial\Omega)$*

$$d\mathcal{J}(\Omega; \mathcal{V}) = \langle \mathbf{g}(\Omega), \gamma_{\partial\Omega} \mathcal{V} \cdot \mathbf{n} \rangle_{\mathcal{D}^k(\partial\Omega)}, \quad (3.21)$$

where $\gamma_{\partial\Omega} \mathcal{V} \cdot \mathbf{n}$ is the normal component of \mathcal{V} on the boundary $\partial\Omega$.

To derive \mathbf{g} , we need to reformulate (3.8) and (3.9) in terms of boundary integrals using integration by parts. For Dirichlet BVP, we use the following vector calculus identity

$$\nabla u \cdot (\mathbf{D}\mathcal{V} + \mathbf{D}\mathcal{V}^T) \nabla p - \nabla \cdot \mathcal{V} (\nabla u \cdot \nabla p) = \\ \nabla \cdot (\nabla u (\mathcal{V} \cdot \nabla p) + \nabla p (\mathcal{V} \cdot \nabla u) - \mathcal{V} (\nabla u \cdot \nabla p)) - \Delta p (\mathcal{V} \cdot \nabla u) - \Delta u (\mathcal{V} \cdot \nabla p),$$

and rewrite (3.8) as follows

$$d\mathcal{J} = \int_{\partial\Omega} \frac{\partial u}{\partial \mathbf{n}} (\mathcal{V} \cdot \nabla p) + \frac{\partial p}{\partial \mathbf{n}} (\mathcal{V} \cdot \nabla u) - \mathcal{V} \cdot \mathbf{n} (\nabla u \cdot \nabla p) ds(\mathbf{r}) \quad (3.22) \\ - \int_{\Omega} p (\mathcal{V} \cdot \nabla u) + u (\mathcal{V} \cdot \nabla p) + u p \nabla \cdot \mathcal{V} d\mathbf{r} \\ + \int_{\Omega} (j'(u) - p) \mathcal{V} \cdot \nabla g - \nabla p \cdot \nabla (\mathcal{V} \cdot \nabla g) d\mathbf{r} \\ + \int_{\Omega} j'(u) \nabla u \cdot \mathcal{V} + j(u) \nabla \cdot \mathcal{V} d\mathbf{r}.$$

For the second integral in (3.22) we have

$$p (\mathcal{V} \cdot \nabla u) + u (\mathcal{V} \cdot \nabla p) + u p \nabla \cdot \mathcal{V} = \nabla (up) \cdot \mathcal{V} + u p \nabla \cdot \mathcal{V} = \nabla (up \mathcal{V}).$$

Then

$$\int_{\Omega} p(\mathcal{V} \cdot \nabla u) + u(\mathcal{V} \cdot \nabla p) + up \nabla \cdot \mathcal{V} \, d\mathbf{r} = \int_{\partial\Omega} up \mathcal{V} \cdot \mathbf{n} \, ds(\mathbf{r}) = 0.$$

Using integration by parts, the third integral will be

$$\begin{aligned} & \int_{\Omega} (j'(u) - p) \mathcal{V} \cdot \nabla g - \nabla p \cdot \nabla(\mathcal{V} \cdot \nabla g) \, d\mathbf{r} = \\ & \int_{\Omega} (\Delta p - p + j'(u)) \mathcal{V} \cdot \nabla g \, d\mathbf{r} - \int_{\partial\Omega} \frac{\partial p}{\partial \mathbf{n}} \mathcal{V} \cdot \nabla g \, ds(\mathbf{r}) = \int_{\partial\Omega} \frac{\partial p}{\partial \mathbf{n}} \mathcal{V} \cdot \nabla g \, ds(\mathbf{r}). \end{aligned}$$

The fourth integral in (3.22) can be simplified as

$$\begin{aligned} & \int_{\Omega} j'(u) \nabla u \cdot \mathcal{V} + j(u) \nabla \cdot \mathcal{V} \, d\mathbf{r} = \int_{\Omega} \nabla j(u) \cdot \mathcal{V} + j \nabla \cdot \mathcal{V} \, d\mathbf{r} \\ & = \int_{\Omega} \nabla(j(u) \mathcal{V}) \, d\mathbf{r} = \int_{\partial\Omega} j(u) \mathcal{V} \cdot \mathbf{n} \, ds(\mathbf{r}). \end{aligned}$$

Finally, using boundary conditions on u and p , and exploiting identities above, we derive the boundary integral representation for the shape gradient as follows

$$d\mathcal{J}(\Omega; \mathcal{V}) = \int_{\partial\Omega} (\mathcal{V} \cdot \mathbf{n}) \left(j(u) + \frac{\partial p}{\partial \mathbf{n}} \frac{\partial(u-g)}{\partial \mathbf{n}} \right) ds(\mathbf{r}). \quad (3.23)$$

For the Neumann BVP, the boundary integral representative of (3.9) can be obtained by following similar steps as for the Dirichlet BVP, and exploiting the following integration by parts on the boundary

$$\int_{\partial\Omega} (\nabla(gp) \cdot \mathcal{V} + gp \nabla_t \mathcal{V}) \, ds(\mathbf{r}) = \int_{\partial\Omega} \left(\frac{\partial gp}{\partial \mathbf{n}} + \kappa gp \right) \mathcal{V} \cdot \mathbf{n} \, ds(\mathbf{r}), \quad (3.24)$$

where κ is the mean curvature of $\partial\Omega$. The final result reads

$$d\mathcal{J}(\Omega; \mathcal{V}) = \int_{\partial\Omega} \mathcal{V} \cdot \mathbf{n} \left(j(u) - \nabla u \cdot \nabla p - up + fp + \frac{\partial gp}{\partial \mathbf{n}} + \kappa gp \right) ds(\mathbf{r}). \quad (3.25)$$

However, the step (3.24) must be corrected in the presence of nonsmooth boundaries based on Remark 8.

Remark 8. In general, the shape gradient does not feature the Hadamard structure (3.21) if the boundary is piecewise smooth only. For instance, in the presence of corners in 2D, Formula (3.24) and eventually (3.25) have to be corrected by adding the term

$$\sum_i p(\mathbf{a}_i) g(\mathbf{a}_i) \mathcal{V}(\mathbf{a}_i) \cdot [[\tau(\mathbf{a}_i)]], \quad (3.26)$$

where the \mathbf{a}_i denote the corner points and $[[\tau(\mathbf{a}_i)]]$ is the jump of the tangential unit vector field in the corner \mathbf{a}_i [63, Ch. 3.8]. No correction has to be made to formula (3.23).

3.3.2 Electromagnetic shape functional

As a 3D case of study, we investigate the electromagnetic wave scattering problem within the geometry setting of Figure 3.1, and try to derive the shape gradient of an output functional with respect to perturbations of the scatterer boundary $\partial\Omega_s$.

Here, we are mainly interested in an output functional that measures the far-field flux

$$\mathcal{J} = \int_{\Omega_{\text{fens}}} |\mathbf{E}_\infty|^2 d\hat{\mathbf{r}}, \quad (3.27)$$

where

$$\begin{aligned} \mathbf{E}_\infty(\hat{\mathbf{r}}) \cdot \hat{\ell} &= \int_{\Omega_f} \nabla \times \mathbf{E}(\mathbf{r}) \cdot \nabla \times \left(\Psi(\mathbf{r}) \mathbf{G}_\infty(\hat{\mathbf{r}}, \mathbf{r}, \hat{\ell}) \right) \\ &\quad - \nabla \times (\Psi(\mathbf{r}) \mathbf{E}(\mathbf{r})) \cdot \nabla \times \mathbf{G}_\infty(\hat{\mathbf{r}}, \mathbf{r}, \hat{\ell}) \, d\mathbf{r} \\ &= \int_{\Omega_f} \nabla \times \mathbf{E}(\mathbf{r}) \cdot (\nabla \Psi(\mathbf{r}) \times \mathbf{G}_\infty(\hat{\mathbf{r}}, \mathbf{r}, \hat{\ell})) \\ &\quad - \nabla \times \mathbf{G}_\infty(\hat{\mathbf{r}}, \mathbf{r}, \hat{\ell}) \cdot (\nabla \Psi(\mathbf{r}) \times \mathbf{E}(\mathbf{r})) \, d\mathbf{r}. \end{aligned} \quad (3.28)$$

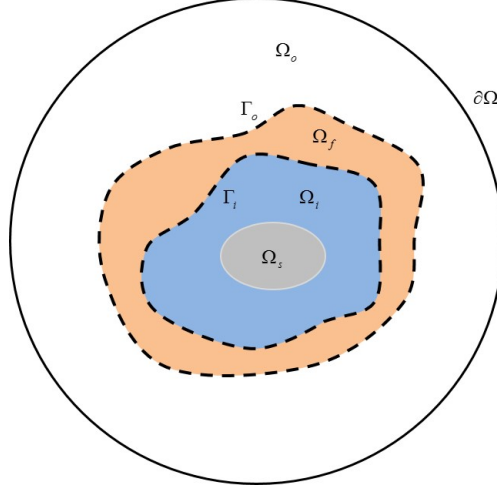


Figure 3.1: The general setting of electromagnetic scattering problem. The far field integration region Ω_f is shown in orange. The outer region shown in white is Ω_o , and by Ω_i we denote the interior part which consists of blue and gray regions. The scatterer is depicted by gray color.

Note that the electric field \mathbf{E} solves the second order Maxwell's equation

$$\begin{cases} \nabla \times \nabla \times \mathbf{E} - k^2(\mathbf{r}) \mathbf{E} = 0 & \mathbf{r} \in \mathbb{R}^3, \\ \llbracket \gamma_t(\mathbf{E}) \rrbracket = 0 & \mathbf{r} \in \partial\Omega_s, \\ \llbracket \gamma_t(\nabla \times \mathbf{E}) \rrbracket = 0 & \mathbf{r} \in \partial\Omega_s, \\ ((\nabla \times \mathbf{E}_s) \times \hat{r} - ik(\mathbf{r}) \mathbf{E}_s) = 0 & r \rightarrow \infty. \end{cases} \quad (3.29)$$

By testing (3.29) with $\mathbf{W} \in H(\text{curl}, \Omega)$, we find $\mathbf{E} \in H(\text{curl}, \Omega)$ as the solution to

$$\begin{aligned} & \int_{\Omega} \nabla \times \mathbf{E} \cdot \nabla \times \overline{\mathbf{W}} - k^2(\mathbf{r}) \mathbf{E} \cdot \overline{\mathbf{W}} \, d\mathbf{r} - \int_{\partial\Omega} \text{DtN}[\mathbf{E}] \cdot \overline{\mathbf{W}} \, ds(\mathbf{r}) = \\ & \int_{\partial\Omega} ((\nabla \times \mathbf{E}_i) \times \hat{n}) \cdot \overline{\mathbf{W}} - \text{DtN}[\mathbf{E}_i] \cdot \overline{\mathbf{W}} \, ds(\mathbf{r}) \quad \forall \mathbf{W} \in H(\text{curl}; \Omega). \end{aligned} \quad (3.30)$$

3 Shape Gradient: Evaluation and Approximation

As explained in Section 2.4, Ψ is the cutoff function such that $\Psi(\mathbf{r})|_{\Gamma_i} \equiv 1$, and $\Psi(\mathbf{r})|_{\Gamma_o} \equiv 0$. By Γ_i and Γ_o we denote the inner and outer boundaries of domain Ω_f , respectively (see Figure 3.1)

For the theory part in Section 3.4, we need to assume that the cutoff function is smooth enough and $\nabla\Psi$ is compactly supported in Ω (see Assumption 3). However, for numerical simulations in Chapter 2 and 4, we simply use the very simple case depicted in (2.72)

Assumption 3. *We choose the cutoff function such that $\Psi \in C^3$ and*

$$\begin{cases} \Psi = 0 & \mathbf{r} \in \Omega_o, \\ \Psi = 1 & \mathbf{r} \in \Omega_i, \\ \nabla\Psi = 0 & \mathbf{r} \in \Gamma_i \cup \Gamma_o. \end{cases} \quad (3.31)$$

Based on Assumption 3, $\nabla\Psi$ is smooth and also compactly supported in Ω . So, we can do one more step of integration by part on (3.28) and rewrite the far field as follows

$$\mathbf{E}_\infty(\hat{\mathbf{r}}) \cdot \hat{\boldsymbol{\ell}} = \int_{\Omega_f} \kappa_f(\mathbf{r}, \hat{\mathbf{r}}) \cdot \mathbf{E}(\mathbf{r}) \, d\mathbf{r}, \quad (3.32)$$

where

$$\kappa_f(\mathbf{r}, \hat{\mathbf{r}}) = \nabla \times (\nabla\Psi(\mathbf{r}) \times \mathbf{G}_\infty(\hat{\mathbf{r}}, \mathbf{r}, \hat{\boldsymbol{\ell}})) - \nabla \times \mathbf{G}_\infty(\hat{\mathbf{r}}, \mathbf{r}, \hat{\boldsymbol{\ell}}) \times \nabla\Psi(\mathbf{r}).$$

Using Assumption 3, we see that $\kappa_f : \mathbb{R}^3 \rightarrow \mathbb{R}^3$ belongs to C^1 and is also compactly supported in Ω . So, we can replace the integration over Ω_f in (3.32) by the integration over domain Ω .

Finally, the derivative of \mathcal{J} with respect to \mathbf{E} is

$$\left\langle \frac{\partial \mathcal{J}}{\partial \mathbf{E}}, \delta \mathbf{E} \right\rangle = \text{Re} \int_{\Omega} \delta \mathbf{E}(\mathbf{r}) \cdot \mathcal{G}(\mathbf{E}, \mathbf{r}) \, d\mathbf{r}, \quad (3.33)$$

where

$$\mathcal{G}(\mathbf{E}, \mathbf{r}) = \int_{\Omega_{\text{tens}}} \kappa_f(\mathbf{r}, \hat{\mathbf{r}}_1) \int_{\Omega} \mathbf{E}(\mathbf{r}_2) \cdot \kappa_f(\mathbf{r}_2, \hat{\mathbf{r}}_1) \, d\mathbf{r}_2 \, d\hat{\mathbf{r}}_1.$$

To start the procedure of deriving the shape gradient of (3.27), we must note that \mathcal{J} is real valued while the constraint (3.30) is complex valued,

therefore the standard Lagrangian approach can not be applied. Following [43], we define the Lagrangian as

$$\begin{aligned} \mathcal{L}(\Omega, \mathbf{U}, \mathbf{P}) = \operatorname{Re} \left\{ \mathcal{J}(\mathbf{U}) + \int_{\Omega} \nabla \times \mathbf{U} \cdot \nabla \times \bar{\mathbf{P}} - k^2(\mathbf{r}) \mathbf{U} \cdot \bar{\mathbf{P}} d\mathbf{r} \right. \\ \left. - \int_{\partial\Omega} \operatorname{DtN}[\mathbf{U}] \cdot \bar{\mathbf{P}} - \operatorname{DtN}[\mathbf{E}_i] \cdot \bar{\mathbf{P}} + ((\nabla \times \mathbf{E}_i) \times \hat{n}) \cdot \bar{\mathbf{P}} ds(\mathbf{r}) \right\}, \end{aligned} \quad (3.34)$$

where functions \mathbf{U} and \mathbf{P} are in $H(\operatorname{curl}; \Omega)$.

Similar to (3.12), we obtain the saddle point of (3.34) for $\mathbf{U}, \mathbf{P} \in H(\operatorname{curl}, \Omega)$ as solutions to

State problem:

$$\begin{aligned} \int_{\Omega} \nabla \times \mathbf{U} \cdot \nabla \times \bar{\mathbf{W}} - k^2(\mathbf{r}) \mathbf{U} \cdot \bar{\mathbf{W}} d\mathbf{r} - \int_{\partial\Omega} \operatorname{DtN}[\mathbf{U}] \cdot \bar{\mathbf{W}} ds(\mathbf{r}) = \\ \int_{\partial\Omega} ((\nabla \times \mathbf{E}_i) \times \hat{n}) \cdot \bar{\mathbf{W}} - \operatorname{DtN}[\mathbf{E}_i] \cdot \bar{\mathbf{W}} ds(\mathbf{r}) \quad \forall \mathbf{W} \in H(\operatorname{curl}, \Omega), \end{aligned} \quad (3.35a)$$

Adjoint problem:

$$\begin{aligned} \operatorname{Re} \left\{ \int_{\Omega} \nabla \times \bar{\mathbf{P}} \cdot \nabla \times \mathbf{W} - k^2(\mathbf{r}) \bar{\mathbf{P}} \cdot \mathbf{W} d\mathbf{r} - \int_{\partial\Omega} \overline{\operatorname{DtN}^*[\mathbf{P}]} \cdot \mathbf{W} ds(\mathbf{r}) \right. \\ \left. - \int_{\Omega} \mathcal{G}(\mathbf{U}) \cdot \mathbf{W} d\mathbf{r} \right\} = 0 \quad \forall \mathbf{W} \in H(\operatorname{curl}, \Omega), \end{aligned} \quad (3.35b)$$

where DtN^* is the adjoint DtN operator such that $\langle \operatorname{DtN}[\mathbf{A}], \mathbf{B} \rangle_{\partial\Omega} = \langle \mathbf{A}, \operatorname{DtN}^*[\mathbf{B}] \rangle_{\partial\Omega}$, where $\mathbf{A}, \mathbf{B} \in H(\operatorname{curl}, \Omega)$ and $\langle \mathbf{A}, \mathbf{B} \rangle_{\partial\Omega} = \int_{\partial\Omega} \mathbf{A} \cdot \mathbf{B} ds(\mathbf{r})$.

Lemma 1. *Let $u \in Y(\Omega)$ and $u : \Omega \mapsto \mathbb{C}$, be the solution to the following variational formulation for all $v \in Y(\Omega)$*

$$\operatorname{Re} \{a(u, v) - \ell(v)\} = 0,$$

3 Shape Gradient: Evaluation and Approximation

where $a : Y \times Y \mapsto \mathbb{C}$ and $\ell : Y \mapsto \mathbb{C}$ are sesquilinear and linear forms defined on $Y(\Omega)$. Then u is the solution to the following weak form for all $v \in Y(\Omega)$

$$a(u, v) - \ell(v) = 0,$$

Proof. If $\arg(a(u, v) - \ell(v)) = \varphi$, then

$$\begin{aligned} e^{-i\varphi}(a(u, v) - \ell(v)) &= a(u, e^{-i\varphi}v) - \ell(e^{-i\varphi}v) \\ &= \operatorname{Re} \{a(u, e^{-i\varphi}v) - \ell(e^{-i\varphi}v)\} \\ &= 0. \end{aligned}$$

□

Using Lemma 1 and (3.35b) we find $\mathbf{P} \in H(\operatorname{curl}, \Omega)$ as the solution to

$$\begin{aligned} \int_{\Omega} \nabla \times \bar{\mathbf{P}} \cdot \nabla \times \mathbf{W} - k^2(\mathbf{r}) \bar{\mathbf{P}} \cdot \mathbf{W} \, d\mathbf{r} - \int_{\partial\Omega} \overline{\operatorname{DtN}^*[\mathbf{P}]} \cdot \mathbf{W} \, ds(\mathbf{r}) \quad (3.36) \\ = \int_{\Omega} \mathcal{G}(\mathbf{U}) \cdot \mathbf{W} \, d\mathbf{r} \quad \forall \mathbf{W} \in H(\operatorname{curl}, \Omega). \end{aligned}$$

The corresponding strong form of (3.36) for $\mathbf{P} \in C^2$ is

$$\begin{cases} \nabla \times \nabla \times \bar{\mathbf{P}} - k^2(\mathbf{r})\bar{\mathbf{P}} = \mathcal{G}(\mathbf{E}) & \mathbf{r} \in \Omega, \\ \llbracket \gamma_t(\bar{\mathbf{P}}) \rrbracket = 0 & \mathbf{r} \in \partial\Omega_s, \\ \llbracket \gamma_t(\nabla \times \bar{\mathbf{P}}) \rrbracket = 0 & \mathbf{r} \in \partial\Omega_s, \\ \nabla \times \bar{\mathbf{P}} \times \hat{\mathbf{n}} = \overline{\operatorname{DtN}^*[\mathbf{P}]} & \mathbf{r} \in \partial\Omega. \end{cases} \quad (3.37)$$

To derive the Eulerian derivative of (3.34), we first need to state an Assumption on \mathcal{V} and also introduce the covariant transformation.

Assumption 4. *The perturbation $\mathcal{V} \in C^1(\mathbb{R}^3, \mathbb{R}^3)$ vanishes on $\partial\Omega$ and inside Ω_f .*

Lemma 2. *The covariant transformation (pull back)*

$$\Psi_{\mathcal{V}} : \begin{cases} H(\text{curl}; T_{\mathcal{V}}(\Omega)) \mapsto H(\text{curl}; \Omega), \\ \mathbf{F} \mapsto DT_{\mathcal{V}}^T (\mathbf{F} \circ T_{\mathcal{V}}), \end{cases}$$

$$\Phi_{\mathcal{V}} : \begin{cases} H(\text{div}; T_{\mathcal{V}}(\Omega)) \mapsto H(\text{div}; \Omega), \\ \mathbf{F} \mapsto \det DT_{\mathcal{V}} (DT_{\mathcal{V}}^{-1} (\mathbf{F} \circ T_{\mathcal{V}})), \end{cases}$$

$$\nabla \times \Psi_{\mathcal{V}}(\mathbf{F}) = \Phi_{\mathcal{V}} (\nabla^{\mathcal{V}} \times \mathbf{F}),$$

is an isomorphism [32]. By $\nabla^{\mathcal{V}}$ we denote the derivative in the transformed domain.

Using Lemma 2, we define the material derivative of the vector function \mathbf{F} with respect to the deformation $T_{\mathcal{V}}$ as

$$\dot{\mathbf{F}} := \lim_{s \searrow 0} \frac{\mathbf{F}^s - \mathbf{F}}{s},$$

where $\mathbf{F}^s = \Psi_{s, \mathcal{V}}(\mathbf{F})$.

The Lagrangian in the transformed domain is

$$\begin{aligned} \mathcal{L}(T_{s, \mathcal{V}}(\Omega), \mathbf{U}, \mathbf{P}) &= \text{Re} \left\{ \mathcal{J}(\mathbf{U}) + \int_{T_{s, \mathcal{V}}(\Omega)} \nabla \times \mathbf{U} \cdot \nabla \times \bar{\mathbf{P}} - k^2(\mathbf{r}) \mathbf{U} \cdot \bar{\mathbf{P}} d\mathbf{r} \right. \\ &\quad \left. - \int_{\partial\Omega} \text{DtN}[\mathbf{U}] \cdot \bar{\mathbf{P}} - \text{DtN}[\mathbf{E}_i] \cdot \bar{\mathbf{P}} + ((\nabla \times \mathbf{E}_i) \times \hat{n}) \cdot \bar{\mathbf{P}} ds(\mathbf{r}) \right\} \\ &= \text{Re} \left\{ \mathcal{J}(\mathbf{U}^s) + \int_{\Omega} \nabla \times \mathbf{U}^s \cdot \frac{DT_{s, \mathcal{V}}}{\det DT_{s, \mathcal{V}}} \frac{DT_{s, \mathcal{V}}^T}{\det DT_{s, \mathcal{V}}} \nabla \times \bar{\mathbf{P}}^s | \det DT_{s, \mathcal{V}}| \right. \\ &\quad \left. - \int_{\Omega} k^2(\mathbf{r}) \mathbf{U}^s \cdot DT_{s, \mathcal{V}}^{-T} DT_{s, \mathcal{V}}^{-1} \bar{\mathbf{P}}^s | \det DT_{s, \mathcal{V}}| d\mathbf{r} \right. \\ &\quad \left. - \int_{\partial\Omega} \text{DtN}[\mathbf{U}^s] \cdot \bar{\mathbf{P}}^s - \text{DtN}[\mathbf{E}_i] \cdot \bar{\mathbf{P}}^s + ((\nabla \times \mathbf{E}_i) \times \hat{n}) \cdot \bar{\mathbf{P}}^s ds(\mathbf{r}) \right\}. \end{aligned} \tag{3.38}$$

3 Shape Gradient: Evaluation and Approximation

Using Tailor expansion, one can simply show that [63, Ch. 2]

$$\begin{cases} (\det DT_{s,\mathcal{V}})^{-1} = 1 - s \nabla \cdot \mathcal{V} + O(s^2) \\ DT_{s,\mathcal{V}}^{-1} = \mathcal{I} - s \mathbf{D}\mathcal{V} + O(s^2) \end{cases} \quad s \rightarrow 0, \quad (3.39)$$

where \mathcal{I} is the identity matrix.

Plugging (3.39) into (3.38), one can derive the Eulerian derivative of (3.34) as follows

$$\begin{aligned} & \lim_{s \searrow 0} \frac{\mathcal{L}(T_{s,\mathcal{V}}(\Omega), \mathbf{U}, \mathbf{P}) - \mathcal{L}(\Omega, \mathbf{U}, \mathbf{P})}{s} = \\ & \text{Re} \left\{ \int_{\Omega} \mathcal{G}(\mathbf{U}) \cdot \dot{\mathbf{U}} \, d\mathbf{r} + \int_{\Omega} \nabla \times \dot{\mathbf{U}} \cdot \nabla \times \bar{\mathbf{P}} + \nabla \times \mathbf{U} \cdot \nabla \times \bar{\mathbf{P}} \right. \\ & + \nabla \times \mathbf{U} \cdot (\mathbf{D}\mathcal{V} + \mathbf{D}\mathcal{V}^{\top}) \nabla \times \bar{\mathbf{P}} - \nabla \cdot \mathcal{V} (\nabla \times \mathbf{U} \cdot \nabla \times \bar{\mathbf{P}}) \\ & - k^2(\mathbf{r}) \left(\dot{\mathbf{U}} \cdot \bar{\mathbf{P}} + \mathbf{U} \cdot \dot{\bar{\mathbf{P}}} - \mathbf{U} \cdot (\mathbf{D}\mathcal{V} + \mathbf{D}\mathcal{V}^{\top}) \bar{\mathbf{P}} + \nabla \cdot \mathcal{V} (\mathbf{U} \cdot \bar{\mathbf{P}}) \right) d\mathbf{r} \\ & \left. - \int_{\partial\Omega} \text{DtN}[\dot{\mathbf{U}}] \cdot \bar{\mathbf{P}} + \text{DtN}[\mathbf{U}] \cdot \dot{\bar{\mathbf{P}}} - \text{DtN}[\mathbf{E}_i] \cdot \dot{\bar{\mathbf{P}}} + ((\nabla \times \mathbf{E}_i) \times \hat{\mathbf{n}}) \cdot \bar{\mathbf{P}} \, ds(\mathbf{r}) \right\}. \end{aligned}$$

So, in the saddle point defined by (3.35), we derive the shape gradient as follows

$$\begin{aligned} d\mathcal{J}(\mathcal{V}, \Omega) = \text{Re} \left(\int_{\Omega} \nabla \times \mathbf{E} \cdot (\mathbf{D}\mathcal{V} + \mathbf{D}\mathcal{V}^{\top}) \nabla \times \bar{\mathbf{P}} + k^2 \mathbf{E} \cdot (\mathbf{D}\mathcal{V} + \mathbf{D}\mathcal{V}^{\top}) \bar{\mathbf{P}} \right. \\ \left. - \nabla \cdot \mathcal{V} (\nabla \times \mathbf{E} \cdot \nabla \times \bar{\mathbf{P}} + k^2(\mathbf{r}) \mathbf{E} \cdot \bar{\mathbf{P}}) d\mathbf{r} \right). \quad (3.40) \end{aligned}$$

Rewriting (3.40) in terms of boundary integrals using vector calculus is not so straight forward as in the scalar case. So, we do similar steps as in [21, Ch. 10, Sec.5.6], and use the following formula

$$\frac{d}{ds} \int_{T_{s,\mathcal{V}}(\Omega)} F(s, \mathbf{r}) \, d\mathbf{r} \Big|_{s=0} = \int_{\partial\Omega_s} \llbracket F(0, \mathbf{r}) \rrbracket \mathcal{V} \cdot \hat{\mathbf{n}} \, ds(\mathbf{r}) + \int_{\Omega} \frac{\partial F}{\partial s}(0, \mathbf{r}) \, d\mathbf{r}. \quad (3.41)$$

Using Assumption 4, we obtain

$$\begin{aligned} \frac{d}{ds} \mathcal{L}(T_s, \mathcal{V}(\Omega), \mathbf{U}, \mathbf{P}) = \operatorname{Re} \left\{ \int_{\partial\Omega_s} \llbracket \nabla \times \mathbf{U} \cdot \nabla \times \bar{\mathbf{P}} - k^2(\mathbf{r}) \mathbf{U} \cdot \bar{\mathbf{P}} \rrbracket \mathcal{V} \cdot \hat{n} ds(\mathbf{r}) \right. \\ \left. + \int_{\Omega} \nabla \times \mathbf{U}' \cdot \nabla \times \bar{\mathbf{P}} - k^2(\mathbf{r}) \mathbf{U}' \cdot \bar{\mathbf{P}} d\mathbf{r} \right. \\ \left. + \int_{\Omega} \nabla \times \mathbf{U} \cdot \nabla \times \bar{\mathbf{P}}' - k^2(\mathbf{r}) \mathbf{U} \cdot \bar{\mathbf{P}}' d\mathbf{r} \right\}, \end{aligned} \quad (3.42)$$

where

$$\mathbf{U}' = \frac{d}{dt} \mathbf{U} \circ T_{\mathcal{V}}^{-1} = -(\nabla \times \mathbf{U}) \times \mathcal{V} - \nabla(\mathcal{V} \cdot \mathbf{U}), \quad (3.43)$$

$$\mathbf{P}' = \frac{d}{dt} \mathbf{P} \circ T_{\mathcal{V}}^{-1} = -(\nabla \times \mathbf{P}) \times \mathcal{V} - \nabla(\mathcal{V} \cdot \mathbf{P}).$$

Now we perform one more step of integration by parts on second and third integrals in (3.42)

$$\begin{aligned} \frac{d}{ds} \mathcal{L}(T_s, \mathcal{V}(\Omega), \mathbf{U}, \mathbf{P}) = \operatorname{Re} \left\{ \int_{\partial\Omega_s} \llbracket \nabla \times \mathbf{U} \cdot \nabla \times \bar{\mathbf{P}} - k^2(\mathbf{r}) \mathbf{U} \cdot \bar{\mathbf{P}} \rrbracket \mathcal{V} \cdot \hat{n} ds(\mathbf{r}) \right. \\ \left. + \int_{\Omega} \nabla \times \nabla \times \mathbf{U} \cdot \bar{\mathbf{P}}' - k^2(\mathbf{r}) \mathbf{U} \cdot \bar{\mathbf{P}}' d\mathbf{r} \right. \\ \left. + \int_{\partial\Omega_s} \llbracket (\gamma_t(\nabla \times \mathbf{U}) \times \hat{n}) \cdot \bar{\mathbf{P}}' \rrbracket ds(\mathbf{r}) \right. \\ \left. + \int_{\Omega} \nabla \times \nabla \times \bar{\mathbf{P}} \cdot \mathbf{U}' - k^2(\mathbf{r}) \bar{\mathbf{P}} \cdot \mathbf{U}' d\mathbf{r} \right. \\ \left. + \int_{\partial\Omega_s} \llbracket (\gamma_t(\nabla \times \bar{\mathbf{P}}) \times \hat{n}) \cdot \mathbf{U}' \rrbracket ds(\mathbf{r}) \right\}. \end{aligned} \quad (3.44)$$

At saddle point (3.29) and (3.37), the second and fourth integrals on the right hand side of (3.44) are zero. We also have the following continuity conditions along the surface of the scatterer

$$\left\{ \begin{array}{ll} \llbracket \gamma_t(\mathbf{E}) \rrbracket = 0 & \mathbf{r} \in \partial\Omega_s, \\ \llbracket \gamma_t(\mathbf{P}) \rrbracket = 0 & \mathbf{r} \in \partial\Omega_s, \\ \llbracket \gamma_t(\nabla \times \mathbf{E}) \rrbracket = 0 & \mathbf{r} \in \partial\Omega_s, \\ \llbracket \gamma_t(\nabla \times \mathbf{P}) \rrbracket = 0 & \mathbf{r} \in \partial\Omega_s, \\ \llbracket \nabla \times \mathbf{E} \cdot \hat{n} \rrbracket = 0 & \mathbf{r} \in \partial\Omega_s, \\ \llbracket \nabla \times \mathbf{P} \cdot \hat{n} \rrbracket = 0 & \mathbf{r} \in \partial\Omega_s. \end{array} \right. \quad (3.45)$$

Using (3.45), we have

$$\begin{aligned} d\mathcal{J} = -\operatorname{Re} \left\{ \int_{\partial\Omega_s} \llbracket k^2(\mathbf{r}) \mathbf{E} \cdot \bar{\mathbf{P}} \rrbracket \mathcal{V} \cdot \hat{n} ds(\mathbf{r}) \right. \\ + \int_{\partial\Omega_s} \llbracket (\gamma_t(\nabla \times \mathbf{E}) \times \hat{n}) \cdot \nabla(\mathcal{V} \cdot \bar{\mathbf{P}}) \rrbracket ds(\mathbf{r}) \\ + \int_{\partial\Omega_s} \llbracket (\gamma_t(\nabla \times \bar{\mathbf{P}}) \times \hat{n}) \cdot \nabla(\mathcal{V} \cdot \mathbf{E}) \rrbracket ds(\mathbf{r}) \\ + \int_{\partial\Omega_s} \llbracket (\gamma_t(\nabla \times \mathbf{E}) \times \hat{n}) \cdot ((\nabla \times \bar{\mathbf{P}}) \times \mathcal{V}) \rrbracket ds(\mathbf{r}) \\ \left. + \int_{\partial\Omega_s} \llbracket (\gamma_t(\nabla \times \bar{\mathbf{P}}) \times \hat{n}) \cdot ((\nabla \times \mathbf{E}) \times \mathcal{V}) \rrbracket ds(\mathbf{r}) \right\}. \end{aligned}$$

Using the Green's identity and also continuity conditions in (3.45), we rewrite the second integral as follows

$$\int_{\partial\Omega_s} \llbracket (\gamma_t(\nabla \times \mathbf{E}) \times \hat{n}) \cdot \nabla(\mathcal{V} \cdot \bar{\mathbf{P}}) \rrbracket ds(\mathbf{r}) = - \int_{\partial\Omega_s} \llbracket \nabla_t \cdot (\gamma_t(\nabla \times \mathbf{E}) \times \hat{n}) \bar{\mathbf{P}} \cdot \hat{n} \rrbracket \mathcal{V} \cdot \hat{n} ds(\mathbf{r}).$$

The third integral can also be simplified similar to the second integral. Since the fourth and the fifth integrals are zero due to the continuity conditions in (3.45), we get the following form for $d\mathcal{J}$

$$\begin{aligned} d\mathcal{J} = \operatorname{Re} \left\{ \int_{\partial\Omega_s} \llbracket \nabla_t \cdot (\gamma_t(\nabla \times \mathbf{E}) \times \hat{n}) \bar{\mathbf{P}} \cdot \hat{n} \right. \\ \left. + \nabla_t \cdot (\gamma_t(\nabla \times \bar{\mathbf{P}}) \times \hat{n}) \mathbf{E} \cdot \hat{n} - k^2(\mathbf{r}) \mathbf{E} \cdot \bar{\mathbf{P}} \rrbracket \mathcal{V} \cdot \hat{n} ds(\mathbf{r}) \right\}. \end{aligned}$$

3.4 Approximation of shape gradients

In this section we investigate the approximation of the shape gradient $d\mathcal{J}$. As explained before, the shape gradient can be expressed in terms of volume and boundary integrals. For exact solutions of adjoint and state problems we have

$$d\mathcal{J} = d\mathcal{J}^{\text{Vol}} = d\mathcal{J}^{\text{Bdry}}, \quad (3.46)$$

where $d\mathcal{J}^{\text{Vol}}$ and $d\mathcal{J}^{\text{Bdry}}$ are expressions in terms of volume and boundary integrals, respectively. The operator $d\mathcal{J}$ can be approximated by replacing the finite element solutions of state and adjoint problems, which breaks down the equality in (3.46). So, the natural question is, which form of shape gradient expressions should be preferred for an approximation of $d\mathcal{J}$. To answer this question, we discuss the scalar and Maxwell problem separately.

3.4.1 Scalar Problem

Here we recall results obtained in [34] for the scalar problem discussed in Section 3.3.1. We introduce a family V_h of finite-dimensional subspaces of $H_0^1(\Omega)$ and define $u_h \in g + V_h$, $p_h \in V_h$ as Ritz-Galerkin solutions² of (3.4) and (3.6), respectively, that is,

$$\int_{\Omega} \nabla u_h \cdot \nabla v_h + u_h v_h \, d\mathbf{x} = \int_{\Omega} f v_h \, d\mathbf{x} \quad \forall v_h \in V_h, \quad (3.47)$$

$$\int_{\Omega} \nabla p_h \cdot \nabla v_h + p_h v_h \, d\mathbf{x} = \int_{\Omega} j(u_h) v_h \, d\mathbf{x} \quad \forall v_h \in V_h. \quad (3.48)$$

In particular, we let V_h be a family of H^1 piecewise linear Lagrangian finite element spaces built on simplicial meshes [11, Ch. II, Def. 5.1], and let h designate the meshwidth.

Assumption 5. *The Dirichlet BVP for the Laplacian is H^2 -regular [11, Ch. II, Def. 7.1], that is, if a function $w \in H_0^1(\Omega)$ is the (unique) weak*

²Note that p_h is not a proper Ritz-Galerkin solution to (3.6), because the right-hand side is perturbed.

solution to the elliptic BVP

$$\begin{cases} -\Delta w + w = \rho & \text{in } \Omega, \\ w = 0 & \text{on } \partial\Omega, \end{cases}$$

for a function $\rho \in L^2(\Omega)$, then $w \in H^2(\Omega)$.

Assumption 6. The source function f and the boundary data g in (3.4) are restrictions of functions in $H^1(\mathbb{R}^d)$ and $H^3(\mathbb{R}^d)$ to Ω and $\partial\Omega$, respectively.

Theorem 7. Let u and p be the solutions of state and adjoint problem (3.4) and (3.6), and let u_h and p_h be their Ritz-Galerkin approximations in the sense of (3.47) and (3.48) by piecewise linear Lagrangian finite elements. Furthermore, let Assumptions 5 and 6 be satisfied. Then³

$$|d\mathcal{J}(\Omega; \mathcal{V}) - d\mathcal{J}(\Omega, u_h, p_h; \mathcal{V})^{\text{Vol}}| \leq C(\Omega, u, p, f, g)h^2 \|\mathcal{V}\|_{W^{2,4}(\Omega)},$$

where the constant $C(\Omega, u, p, f, g)$ depends on the domain Ω and its discretization, $\|u\|_{H^2(\Omega)}$, $\|p\|_{H^2(\Omega)}$, $\|f\|_{H^1(\Omega)}$, and $\|g\|_{H^3(\Omega)}$.

Theorem 8. Let u_h and p_h be Ritz-Galerkin linear Lagrangian finite element approximations of the solutions u and p of (3.4) and (3.6), then

$$|d\mathcal{J}(\Omega; \mathcal{V}) - d\mathcal{J}(\Omega, u_h, p_h; \mathcal{V})^{\text{Bdry}}| \leq Ch \|\mathcal{V} \cdot \hat{n}\|_{L^\infty(\partial\Omega)},$$

where h stands for the meshwidth, and $C > 0$ does not depend on h .

Proof of Theorem 7 and 8 are given by detail in [34].

3.4.2 Maxwell problem

In theorem 9, we also show that $d\mathcal{J}(\Omega, \mathbf{E}_h, \mathbf{P}_h; \mathcal{V})^{\text{Vol}}$ enjoys superb convergence for the Maxwell problem. Before getting to the theorem, we need to take a closer look at the regularity of Maxwell's transmission problem within domains Ω_s and $\Omega_c = \Omega \setminus \bar{\Omega}_s$. According to [18], the study of the

³For the sake of readability, we use the same notation for scalar and vectorial Sobolev norms.

smoothness of solutions of

$$\begin{cases} \nabla \times \mu^{-1} \nabla \times \mathbf{u} - \omega^2 \epsilon \mathbf{u} = \mathbf{F} & \text{in } \Omega, \\ \mathbf{u} \times \hat{n} = 0 & \text{on } \partial\Omega, \end{cases} \quad (3.49)$$

for $\mathbf{F} \in L^2(\Omega)$ and $\nabla \cdot \mathbf{F} \in L^2(\Omega)$, can rely on smoothness results for 2nd-order scalar elliptic PDEs $\nabla \cdot (\epsilon \nabla v) = f$ and $\nabla \cdot (\mu^{-1} \nabla w) = g$ for $f, g \in L^2(\Omega)$. The Sobolev regularity of \mathbf{u} will be that of the sum of the gradients of v and w . This can be shown based on the decomposition of \mathbf{u} into a H^1 -regular vectorfield and a gradient, see [18, Sec. 3]. If both μ and ϵ are piecewise C^2 and jump only across a single interface, then standard elliptic regularity theory [47, Thm. 8.10] tells us that v and w will belong to H^2 both in Ω_s and Ω_c . Moreover, their corresponding H^2 -norms will be bounded by the L^2 -norms of the source functions f and g . In terms of \mathbf{u} this permits us to conclude that \mathbf{u} will be in $H^1(\Omega_s \cup \Omega_c)$, such that

$$\|\mathbf{u}\|_{H^1(\Omega_s \cup \Omega_c)} + \|\nabla \times \mathbf{u}\|_{H^1(\Omega_s \cup \Omega_c)} \leq C(\Omega)(\|\mathbf{F}\|_{L^2(\Omega)} + \|\nabla \cdot \mathbf{F}\|_{L^2(\Omega)}), \quad (3.50)$$

with a constant independent of \mathbf{F} .

Since we could not find a concise statement of such a result in literature that fits our setting, we make the assumption:

Assumption 7. *Let $k(\mathbf{r})$ be twice continuously differentiable (up to the boundary) both in Ω_s and Ω_c and the function $\mathbf{u} \in H^1(\Omega_s \cup \Omega_c)$ and $\nabla \times \mathbf{u} \in H^1(\Omega_s \cup \Omega_c)$ be the solution to the following problem*

$$\begin{cases} \nabla \times \nabla \times \mathbf{u} - k^2(\mathbf{r})\mathbf{u} = \mathbf{F} & \mathbf{r} \in \Omega, \\ \llbracket \gamma_t(\mathbf{u}) \rrbracket = 0 & \mathbf{r} \in \partial\Omega_s, \\ \llbracket \gamma_t(\nabla \times \mathbf{u}) \rrbracket = 0 & \mathbf{r} \in \partial\Omega_s, \\ \nabla \times \mathbf{u} \times \hat{n} = DtN[\mathbf{u}] & \mathbf{r} \in \partial\Omega, \end{cases} \quad (3.51)$$

for $\partial\Omega_s, \partial\Omega \in C^2$, $\mathbf{F} \in L^2(\Omega)$, and $\nabla \cdot \mathbf{F} \in L^2(\Omega)$, then we have

$$\|\mathbf{u}\|_{H^1(\Omega_s \cup \Omega_c)} + \|\nabla \times \mathbf{u}\|_{H^1(\Omega_s \cup \Omega_c)} \leq C(\Omega)(\|\mathbf{F}\|_{L^2(\Omega)} + \|\nabla \cdot \mathbf{F}\|_{L^2(\Omega)}). \quad (3.52)$$

Similar to the scalar case, we introduce $X_h \subset H(\text{curl}, \Omega)$ as the lowest order edge elements space defined on a shape regular and quasi-uniform

3 Shape Gradient: Evaluation and Approximation

family of meshes. We also define $\mathbf{E}_h, \mathbf{P}_h \in X_h$ as finite element solutions of (3.29) and (3.37), such that

$$\begin{aligned} & \int_{\Omega} \nabla \times \mathbf{E}_h \cdot \nabla \times \overline{\mathbf{W}}_h - k^2(\mathbf{r}) \mathbf{E}_h \cdot \overline{\mathbf{W}}_h \, d\mathbf{r} - \int_{\partial\Omega} \text{DtN}[\mathbf{E}_h] \cdot \overline{\mathbf{W}}_h \, ds(\mathbf{r}) \\ &= \int_{\partial\Omega} ((\nabla \times \mathbf{E}_i) \times \hat{n}) \cdot \overline{\mathbf{W}}_h - \text{DtN}[\mathbf{E}_i] \cdot \overline{\mathbf{W}}_h \, ds(\mathbf{r}) \quad \forall \mathbf{W}_h \in X_h, \end{aligned} \quad (3.53)$$

$$\begin{aligned} & \int_{\Omega} \nabla \times \overline{\mathbf{P}}_h \cdot \nabla \times \mathbf{W}_h - k^2(\mathbf{r}) \overline{\mathbf{P}}_h \cdot \mathbf{W}_h \, d\mathbf{r} - \int_{\partial\Omega} \overline{\text{DtN}^*[\mathbf{P}_h]} \cdot \mathbf{W}_h \, ds(\mathbf{r}) \\ &= \int_{\Omega} \mathbf{W}_h(\mathbf{r}) \cdot \mathcal{G}(\mathbf{E}_h, \mathbf{r}) \, d\mathbf{r} \quad \forall \mathbf{W}_h \in X_h. \end{aligned} \quad (3.54)$$

Assumption 8. *If $a : H(\text{curl}, \Omega) \times H(\text{curl}, \Omega) \mapsto \mathbb{C}$ is a sesquilinear form given as the following*

$$a(\mathbf{u}, \mathbf{v}) = \int_{\Omega} \nabla \times \mathbf{u} \cdot \nabla \times \overline{\mathbf{v}} - k^2(\mathbf{r}) \mathbf{u} \cdot \overline{\mathbf{v}} \, d\mathbf{r} - \int_{\partial\Omega} \text{DtN}[\mathbf{u}] \cdot \overline{\mathbf{v}} \, ds(\mathbf{r}).$$

then for sufficiently small mesh width h , we assume⁴

$$C \|\mathbf{u}_h\| \leq \sup_{\mathbf{v}_h \in X_h} \frac{|a(\mathbf{u}_h, \mathbf{v}_h)|}{\|\mathbf{v}_h\|_{H(\text{curl}, \Omega)}} \quad \forall \mathbf{u}_h \in X_h, \quad (3.55)$$

where C is independent of h (it only depends on Ω and the shape regularity).

We also recall that for any tetrahedral mesh Ω_h with meshwidth $h > 0$ we have the following a priori interpolation error estimate [32, Thm. 3.14]

$$\|\nabla \times \mathbf{u} - \nabla \times \mathcal{I}_h \mathbf{u}\|_{L^2(\Omega)} \leq C h \|\nabla \times \mathbf{u}\|_{H^1(\Omega_s \cup \Omega_c)},$$

⁴The discrete inf-sup condition is proven in [32, Thm. 5.2] for the Maxwell's problem with $\mathbf{u} \times \hat{n} = 0$ on the outer boundary. Here, we believe that the same result can be obtained for the case with the DtN map on $\partial\Omega$, by following the same lines as in [32, Sec. 5.2].

(3.56)

$$\|\mathbf{u} - \mathcal{I}_h \mathbf{u}\|_{L^2(\Omega)} \leq C h (\|\mathbf{u}\|_{H^1(\Omega_s \cup \Omega_c)} + \|\nabla \times \mathbf{u}\|_{H^1(\Omega_s \cup \Omega_c)}),$$

where $\mathcal{I}_h \mathbf{u}$ is the lowest order edge interpolation of \mathbf{u} .

We can extend (3.56) using standard finite element convergence estimate [32, Ch. 5]

$$\|\mathbf{u} - \mathbf{u}_h\|_{H(\text{curl}, \Omega)} \leq C h (\|\mathbf{u}\|_{H^1(\Omega_s \cup \Omega_c)} + \|\nabla \times \mathbf{u}\|_{H^1(\Omega_s \cup \Omega_c)}). \quad (3.57)$$

Remark 9. Note that, the error measured with respect to the $L^2(\Omega)$ norm does not decrease as h^2 when the solution is approximated employing edge elements [32, Ch. 5]

$$\|\mathbf{u} - \mathbf{u}_h\|_{L^2(\Omega)} \leq C h (\|\mathbf{u}\|_{H^1(\Omega_s \cup \Omega_c)} + \|\nabla \times \mathbf{u}\|_{H^1(\Omega_s \cup \Omega_c)})$$

Theorem 9. Let \mathbf{E} and \mathbf{P} be solutions of (3.29) and (3.37), and let \mathbf{E}_h and \mathbf{P}_h be their lowest order edge element approximation as (3.53) and (3.54). Furthermore, let assumption 7 be satisfied. Then, similar to the scalar case, the volume formulation of the shape gradient converges to the exact expression with the rate h^2

$$|d\mathcal{J}(\Omega; \mathcal{V}) - d\mathcal{J}(\Omega, \mathbf{E}_h, \mathbf{P}_h; \mathcal{V})^{\text{Vol}}| \leq C(\Omega, \mathbf{E}, \mathbf{P}) h^2 \|\mathcal{V}\|_{W^{2, \infty}(\Omega)},$$

Proof. From the equality $d\mathcal{J}(\Omega; \mathcal{V}) = d\mathcal{J}(\Omega, \mathbf{E}, \mathbf{P}; \mathcal{V})^{\text{Vol}}$ and using the triangle inequality, we immediately get

$$\begin{aligned} & |d\mathcal{J}(\Omega; \mathcal{V}) - d\mathcal{J}(\Omega, \mathbf{E}_h, \mathbf{P}_h; \mathcal{V})^{\text{Vol}}| \\ & \leq \left(\left| \text{Re} \int_{\Omega} \nabla \times \mathbf{E} \cdot (D\mathcal{V} + D\mathcal{V}^T) \nabla \times \bar{\mathbf{P}} \right. \right. \\ & \quad \left. \left. - \nabla \times \mathbf{E}_h \cdot (D\mathcal{V} + D\mathcal{V}^T) \nabla \times \bar{\mathbf{P}}_h \, d\mathbf{r} \right| \right. \\ & \quad \left. + \left| \text{Re} \int_{\Omega} k^2 \mathbf{E} \cdot (D\mathcal{V} + D\mathcal{V}^T) \bar{\mathbf{P}} - k^2 \mathbf{E}_h \cdot (D\mathcal{V} + D\mathcal{V}^T) \bar{\mathbf{P}}_h \, d\mathbf{r} \right| \right. \\ & \quad \left. + \left| \text{Re} \int_{\Omega} \nabla \cdot \mathcal{V} \cdot (\nabla \times \mathbf{E} \cdot \nabla \times \bar{\mathbf{P}} + k^2 \mathbf{E} \cdot \bar{\mathbf{P}} \right. \right. \end{aligned}$$

$$- \nabla \times \mathbf{E}_h \cdot \nabla \times \bar{\mathbf{P}}_h - k^2 \mathbf{E}_h \cdot \bar{\mathbf{P}}_h) \, d\mathbf{r} \Big),$$

which results in

$$\begin{aligned} & |d\mathcal{J}(\Omega; \mathcal{V}) - d\mathcal{J}(\Omega, \mathbf{E}_h, \mathbf{P}_h; \mathcal{V})^{\text{Vol}}| \tag{3.58} \\ & \leq \left(\left| \int_{\Omega} \nabla \times \mathbf{E} \cdot (D\mathcal{V} + D\mathcal{V}^T) \nabla \times \bar{\mathbf{P}} \right. \right. \\ & \quad \left. \left. - \nabla \times \mathbf{E}_h \cdot (D\mathcal{V} + D\mathcal{V}^T) \nabla \times \bar{\mathbf{P}}_h \, d\mathbf{r} \right| \right. \\ & \quad + \left| \int_{\Omega} k^2 \mathbf{E} \cdot (D\mathcal{V} + D\mathcal{V}^T) \bar{\mathbf{P}} \right. \\ & \quad \left. - k^2 \mathbf{E}_h \cdot (D\mathcal{V} + D\mathcal{V}^T) \bar{\mathbf{P}}_h \, d\mathbf{r} \right| \\ & \quad + \left| \int_{\Omega} \nabla \cdot \mathcal{V} \cdot (\nabla \times \mathbf{E} \cdot \nabla \times \bar{\mathbf{P}} + k^2 \mathbf{E} \cdot \bar{\mathbf{P}} \right. \\ & \quad \left. - \nabla \times \mathbf{E}_h \nabla \times \bar{\mathbf{P}}_h - k^2 \mathbf{E}_h \cdot \bar{\mathbf{P}}_h) \, d\mathbf{r} \right| \Big). \end{aligned}$$

The proof boils down to bounding each integral in (3.58) by applying standard finite element convergence estimate (3.56) and (3.57) and using duality techniques.

To begin with, we split the first integral into

$$\begin{aligned} & \int_{\Omega} \nabla \times \mathbf{E} \cdot (D\mathcal{V} + D\mathcal{V}^T) \nabla \times \bar{\mathbf{P}} - \nabla \times \mathbf{E}_h \cdot (D\mathcal{V} + D\mathcal{V}^T) \nabla \times \bar{\mathbf{P}}_h \, d\mathbf{r} \tag{3.59} \\ & = \int_{\Omega} \nabla \times (\mathbf{E} - \mathbf{E}_h) \cdot (D\mathcal{V} + D\mathcal{V}^T) \nabla \times \bar{\mathbf{P}} \, d\mathbf{r} \\ & \quad + \int_{\Omega} \nabla \times \mathbf{E} \cdot (D\mathcal{V} + D\mathcal{V}^T) \nabla \times (\bar{\mathbf{P}} - \bar{\mathbf{P}}_h) \, d\mathbf{r} \\ & \quad + \int_{\Omega} \nabla \times (\mathbf{E} - \mathbf{E}_h) \cdot (D\mathcal{V} + D\mathcal{V}^T) \nabla \times (\bar{\mathbf{P}} - \bar{\mathbf{P}}_h) \, d\mathbf{r}. \end{aligned}$$

To bound the first and the second integral on the right hand side of the (3.59), we use duality techniques. For the first one we introduce the function

\mathbf{u} as the weak solution to the following BVP

$$\begin{cases} \nabla \times \nabla \times \bar{\mathbf{u}} - k^2(\mathbf{r})\bar{\mathbf{u}} = \nabla \times ((D\mathcal{V} + D\mathcal{V}^T)\nabla \times \mathbf{P}) & \mathbf{r} \in \Omega, \\ \llbracket \gamma_t(\bar{\mathbf{u}}) \rrbracket = 0 & \mathbf{r} \in \partial\Omega_s, \\ \llbracket \gamma_t(\nabla \times \bar{\mathbf{u}}) \rrbracket = 0 & \mathbf{r} \in \partial\Omega_s, \\ \nabla \times \bar{\mathbf{u}} \times \hat{\mathbf{n}}, = \overline{\text{DtN}^*[\mathbf{u}]} & \mathbf{r} \in \partial\Omega, \end{cases} \quad (3.60)$$

that is

$$\begin{aligned} & \int_{\Omega} \nabla \times \mathbf{u} \cdot \nabla \times \mathbf{v} - k^2 \mathbf{u} \cdot \mathbf{v} \, d\mathbf{r} - \int_{\partial\Omega} \text{DtN}^*[\mathbf{u}] \cdot \mathbf{v} \, ds \\ & = \int_{\Omega} \nabla \times \mathbf{v} \cdot (D\mathcal{V} + D\mathcal{V}^T)\nabla \times \bar{\mathbf{P}} \quad \forall \mathbf{v} \in H_0(\text{curl}, \Omega). \end{aligned} \quad (3.61)$$

Using (3.52) and keeping in mind that the right hand side of (3.60) is divergence free, we get

$$\|\mathbf{u}\|_{H^1(\Omega_s \cup \Omega_c)} + \|\nabla \times \mathbf{u}\|_{H^1(\Omega_s \cup \Omega_c)} \leq C (\|\nabla \times ((D\mathcal{V} + D\mathcal{V}^T)\nabla \times \mathbf{P})\|_{L^2(\Omega)}) . \quad (3.62)$$

By triangular inequality and product rule, we have

$$\begin{aligned} & \|\nabla \times ((D\mathcal{V} + D\mathcal{V}^T)\nabla \times \mathbf{P})\|_{L^2(\Omega)} \\ & \leq C (\|\nabla \times \mathcal{V}\|_{W^{1,\infty}} \|\nabla \times \mathbf{P}\|_{L^2(\Omega)} + \|\mathcal{V}\|_{W^{1,\infty}} \|\nabla \times \mathbf{P}\|_{H^1(\Omega_s \cup \Omega_c)}) \\ & \leq C \|\nabla \times \mathcal{V}\|_{W^{1,\infty}} \|\nabla \times \mathbf{P}\|_{H^1(\Omega_s \cup \Omega_c)}. \end{aligned} \quad (3.63)$$

Using (3.61) and exploiting the Galerkin orthogonality of $\mathbf{E} - \mathbf{E}_h$ to the finite dimensional trial space X_h , we have

$$\begin{aligned} & \int_{\Omega} \nabla \times (\mathbf{E} - \mathbf{E}_h) \cdot (D\mathcal{V} + D\mathcal{V}^T)\nabla \times \bar{\mathbf{P}} \, d\mathbf{r} = a(\mathbf{E} - \mathbf{E}_h, \bar{\mathbf{u}}) \\ & = a(\mathbf{E} - \mathbf{E}_h, \bar{\mathbf{u}} - \mathcal{I}_h \bar{\mathbf{u}}). \end{aligned}$$

Since $a(\cdot, \cdot)$ is continuous in $L^2(\Omega)$, we have

$$\left| \int_{\Omega} \nabla \times (\mathbf{E} - \mathbf{E}_h) \cdot (D\mathcal{V} + D\mathcal{V}^T)\nabla \times \bar{\mathbf{P}} \, d\mathbf{r} \right|$$

3 Shape Gradient: Evaluation and Approximation

$$\leq C \|\mathbf{E} - \mathbf{E}_h\|_{H(\text{curl}, \Omega)} \|\mathbf{u} - \mathcal{I}_h \mathbf{u}\|_{H(\text{curl}, \Omega)}.$$

Using (3.56) and (3.57), we conclude

$$\begin{aligned} & \left| \int_{\Omega} \nabla \times (\mathbf{E} - \mathbf{E}_h) \cdot (D\mathcal{V} + D\mathcal{V}^T) \nabla \times \bar{\mathbf{P}} \, d\mathbf{r} \right| \\ & \leq Ch^2 (\|\mathbf{E}\|_{H^1(\Omega_s \cup \Omega_c)} + \|\nabla \times \mathbf{E}\|_{H^1(\Omega_s \cup \Omega_c)}) \|\nabla \times \mathcal{V}\|_{W^{1, \infty}} \|\nabla \times \bar{\mathbf{P}}\|_{H^1(\Omega_s \cup \Omega_c)}. \end{aligned}$$

Similarly, for the second integral on the right hand side of (3.59) we introduce the function \mathbf{u} as the weak solution to the following problem

$$\begin{cases} \nabla \times \nabla \times \mathbf{u} - k^2(\mathbf{r})\mathbf{u}, = \nabla \times ((D\mathcal{V} + D\mathcal{V}^T) \nabla \times \mathbf{E}) & \mathbf{r} \in \Omega, \\ \llbracket \gamma_t(\mathbf{u}) \rrbracket = 0 & \mathbf{r} \in \partial\Omega_s, \\ \llbracket \gamma_t(\nabla \times \mathbf{u}) \rrbracket = 0 & \mathbf{r} \in \partial\Omega_s, \\ \nabla \times \mathbf{u} \times \hat{n} = \text{DtN}[\mathbf{u}] & \mathbf{r} \in \partial\Omega, \end{cases}$$

that is

$$\begin{aligned} & \int_{\Omega} \nabla \times \mathbf{u} \cdot \nabla \times \bar{\mathbf{v}} - k^2 \mathbf{u} \cdot \bar{\mathbf{v}} \, d\mathbf{r} - \int_{\partial\Omega} \text{DtN}[\mathbf{u}] \cdot \bar{\mathbf{v}} \, ds \\ & = \int_{\Omega} \nabla \times \bar{\mathbf{v}} \cdot (D\mathcal{V} + D\mathcal{V}^T) \nabla \times \mathbf{E} \, d\mathbf{r} \quad \forall \bar{\mathbf{v}} \in H_0(\text{curl}, \Omega). \end{aligned}$$

Similar to (3.63), we derive the following bound for function \mathbf{u}

$$\|\mathbf{u}\|_{H^1(\Omega_s \cup \Omega_c)} + \|\nabla \times \mathbf{u}\|_{H^1(\Omega_s \cup \Omega_c)} \leq C \|\nabla \times \mathcal{V}\|_{W^{1, \infty}} \|\nabla \times \mathbf{E}\|_{H^1(\Omega_s \cup \Omega_c)}. \quad (3.64)$$

Next, we note that for every $\mathbf{v}_h \in X_h$ we have

$$\begin{aligned} & \int_{\Omega} \nabla \times (\bar{\mathbf{P}} - \bar{\mathbf{P}}_h) \cdot \nabla \times \mathbf{v}_h - k^2 (\bar{\mathbf{P}} - \bar{\mathbf{P}}_h) \mathbf{v}_h \, d\mathbf{r} - \int_{\partial\Omega} \overline{\text{DtN}^*[\bar{\mathbf{P}} - \bar{\mathbf{P}}_h]} \cdot \mathbf{v}_h \, ds \\ & = \int_{\Omega} (\mathcal{G}(\mathbf{E}) - \mathcal{G}(\mathbf{E}_h)) \cdot \mathbf{v}_h \, d\mathbf{r} \end{aligned}$$

which implies

$$\left| \int_{\Omega} \nabla \times (\bar{\mathbf{P}} - \bar{\mathbf{P}}_h) \cdot (D\mathcal{V} + D\mathcal{V}^T) \nabla \times \mathbf{E} \, d\mathbf{r} \right| = |a^*(\bar{\mathbf{P}} - \bar{\mathbf{P}}_h, \mathbf{u})|$$

$$\leq |a^*(\mathbf{P} - \mathbf{P}_h, \mathbf{u} - \mathcal{I}_h \mathbf{u})| + \left| \int_{\Omega} (\mathcal{G}(\mathbf{E}) - \mathcal{G}(\mathbf{E}_h)) \cdot \mathcal{I}_h \mathbf{u} \, d\mathbf{r} \right|,$$

where $a^*(\mathbf{u}, \mathbf{v}) := a(\mathbf{v}, \mathbf{u})$. Then, using continuity of $a^*(\cdot, \cdot)$ in $L^2(\Omega)$,

$$\begin{aligned} & \left| \int_{\Omega} \nabla \times (\bar{\mathbf{P}} - \bar{\mathbf{P}}_h) \cdot (D\mathcal{V} + D\mathcal{V}^T) \nabla \times \mathbf{E} \, d\mathbf{r} \right| \\ & \leq C \|\mathbf{P} - \mathbf{P}_h\|_{H(\text{curl}, \Omega)} \|\mathbf{u} - \mathcal{I}_h \mathbf{u}\|_{H(\text{curl}, \Omega)} + \left| \int_{\Omega} \mathcal{G}(\mathbf{E} - \mathbf{E}_h) \cdot \mathcal{I}_h \mathbf{u} \, d\mathbf{r} \right|. \end{aligned} \quad (3.65)$$

Unlike the scalar problem in [34], we cannot use the continuity of $\mathcal{G}(\mathbf{E} - \mathbf{E}_h)$ in $L^2(\Omega)$ norm to bound the second term on the right hand side of (3.65). As depicted in Remark 9, the error in $L^2(\Omega)$ norm decreases as h . So, we use duality technique once more to achieve higher convergence rates.

Based on (3.33), we have

$$\int_{\Omega} \mathcal{G}(\mathbf{E} - \mathbf{E}_h) \cdot \mathcal{I}_h \mathbf{u} \, d\mathbf{r} = \int_{\Omega} (\mathbf{E}(\mathbf{r}) - \mathbf{E}_h(\mathbf{r})) \cdot \mathcal{K}(\mathbf{r}) \, d\mathbf{r}, \quad (3.66)$$

where

$$\mathcal{K}(\mathbf{r}) = \int_{\Omega_{\text{leaves}}} \kappa_f(\mathbf{r}, \hat{\mathbf{r}}_1) \int_{\Omega} \mathcal{I}_h \mathbf{u}(\mathbf{r}_2) \cdot \kappa_f(\mathbf{r}_2, \hat{\mathbf{r}}_1) \, d\mathbf{r}_2 \, d\hat{\mathbf{r}}_1. \quad (3.67)$$

To bound (3.66), we again use the duality technique and define \mathbf{q} as the weak solution to the following BVPs

$$\begin{cases} \nabla \times \nabla \times \bar{\mathbf{q}} - k^2(\mathbf{r})\bar{\mathbf{q}} = \overline{\mathcal{K}} & \mathbf{r} \in \Omega, \\ \llbracket \gamma_t(\bar{\mathbf{q}}) \rrbracket = 0 & \mathbf{r} \in \partial\Omega_s, \\ \llbracket \gamma_t(\nabla \times \bar{\mathbf{q}}) \rrbracket = 0 & \mathbf{r} \in \partial\Omega_s, \\ \nabla \times \bar{\mathbf{q}} \times \hat{n} = \overline{\text{DtN}^*[\mathbf{q}]} & \mathbf{r} \in \partial\Omega, \end{cases} \quad (3.68)$$

that is

$$\begin{aligned} & \int_{\Omega} \nabla \times \mathbf{q} \cdot \nabla \times \mathbf{v} - k^2 \mathbf{q} \cdot \mathbf{v} \, d\mathbf{r} - \int_{\partial\Omega} \text{DtN}^*[\mathbf{q}] \cdot \mathbf{v} \, ds \\ & = \int_{\Omega} \mathbf{v} \cdot \mathcal{K}(\mathbf{r}) \, d\mathbf{r} \quad \forall \mathbf{v} \in H_0(\text{curl}, \Omega). \end{aligned} \quad (3.69)$$

3 Shape Gradient: Evaluation and Approximation

Since $\kappa(\mathbf{r})$ is a smooth function in \mathbf{r} , we use Assumption 7 and write

$$\|\mathbf{q}\|_{H^1(\Omega_s \cup \Omega_c)} + \|\nabla \times \mathbf{q}\|_{H^1(\Omega_s \cup \Omega_c)} \leq C (\|\mathcal{K}\|_{L^2(\Omega)} + \|\nabla \cdot \mathcal{K}\|_{L^2(\Omega)}). \quad (3.70)$$

Using Cauchy-Schwarz inequality, we can show that

$$\begin{aligned} & \|\mathcal{K}\|_{L^2(\Omega)} + \|\nabla \cdot \mathcal{K}\|_{L^2(\Omega)} \\ & \leq C \|\mathcal{I}_h \mathbf{u}\|_{H(\text{curl}, \Omega)} \|\kappa_f(\mathbf{r}, \hat{\mathbf{r}}_1)\|_{W^{1,\infty}(\Omega \times \Omega_{\text{tens}})} \|\nabla^{\mathbf{r}} \kappa_f(\mathbf{r}, \hat{\mathbf{r}}_1)\|_{W^{1,\infty}(\Omega \times \Omega_{\text{tens}})}. \end{aligned} \quad (3.71)$$

Then, using (3.64) to bound $\|\mathcal{I}_h \mathbf{u}\|_{H(\text{curl}, \Omega)}$,

$$\begin{aligned} & \|\mathcal{K}\|_{L^2(\Omega)} + \|\nabla \cdot \mathcal{K}\|_{L^2(\Omega)} \\ & \leq C \|\nabla \times \mathcal{V}\|_{W^{1,\infty}} \|\nabla \times \mathbf{E}\|_{H^1(\Omega_s \cup \Omega_c)} \\ & \quad \|\kappa_f(\mathbf{r}, \hat{\mathbf{r}}_1)\|_{W^{1,\infty}(\Omega \times \Omega_{\text{tens}})} \|\nabla^{\mathbf{r}} \kappa_f(\mathbf{r}, \hat{\mathbf{r}}_1)\|_{W^{1,\infty}(\Omega \times \Omega_{\text{tens}})}. \end{aligned} \quad (3.72)$$

Using Galerkin orthogonality, continuity of $a(\cdot, \cdot)$, and (3.69), we have

$$\begin{aligned} \left| \int_{\Omega} (\mathbf{E}(\mathbf{r}) - \mathbf{E}_h(\mathbf{r})) \cdot \mathcal{K}(\mathbf{r}) \, d\mathbf{r} \right| &= |a(\mathbf{E} - \mathbf{E}_h, \bar{\mathbf{q}})| \\ &= |a(\mathbf{E} - \mathbf{E}_h, \bar{\mathbf{q}} - \mathcal{I}_h \bar{\mathbf{q}})| \\ &\leq C \|\mathbf{E} - \mathbf{E}_h\|_{H(\text{curl}, \Omega)} \|\mathbf{q} - \mathcal{I}_h \mathbf{q}\|_{H(\text{curl}, \Omega)}. \end{aligned}$$

So, based on (3.72), (3.56), and (3.57),

$$\begin{aligned} & \left| \int_{\Omega} (\mathbf{E}(\mathbf{r}) - \mathbf{E}_h(\mathbf{r})) \cdot \mathcal{K}(\mathbf{r}) \, d\mathbf{r} \right| \\ & \leq C h^2 \|\nabla \times \mathcal{V}\|_{W^{1,\infty}} \|\nabla \times \mathbf{E}\|_{H^1(\Omega_s \cup \Omega_c)} \|\kappa_f(\mathbf{r}, \hat{\mathbf{r}}_1)\|_{W^{1,\infty}(\Omega \times \Omega_{\text{tens}})} \\ & \quad \|\nabla^{\mathbf{r}} \kappa_f(\mathbf{r}, \hat{\mathbf{r}}_1)\|_{W^{1,\infty}(\Omega \times \Omega_{\text{tens}})} (\|\mathbf{E}\|_{H^1(\Omega_s \cup \Omega_o)} + \|\nabla \times \mathbf{E}\|_{H^1(\Omega_s \cup \Omega_o)}). \end{aligned} \quad (3.73)$$

In order to establish a bound for $\|\mathbf{P} - \mathbf{P}_h\|_{H(\text{curl}, \Omega)}$ in (3.65), we follow the argument in the proof of Strang's first Lemma. We use inf-sup condition in Assumption 8, and get

$$C \|\mathbf{P}_h - \mathbf{w}_h\|_{H(\text{curl}, \Omega)} \leq \sup_{\mathbf{v}_h \in X_h} \frac{a^*(\mathbf{P}_h - \mathbf{w}_h, \mathbf{v}_h)}{\|\mathbf{v}_h\|_{H(\text{curl}, \Omega)}} \quad (3.74)$$

$$\begin{aligned}
 &\leq \sup_{\mathbf{v}_h \in \mathcal{X}_h} \frac{a^*(\mathbf{P}_h - \mathbf{P}, \mathbf{v}_h)}{\|\mathbf{v}_h\|_{H(\text{curl}, \Omega)}} + \sup_{\mathbf{v}_h \in \mathcal{X}_h} \frac{a^*(\mathbf{P} - \mathbf{w}_h, \mathbf{v}_h)}{\|\mathbf{v}_h\|_{H(\text{curl}, \Omega)}} \\
 &\leq \sup_{\mathbf{v}_h \in \mathcal{X}_h} \frac{\int_{\Omega} \mathcal{G}(\mathbf{E}_h - \mathbf{E}) \cdot \mathbf{v}_h}{\|\mathbf{v}_h\|_{H(\text{curl}, \Omega)}} + C \|\mathbf{P} - \mathbf{w}_h\|_{H(\text{curl}, \Omega)}.
 \end{aligned}$$

Since \mathcal{G} is continuous in $L^2(\Omega)$ norm, we have

$$\int_{\Omega} \mathcal{G}(\mathbf{E}_h - \mathbf{E}) \cdot \mathbf{v}_h \leq C \|\mathbf{E} - \mathbf{E}_h\|_{L^2(\Omega)} \|\mathbf{v}_h\|_{H(\text{curl}, \Omega)}. \quad (3.75)$$

Then, using (3.74), (3.75), (3.56), and (3.57),

$$\begin{aligned}
 \|\mathbf{P} - \mathbf{P}_h\|_{H(\text{curl}, \Omega)} &\leq \|\mathbf{P} - \mathcal{I}_h \mathbf{P}\|_{H(\text{curl}, \Omega)} + \|\mathcal{I}_h \mathbf{P} - \mathbf{P}_h\|_{H(\text{curl}, \Omega)} \quad (3.76) \\
 &\leq C \|\mathbf{P} - \mathcal{I}_h \mathbf{P}\|_{H(\text{curl}, \Omega)} + C \|\mathbf{E} - \mathbf{E}_h\|_{L^2(\Omega)} \\
 &\leq C h (\|\mathbf{P}\|_{H^1(\Omega_s \cup \Omega_o)} + \|\nabla \times \mathbf{P}\|_{H^1(\Omega_s \cup \Omega_o)} \\
 &\quad + \|\mathbf{E}\|_{H^1(\Omega_s \cup \Omega_o)} + \|\nabla \times \mathbf{E}\|_{H^1(\Omega_s \cup \Omega_o)}).
 \end{aligned}$$

Consequently, we can bound (3.65) as follows

$$\begin{aligned}
 &|\int_{\Omega} \nabla \times \mathbf{E} \cdot (D\mathcal{V} + D\mathcal{V}^T) \nabla \times (\bar{\mathbf{P}} - \bar{\mathbf{P}}_h) \, d\mathbf{r}| \quad (3.77) \\
 &\leq C h^2 \|\nabla \times \mathcal{V}\|_{W^{1, \infty}} \|\nabla \times \mathbf{E}\|_{H^1(\Omega_s \cup \Omega_o)} \\
 &\left\{ \|\bar{\mathbf{P}}\|_{H^1(\Omega_s \cup \Omega_o)} + \|\nabla \times \bar{\mathbf{P}}\|_{H^1(\Omega_s \cup \Omega_o)} + \left(\|\mathbf{E}\|_{H^1(\Omega_s \cup \Omega_o)} + \|\nabla \times \mathbf{E}\|_{H^1(\Omega_s \cup \Omega_o)} \right) \right. \\
 &\quad \left. \left(1 + \|\kappa_f(\mathbf{r}, \hat{\mathbf{r}}_1)\|_{W^{1, \infty}(\Omega \times \Omega_{\text{tens}})} \|\nabla^T \kappa_f(\mathbf{r}, \hat{\mathbf{r}}_1)\|_{W^{1, \infty}(\Omega \times \Omega_{\text{tens}})} \right) \right\}.
 \end{aligned}$$

Finally, we bound the third integral on the right hand side of (3.59) by employing Cauchy-Schwarz inequality, (3.76), (3.56), and (3.57)

$$\begin{aligned}
 &\int_{\Omega} \nabla \times (\mathbf{E} - \mathbf{E}_h) \cdot (D\mathcal{V} + D\mathcal{V}^T) \nabla \times (\bar{\mathbf{P}} - \bar{\mathbf{P}}_h) \, d\mathbf{r} \quad (3.78) \\
 &\leq \|\mathcal{V}\|_{W^{1, \infty} \Omega} \|\mathbf{E} - \mathbf{E}_h\|_{H(\text{curl}, \Omega)} \|\bar{\mathbf{P}} - \bar{\mathbf{P}}_h\|_{H(\text{curl}, \Omega)} \\
 &\leq C h^2 \|\mathcal{V}\|_{W^{1, \infty}} (\|\mathbf{E}\|_{H^1(\Omega_s \cup \Omega_o)} + \|\nabla \times \mathbf{E}\|_{H^1(\Omega_s \cup \Omega_o)}) \\
 &\quad (\|\bar{\mathbf{P}}\|_{H^1(\Omega_s \cup \Omega_o)} + \|\nabla \times \bar{\mathbf{P}}\|_{H^1(\Omega_s \cup \Omega_o)}) \\
 &\quad + \|\mathbf{E}\|_{H^1(\Omega_s \cup \Omega_o)} + \|\nabla \times \mathbf{E}\|_{H^1(\Omega_s \cup \Omega_o)}.
 \end{aligned}$$

3 Shape Gradient: Evaluation and Approximation

Along the same lines as before, we split the second integral on the right hand side of (3.58) as follows

$$\begin{aligned}
 \int_{\Omega} \mathbf{E} \cdot (D\mathcal{V} + D\mathcal{V}^T) \bar{\mathbf{P}} - \mathbf{E}_h \cdot (D\mathcal{V} + D\mathcal{V}^T) \mathbf{P}_h \, dr & \quad (3.79) \\
 &= \int_{\Omega} (\mathbf{E} - \mathbf{E}_h) \cdot (D\mathcal{V} + D\mathcal{V}^T) \bar{\mathbf{P}} \, dr \\
 &\quad + \int_{\Omega} \mathbf{E} \cdot (D\mathcal{V} + D\mathcal{V}^T) (\bar{\mathbf{P}} - \bar{\mathbf{P}}_h) \, dr \\
 &\quad + \int_{\Omega} (\mathbf{E} - \mathbf{E}_h) \cdot (D\mathcal{V} + D\mathcal{V}^T) (\bar{\mathbf{P}} - \bar{\mathbf{P}}_h) \, dr.
 \end{aligned}$$

To bound the first integral, we use duality technique and introduce \mathbf{u} as the weak solution to the following BVP

$$\begin{cases}
 \nabla \times \nabla \times \bar{\mathbf{u}} - k^2(\mathbf{r}) \bar{\mathbf{u}} = (D\mathcal{V} + D\mathcal{V}^T) \mathbf{P} & \mathbf{r} \in \Omega, \\
 \llbracket \gamma_t(\bar{\mathbf{u}}) \rrbracket = 0 & \mathbf{r} \in \partial\Omega_s, \\
 \llbracket \gamma_t(\nabla \times \bar{\mathbf{u}}) \rrbracket = 0 & \mathbf{r} \in \partial\Omega_s, \\
 \nabla \times \bar{\mathbf{u}} \times \hat{n}_s = \overline{\text{DtN}^*[\mathbf{u}]} & \mathbf{r} \in \partial\Omega,
 \end{cases} \quad (3.80)$$

that is

$$\begin{aligned}
 \int_{\Omega} \nabla \times \mathbf{u} \cdot \nabla \times \mathbf{v} - k^2 \mathbf{u} \cdot \mathbf{v} \, dr - \int_{\partial\Omega} \text{DtN}^*[\mathbf{u}] \cdot \mathbf{v} \, ds & \quad (3.81) \\
 = \int_{\Omega} \mathbf{v} \cdot (D\mathcal{V} + D\mathcal{V}^T) \bar{\mathbf{P}} \, dr \quad \forall \mathbf{v} \in H_0(\text{curl}, \Omega).
 \end{aligned}$$

Using Assumption 7, we have

$$\begin{aligned}
 & \|\mathbf{u}\|_{H^1(\Omega_s \cup \Omega_c)} + \|\nabla \times \mathbf{u}\|_{H^1(\Omega_s \cup \Omega_c)} & (3.82) \\
 & \leq C \left(\|(D\mathcal{V} + D\mathcal{V}^T) \bar{\mathbf{P}}\|_{L^2(\Omega)} + \|\nabla \cdot ((D\mathcal{V} + D\mathcal{V}^T) \bar{\mathbf{P}})\|_{L^2(\Omega)} \right) \\
 & \leq C (\|\mathcal{V}\|_{W^{1,\infty}(\Omega)} \|\bar{\mathbf{P}}\|_{L^2(\Omega)} + \|\mathcal{V}\|_{W^{2,\infty}(\Omega)} \|\bar{\mathbf{P}}\|_{L^2(\Omega)} + \|\mathcal{V}\|_{W^{1,\infty}(\Omega)} \|\bar{\mathbf{P}}\|_{H^1(\Omega_s \cup \Omega_c)}) \\
 & \leq C \|\mathcal{V}\|_{W^{2,\infty}(\Omega)} \|\bar{\mathbf{P}}\|_{H^1(\Omega_s \cup \Omega_c)}.
 \end{aligned}$$

Using Galerkin orthogonality, continuity of $a(\cdot, \cdot)$ and (3.81),

$$\begin{aligned}
 \left| \int_{\Omega} (\mathbf{E} - \mathbf{E}_h) \cdot (D\mathcal{V} + D\mathcal{V}^T) \bar{\mathbf{P}} \, d\mathbf{r} \right| &= |a(\mathbf{E} - \mathbf{E}_h, \bar{\mathbf{u}})| & (3.83) \\
 &= |a(\mathbf{E} - \mathbf{E}_h, \bar{\mathbf{u}} - \mathcal{I}_h \bar{\mathbf{u}})| \\
 &\leq C \|\mathbf{E} - \mathbf{E}_h\|_{H(\text{curl}, \Omega)} \|\mathbf{u} - \mathcal{I}_h \mathbf{u}\|_{H(\text{curl}, \Omega)}.
 \end{aligned}$$

Then, using (3.56), (3.57), (3.82), and Assumption 7

$$\begin{aligned}
 \left| \int_{\Omega} (\mathbf{E} - \mathbf{E}_h) \cdot (D\mathcal{V} + D\mathcal{V}^T) \bar{\mathbf{P}} \, d\mathbf{r} \right| & & (3.84) \\
 \leq C h^2 (\|\mathbf{E}\|_{H^1(\Omega_s \cup \Omega_o)} + \|\nabla \times \mathbf{E}\|_{H^1(\Omega_s \cup \Omega_o)}) \|\mathcal{V}\|_{W^{2,\infty}(\Omega)} \|\mathbf{P}\|_{H^1(\Omega_s \cup \Omega_c)}.
 \end{aligned}$$

To bound the second integral on the right hand side of (3.79), we again use the duality technique

$$\begin{cases} \nabla \times \nabla \times \mathbf{u} - k^2(\mathbf{r})\mathbf{u} = (D\mathcal{V} + D\mathcal{V}^T) \mathbf{E} & \mathbf{r} \in \Omega, \\ \llbracket \gamma_t(\mathbf{u}) \rrbracket = 0 & \mathbf{r} \in \partial\Omega_s, \\ \llbracket \gamma_t(\nabla \times \mathbf{u}) \rrbracket = 0 & \mathbf{r} \in \partial\Omega_s, \\ (\nabla \times \mathbf{u}) \times \hat{n} = \text{DtN}[\mathbf{u}] & \mathbf{r} \in \partial\Omega, \end{cases} \quad (3.85)$$

that is

$$\begin{aligned}
 \int_{\Omega} \nabla \times \mathbf{u} \cdot \nabla \times \bar{\mathbf{v}} - k^2 \mathbf{u} \cdot \bar{\mathbf{v}} \, d\mathbf{r} - \int_{\partial\Omega} \text{DtN}[\mathbf{u}] \cdot \bar{\mathbf{v}} \, ds & & (3.86) \\
 = \int_{\Omega} \bar{\mathbf{v}} \cdot (D\mathcal{V} + D\mathcal{V}^T) \mathbf{E} \, d\mathbf{r} & \quad \forall \bar{\mathbf{v}} \in H_0(\text{curl}, \Omega).
 \end{aligned}$$

Similar to (3.82), we have

$$\|\mathbf{u}\|_{H^1(\Omega_s \cup \Omega_o)} + \|\nabla \times \mathbf{u}\|_{H^1(\Omega_s \cup \Omega_o)} \leq C \|\mathcal{V}\|_{W^{2,\infty}(\Omega)} \|\mathbf{E}\|_{H^1(\Omega_s \cup \Omega_c)}.$$

Using (3.86), we have

$$\begin{aligned}
 \left| \int_{\Omega} (\bar{\mathbf{P}} - \bar{\mathbf{P}}_h) \cdot (D\mathcal{V} + D\mathcal{V}^T) \mathbf{E} \, d\mathbf{r} \right| &= |a^*(\mathbf{P} - \mathbf{P}_h, \mathbf{u})| & (3.87) \\
 \leq |a^*(\mathbf{P} - \mathbf{P}_h, \mathbf{u} - \mathcal{I}_h \mathbf{u})| + \left| \int_{\Omega} (\mathcal{G}(\mathbf{E}) - \mathcal{G}(\mathbf{E}_h)) \cdot \mathcal{I}_h \mathbf{u} \, d\mathbf{r} \right|.
 \end{aligned}$$

3 Shape Gradient: Evaluation and Approximation

Using (3.56), (3.57), (3.73), and (3.71), we have

$$\begin{aligned}
 & \left| \int_{\Omega} (\bar{\mathbf{P}} - \bar{\mathbf{P}}_h) \cdot (D\mathcal{V} + D\mathcal{V}^T) \mathbf{E} \, d\mathbf{r} \right| \tag{3.88} \\
 & \leq C h^2 \|\mathcal{V}\|_{W^{2,\infty}(\Omega)} \|\mathbf{E}\|_{H^1(\Omega_s \cup \Omega_o)} \\
 & \left\{ \|\mathbf{P}\|_{H^1(\Omega_s \cup \Omega_o)} + \|\nabla \times \mathbf{P}\|_{H^1(\Omega_s \cup \Omega_o)} + \left(\|\mathbf{E}\|_{H^1(\Omega_s \cup \Omega_o)} + \|\nabla \times \mathbf{E}\|_{H^1(\Omega_s \cup \Omega_o)} \right) \right. \\
 & \quad \left. \left(1 + \|\kappa_f(\mathbf{r}, \hat{\mathbf{r}}_1)\|_{W^{1,\infty}(\Omega \times \Omega_{I_{ens}})} \|\nabla^{\mathbf{r}} \kappa_f(\mathbf{r}, \hat{\mathbf{r}}_1)\|_{W^{1,\infty}(\Omega \times \Omega_{I_{ens}})} \right) \right\}.
 \end{aligned}$$

For bounding the third integral on the right hand side of (3.79), we use Cauchy-Schwarz inequality, (3.57), and (3.76)

$$\begin{aligned}
 & \left| \int_{\Omega} (\mathbf{E} - \mathbf{E}_h) \cdot (D\mathcal{V} + D\mathcal{V}^T) (\bar{\mathbf{P}} - \bar{\mathbf{P}}_h) \, d\mathbf{r} \right| \tag{3.89} \\
 & \leq \|\mathcal{V}\|_{W^{1,\infty}(\Omega)} \|\mathbf{E} - \mathbf{E}_h\|_{L^2(\Omega)} \|\mathbf{P} - \mathbf{P}_h\|_{L^2(\Omega)} \\
 & \leq C h^2 \|\mathcal{V}\|_{W^{1,\infty}(\Omega)} (\|\mathbf{E}\|_{H^1(\Omega_s \cup \Omega_o)} + \|\nabla \times \mathbf{E}\|_{H^1(\Omega_s \cup \Omega_o)}) \\
 & \quad (\|\mathbf{P}\|_{H^1(\Omega_s \cup \Omega_o)} + \|\nabla \times \mathbf{P}\|_{H^1(\Omega_s \cup \Omega_o)} + \|\mathbf{E}\|_{H^1(\Omega_s \cup \Omega_o)} + \|\nabla \times \mathbf{E}\|_{H^1(\Omega_s \cup \Omega_o)}).
 \end{aligned}$$

Again, we split the third integral on the right hand side of (3.58) to bound it

$$\begin{aligned}
 & \int_{\Omega} \nabla \cdot \mathcal{V} (\nabla \times \mathbf{E} \cdot \nabla \times \bar{\mathbf{P}} + k^2 \mathbf{E} \cdot \bar{\mathbf{P}} - \nabla \times \mathbf{E}_h \cdot \nabla \times \bar{\mathbf{P}}_h - k^2 \mathbf{E}_h \cdot \bar{\mathbf{P}}_h) \, d\mathbf{r} \\
 & = \int_{\Omega} \nabla \cdot \mathcal{V} (\nabla \times (\mathbf{E} - \mathbf{E}_h) \cdot \nabla \times \bar{\mathbf{P}} + k^2 (\mathbf{E} - \mathbf{E}_h) \cdot \bar{\mathbf{P}}) \, d\mathbf{r} \\
 & \quad + \int_{\Omega} \nabla \cdot \mathcal{V} (\nabla \times \mathbf{E} \cdot \nabla \times (\bar{\mathbf{P}} - \bar{\mathbf{P}}_h) + k^2 \mathbf{E} \cdot (\bar{\mathbf{P}} - \bar{\mathbf{P}}_h)) \, d\mathbf{r} \\
 & \quad - \int_{\Omega} \nabla \cdot \mathcal{V} (\nabla \times (\mathbf{E} - \mathbf{E}_h) \cdot \nabla \times (\bar{\mathbf{P}} - \bar{\mathbf{P}}_h) + k^2 (\mathbf{E} - \mathbf{E}_h) \cdot (\bar{\mathbf{P}} - \bar{\mathbf{P}}_h)) \, d\mathbf{r}. \tag{3.90}
 \end{aligned}$$

We bound the first integral on the right side of (3.4.2) using duality technique. We introduce \mathbf{u} as the weak solution to the following BVP

$$\begin{cases} \nabla \times \nabla \times \bar{\mathbf{u}} - k^2(\mathbf{r})\bar{\mathbf{u}} = \nabla \times ((\nabla \cdot \mathcal{V}) \nabla \times \mathbf{P}) + k^2(\nabla \cdot \mathcal{V}) \mathbf{P} & \mathbf{r} \in \Omega, \\ \llbracket \gamma_t(\bar{\mathbf{u}}) \rrbracket = 0 & \mathbf{r} \in \partial\Omega_s, \\ \llbracket \gamma_t(\nabla \times \bar{\mathbf{u}}) \rrbracket = 0 & \mathbf{r} \in \partial\Omega_s, \\ \nabla \times \bar{\mathbf{u}} \times \hat{n}, = \overline{\text{DtN}^*[\mathbf{u}]} & \mathbf{r} \in \partial\Omega, \end{cases} \quad (3.91)$$

that is

$$\begin{aligned} & \int_{\Omega} \nabla \times \mathbf{u} \cdot \nabla \times \mathbf{v} - k^2 \mathbf{u} \cdot \mathbf{v} \, d\mathbf{r} - \int_{\partial\Omega} \text{DtN}^*[\mathbf{u}] \cdot \mathbf{v} \, ds \\ & = \int_{\Omega} \nabla \cdot \mathcal{V} (\nabla \times \mathbf{v} \cdot \nabla \times \bar{\mathbf{P}} + k^2 \mathbf{v} \cdot \bar{\mathbf{P}}) \quad \forall \mathbf{v} \in H_0(\text{curl}, \Omega). \end{aligned} \quad (3.92)$$

Using Assumption 3.52, we have

$$\|\mathbf{u}\|_{H^1(\Omega_s \cup \Omega_c)} + \|\nabla \times \mathbf{u}\|_{H^1(\Omega_s \cup \Omega_c)} \leq \|\mathcal{V}\|_{W^{2,\infty}} \|\nabla \times \mathbf{P}\|_{H^1(\Omega_s \cup \Omega_c)} \quad (3.93)$$

Then, by (3.91), Galerkin orthogonality, continuity of $a(\cdot, \cdot)$, (3.56), and (3.57),

$$\begin{aligned} & \left| \int_{\Omega} \nabla \cdot \mathcal{V} (\nabla \times (\mathbf{E} - \mathbf{E}_h) \cdot \nabla \times \bar{\mathbf{P}} + k^2 (\mathbf{E} - \mathbf{E}_h) \cdot \bar{\mathbf{P}}) \, d\mathbf{r} \right| \\ & = |a(\mathbf{E} - \mathbf{E}_h, \bar{\mathbf{u}})| \\ & = |a(\mathbf{E} - \mathbf{E}_h, \bar{\mathbf{u}} - \mathcal{I}_h \bar{\mathbf{u}})| \\ & \leq C \|(\mathbf{E} - \mathbf{E}_h)\|_{H(\text{curl}, \Omega)} \|(\bar{\mathbf{u}} - \mathcal{I}_h \bar{\mathbf{u}})\|_{H(\text{curl}, \Omega)} \\ & \leq C h^2 (\|\mathbf{E}\|_{H^1(\Omega_s \cup \Omega_o)} + \|\nabla \times \mathbf{E}\|_{H^1(\Omega_s \cup \Omega_o)}) \|\mathcal{V}\|_{W^{2,\infty}} \|\nabla \times \mathbf{P}\|_{H^1(\Omega_s \cup \Omega_c)}. \end{aligned} \quad (3.94)$$

3 Shape Gradient: Evaluation and Approximation

For the second integral on the right hand side of (3.94), we used the duality technique again, and define \mathbf{u} as the weak solution to the following BVP

$$\begin{cases} \nabla \times \nabla \times \mathbf{u} - k^2(\mathbf{r})\mathbf{u} = \nabla \times ((\nabla \cdot \mathcal{V}) \nabla \times \mathbf{E}) + k^2 (\nabla \cdot \mathcal{V}) \mathbf{E} & \mathbf{r} \in \Omega, \\ \llbracket \gamma_t(\mathbf{u}) \rrbracket = 0 & \mathbf{r} \in \partial\Omega_s, \\ \llbracket \gamma_t(\nabla \times \mathbf{u}) \rrbracket = 0 & \mathbf{r} \in \partial\Omega_s, \\ \nabla \times \mathbf{u} \times \hat{n} = \text{DtN}[\mathbf{u}] & \mathbf{r} \in \partial\Omega, \end{cases} \quad (3.95)$$

that is

$$\begin{aligned} & \int_{\Omega} \nabla \times \mathbf{u} \cdot \nabla \times \bar{\mathbf{v}} - k^2 \mathbf{u} \cdot \bar{\mathbf{v}} \, d\mathbf{r} - \int_{\partial\Omega} \text{DtN}[\mathbf{u}] \cdot \bar{\mathbf{v}} \, ds \\ & = \int_{\Omega} \nabla \cdot \mathcal{V} (\nabla \times \bar{\mathbf{v}} \cdot \nabla \times \mathbf{E} + k^2 \bar{\mathbf{v}} \cdot \mathbf{E}) \quad \forall \bar{\mathbf{v}} \in H_0(\text{curl}, \Omega). \end{aligned} \quad (3.96)$$

Based on Assumption 3.52, we have

$$\|\mathbf{u}\|_{H^1(\Omega_s \cup \Omega_c)} + \|\nabla \times \mathbf{u}\|_{H^1(\Omega_s \cup \Omega_c)} \leq \|\mathcal{V}\|_{W^{2,\infty}} \|\nabla \times \mathbf{E}\|_{H^1(\Omega_s \cup \Omega_c)}. \quad (3.97)$$

Using (3.95), (3.37), and continuity of $a(\cdot, \cdot)$,

$$\begin{aligned} & \left| \int_{\Omega} \nabla \cdot \mathcal{V} (\nabla \times \mathbf{E} \cdot \nabla \times (\bar{\mathbf{P}} - \bar{\mathbf{P}}_h) + k^2 \mathbf{E} \cdot (\bar{\mathbf{P}} - \bar{\mathbf{P}}_h)) \, d\mathbf{r} \right| \\ & = |a^*(\bar{\mathbf{P}} - \bar{\mathbf{P}}_h, \mathbf{u})| \\ & = |a^*(\bar{\mathbf{P}} - \bar{\mathbf{P}}_h, \mathbf{u} - \mathcal{I}_h \mathbf{u}) + \int_{\Omega} (\mathcal{G}(\mathbf{E}) - \mathcal{G}(\mathbf{E}_h)) \cdot \mathcal{I}_h \mathbf{u} \, d\mathbf{r}| \\ & \leq C \|\bar{\mathbf{P}} - \bar{\mathbf{P}}_h\|_{H(\text{curl}, \Omega)} \|\mathbf{u} - \mathbf{u}_h\|_{H(\text{curl}, \Omega)} + \left| \int_{\Omega} \mathcal{G}(\mathbf{E} - \mathbf{E}_h) \cdot \mathcal{I}_h \mathbf{u} \, d\mathbf{r} \right|. \end{aligned} \quad (3.98)$$

Using (3.76), (3.56), (3.57), (3.73), and (3.71) we have

$$\begin{aligned} & \left| \int_{\Omega} \nabla \cdot \mathcal{V} (\nabla \times \mathbf{E} \cdot \nabla \times (\bar{\mathbf{P}} - \bar{\mathbf{P}}_h) + k^2 \mathbf{E} \cdot (\bar{\mathbf{P}} - \bar{\mathbf{P}}_h)) \, d\mathbf{r} \right| \\ & \leq C h^2 \|\mathcal{V}\|_{W^{2,\infty}(\Omega)} \|\nabla \times \mathbf{E}\|_{H^1(\Omega_s \cup \Omega_c)} \\ & \left\{ \|\bar{\mathbf{P}}\|_{H^1(\Omega_s \cup \Omega_o)} + \|\nabla \times \bar{\mathbf{P}}\|_{H^1(\Omega_s \cup \Omega_o)} + \left(\|\mathbf{E}\|_{H^1(\Omega_s \cup \Omega_o)} + \|\nabla \times \mathbf{E}\|_{H^1(\Omega_s \cup \Omega_o)} \right) \right\} \end{aligned} \quad (3.99)$$

$$\left(1 + \|\kappa_f(\mathbf{r}, \hat{\mathbf{r}}_1)\|_{W^{1,\infty}(\Omega \times \Omega_{lens})} \|\nabla^{\mathbf{r}} \kappa_f(\mathbf{r}, \hat{\mathbf{r}}_1)\|_{W^{1,\infty}(\Omega \times \Omega_{lens})} \right) \Bigg\}.$$

In the end, we use Cauchy-Schwarz inequality, (3.57), and (3.76) to bound the third integral on the right hand side of (3.4.2)

$$\begin{aligned} & \int_{\Omega} \nabla \cdot \mathcal{V}(\nabla \times (\mathbf{E} - \mathbf{E}_h) \cdot \nabla \times (\bar{\mathbf{P}} - \bar{\mathbf{P}}_h) + k^2 (\mathbf{E} - \mathbf{E}_h) \cdot (\bar{\mathbf{P}} - \bar{\mathbf{P}}_h)) \, d\mathbf{x} \\ & \leq \|\mathcal{V}\|_{W^{1,\infty}(\Omega)} \|\mathbf{E} - \mathbf{E}_h\|_{H(\text{curl}, \Omega)} \|\bar{\mathbf{P}} - \bar{\mathbf{P}}_h\|_{H(\text{curl}, \Omega)} \\ & \leq C h^2 \|\mathcal{V}\|_{W^{1,\infty}} (\|\mathbf{E}\|_{H^1(\Omega_s \cup \Omega_o)} + \|\nabla \times \mathbf{E}\|_{H^1(\Omega_s \cup \Omega_o)}) \\ & (\|\mathbf{P}\|_{H^1(\Omega_s \cup \Omega_o)} + \|\nabla \times \mathbf{P}\|_{H^1(\Omega_s \cup \Omega_o)} + \|\mathbf{E}\|_{H^1(\Omega_s \cup \Omega_o)} + \|\nabla \times \mathbf{E}\|_{H^1(\Omega_s \cup \Omega_o)}). \end{aligned} \tag{3.100}$$

□

3.5 Numerical experiments

We numerically study the 2D problem of approximating the shape gradient for the quadratic shape functional

$$\mathcal{J}(\Omega) = \int_{\Omega} u^2 \, d\mathbf{x},$$

for $\Omega \subset \mathbb{R}^2$, under the scalar PDE constraint

$$\begin{cases} -\Delta u + u = f & \text{in } \Omega, \\ u = g & \text{on } \partial\Omega. \end{cases} \tag{3.101}$$

It is challenging to investigate convergence rates in the $C^1(\mathbb{R}^d; \mathbb{R}^d)$ dual norm numerically. Therefore, we consider only an operator norm over a finite dimensional space of vector fields in $\mathcal{P}_{3,3}(\mathbb{R}^2)$, whose components are multivariate product polynomials of degree three. Moreover, the $C^1(\mathbb{R}^d; \mathbb{R}^d)$ -norm is replaced with the $H^1(\Omega)$ -norm. By monitoring the following operator norm on different meshes which are generated through uniform refine-

3 Shape Gradient: Evaluation and Approximation

ment, one can study convergence rates

$$\text{err}^{\text{Vol}} := \left(\max_{\mathcal{V} \in \mathcal{P}_{3,3}} \frac{1}{\|\mathcal{V}\|_{H^1(\Omega)}^2} |d\mathcal{J}(\Omega; \mathcal{V}) - d\mathcal{J}(\Omega, u_h, p_h; \mathcal{V})^{\text{Vol}}|^2 \right)^{1/2}$$

and

$$\text{err}^{\text{Bdry}} := \left(\max_{\mathcal{V} \in \mathcal{P}_{3,3}} \frac{1}{\|\mathcal{V}\|_{H^1(\Omega)}^2} |d\mathcal{J}(\Omega; \mathcal{V}) - d\mathcal{J}(\Omega, u_h, p_h; \mathcal{V})^{\text{Bdry}}|^2 \right)^{1/2}$$

To compute the values err^{Vol} and err^{Bdry} , we introduce a basis $\{\mathcal{V}_i\}_{i=1}^m$, $m = 20$, of $\mathcal{P}_{3,3}(\mathbb{R}^2)$, and define the column vectors

$$\begin{aligned} \mathbf{z}^{\text{Vol}} &:= (d\mathcal{J}(\Omega; \mathcal{V}_i) - d\mathcal{J}(\Omega, u_h, p_h; \mathcal{V}_i)^{\text{Vol}})_{i=1}^m, \\ \mathbf{z}^{\text{Bdry}} &:= (d\mathcal{J}(\Omega; \mathcal{V}_i) - d\mathcal{J}(\Omega, u_h, p_h; \mathcal{V}_i)^{\text{Bdry}})_{i=1}^m. \end{aligned}$$

Let \mathbf{M} be the Gramian matrix of $\{\mathcal{V}_i\}_{i=1}^{20}$ with respect to the $H^1(\Omega)$ inner product, and consider the matrices \mathbf{A}^{Vol} and \mathbf{A}^{Bdry} defined by

$$\{\mathbf{A}^{\text{Vol}}\}_{i,j=1}^{20} = \mathbf{z}^{\text{Vol}}(\mathbf{z}^{\text{Vol}})^T \quad \text{and} \quad \{\mathbf{A}^{\text{Bdry}}\}_{i,j=1}^{20} = \mathbf{z}^{\text{Bdry}}(\mathbf{z}^{\text{Bdry}})^T,$$

respectively. Then, err^{Vol} and err^{Bdry} can be obtained as the square roots of the maximal eigenvalues of $\mathbf{M}^{-1}\mathbf{A}^{\text{Vol}}$ and $\mathbf{M}^{-1}\mathbf{A}^{\text{Bdry}}$, respectively.

Although analytical values are in some cases computable, the reference values $d\mathcal{J}(\Omega; \mathcal{V})$ are approximated by evaluating $d\mathcal{J}(\Omega, u_h, p_h; \mathcal{V})^{\text{Vol}}$ on a mesh with an extra level of refinement. This gives us much flexibility in the selection of test cases (the same code can be used for different geometries Ω , source functions f and g , and vector fields \mathcal{V}).

In the implementation, we opt for linear Lagrangian finite elements on quasi-uniform triangular meshes⁵. Integrals in the domain are computed by a 7-point quadrature rule in each triangle and line integrals with a 6-point

⁵The experiments are performed in MATLAB and are based on the library LehrFEM developed at ETHZ.

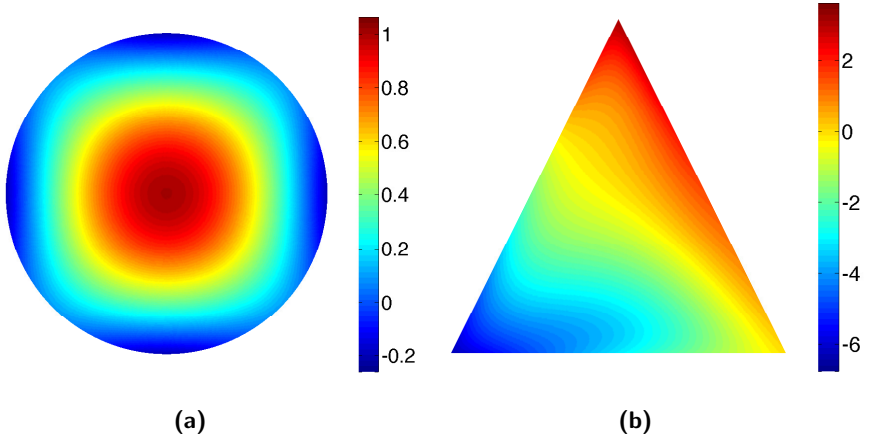


Figure 3.2: Plot of the solution u of the state problem in the computational domain Ω for the (a) first and the (b) second numerical experiment.

Gauss quadrature on each segment.

The **first numerical experiment** is constructed starting from the solution

$$u(x, y) = \cos(x) \cos(y)$$

and setting f and g accordingly. The computational domain is a disc with radius $\sqrt{\pi}$ (see Figure 3.2a). The predicted quadratic and linear convergence with respect to the meshwidth h for formulas (3.8) and (3.23), respectively, are evident in Figure 3.3a.

The **second experiment** is performed on a triangle with corners located at $(-\pi, -\pi)$, $(\pi, -\pi)$, and $(0, \pi)$ (see Figure 3.2b). The source function and the boundary data are chosen as follows:

$$f(x, y) = x^2 - y^2, \quad g(x, y) = x + y.$$

Again, the rates of convergence predicted in Theorems 7 and 8 are confirmed by the experiment, see Figure 3.3b.

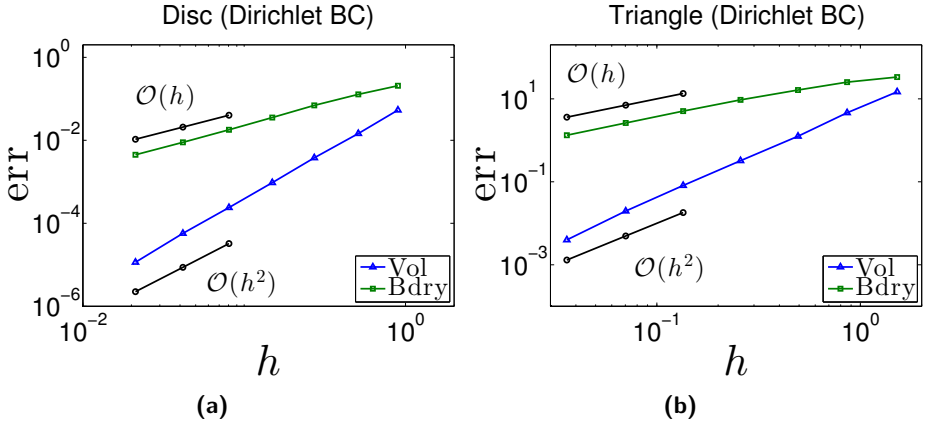


Figure 3.3: Convergence study for the (a) first and the (b) second numerical experiment. Obviously, Formula (3.8) is better suited for a finite element approximation of the Eulerian derivative $d\mathcal{J}(\Omega; \mathcal{V})$ than Formula (3.23).

The **third numerical experiment** is conducted on a domain which does not guarantee H^2 -regularity of the state problem (3.4), see Figure 3.4a. The source and the boundary functions, in polar coordinates, are $f(\mathbf{x}) = r^{2/3} \cos(2\varphi/3)$ and $g(\mathbf{x}) = 0$, respectively. As expected, the convergence rates deteriorate to fractional values due to the presence of a re-entrant corner which, with an interior angle of size $2\pi \cdot 60/61$, affects the regularity of the functions u and p .

In the **fourth numerical experiment**, we investigate the *Neumann problem* and the accuracy of Formulas (3.9) and (3.25), for which we expect results similar to the Dirichlet case. We consider the solution

$$u(x, y) = \cos(x - 1) \cos(y + 1)$$

and we choose f and g accordingly. The computational domain is a disc with radius $\sqrt{\pi}$ (see Figure 3.5, left). Surprisingly, we observe that Formula (3.25) performs as well as Formula (3.9), showing quadratic convergence in the meshwidth h , too (see Figure 3.6, left).

This surprising observation is not confined to smooth domains, as will be

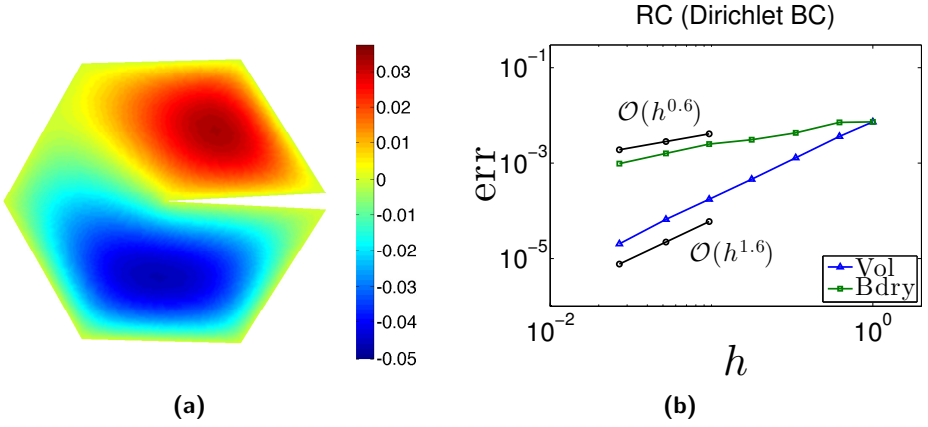


Figure 3.4: (a) Plot of the solution u of the state problem in the computational domain Ω for the third numerical experiment, and (b) corresponding convergence study. Due to the poor regularity of the functions u and p , the convergence rate of $d\mathcal{J}(\Omega, u_h, p_h; \mathcal{V})^{\text{Vol}}$ and $d\mathcal{J}(\Omega, u_h, p_h; \mathcal{V})^{\text{Bdry}}$ deteriorate.

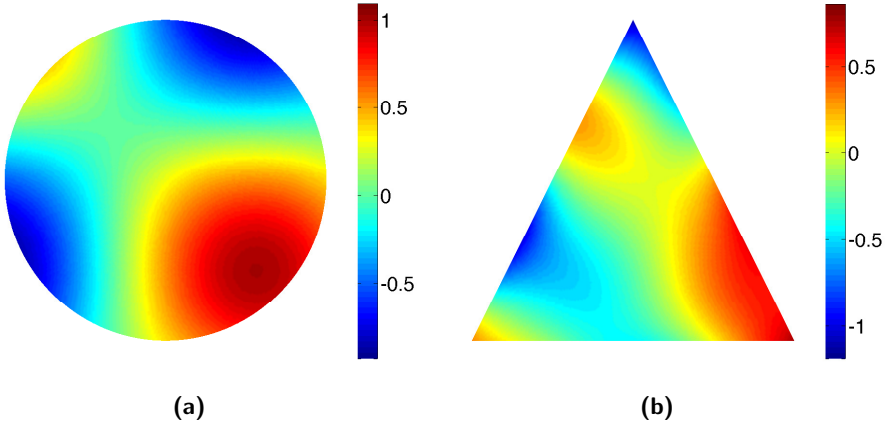


Figure 3.5: Plot of the solution u of the state problem in the computational domain Ω for the (a) fourth and the (b) fifth numerical experiment.

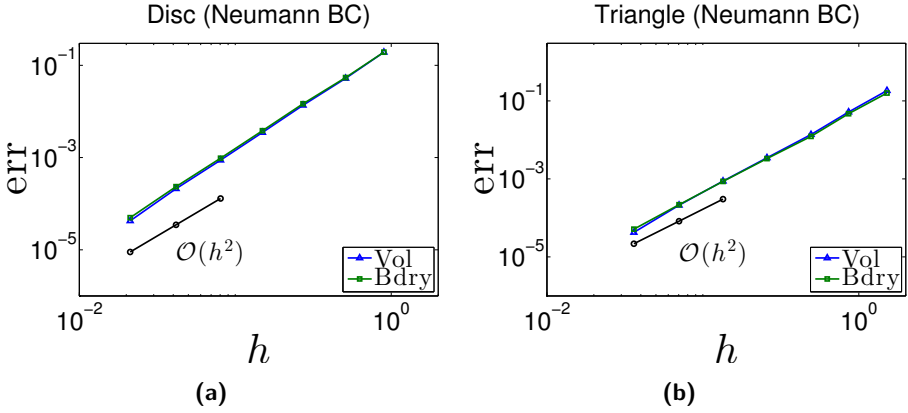


Figure 3.6: Convergence study for the (a) fourth and (b) fifth numerical experiment. The quadratic convergence of $d\mathcal{J}(\Omega, u_h, p_h; \mathcal{V})^{\text{Bdry}}$ is unexpected.

demonstrated by our **fifth numerical experiment**. It investigates the convergence for the *Neumann case* on a triangle with corners located at $(-\pi, -\pi)$, $(\pi, -\pi)$, and $(0, \pi)$ (see Figure 3.5, right). The source function and the boundary data are set as follows:

$$f(x, y) = \cos(x + 1) \cos(y - 1), \quad g(x, y) = \cos(x - 1) \cos(y + 1).$$

Again, we observe that Formula (3.25), corrected according to Remark 8, converges quadratically in the meshwith h (see Figure 3.6, right).

Nevertheless, the **sixth numerical experiment**, which studies the Neumann boundary value problem again, shows that Formula (3.9) is superior to (3.25) in terms of accuracy and convergence in case of domains which do not guarantee H^2 -regularity, see Figure 3.7. The source and the boundary functions are chosen as in the third numerical experiment.

Finally, all experiments are repeated considering the operator norm on the subspace of multivariate polynomials of degree two instead of three. The measured errors well agree with those reported above, see Figure 3.8. Thus, the arbitrary choice of computing the operator norm on the finite dimen-

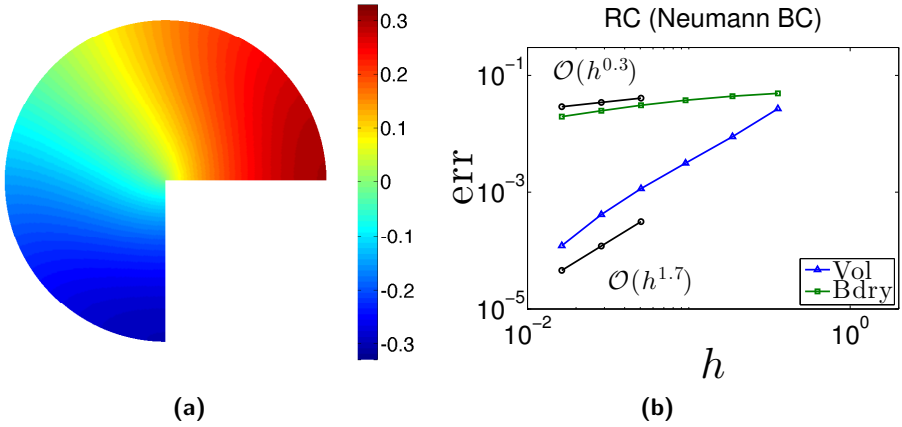


Figure 3.7: (a) Plot of the solution u of the state problem in the computational domain Ω for the sixth numerical experiment, and (b) corresponding convergence study. Due to the poor regularity of the functions u and p , the convergence rate of $d\mathcal{J}(\Omega, u_h, p_h; \mathcal{V})^{\text{Vol}}$ and $d\mathcal{J}(\Omega, u_h, p_h; \mathcal{V})^{\text{Bdry}}$ deteriorate.

sional subspace of multivariate polynomial vector fields of degree three does not seem to compromise our observations.

3 Shape Gradient: Evaluation and Approximation

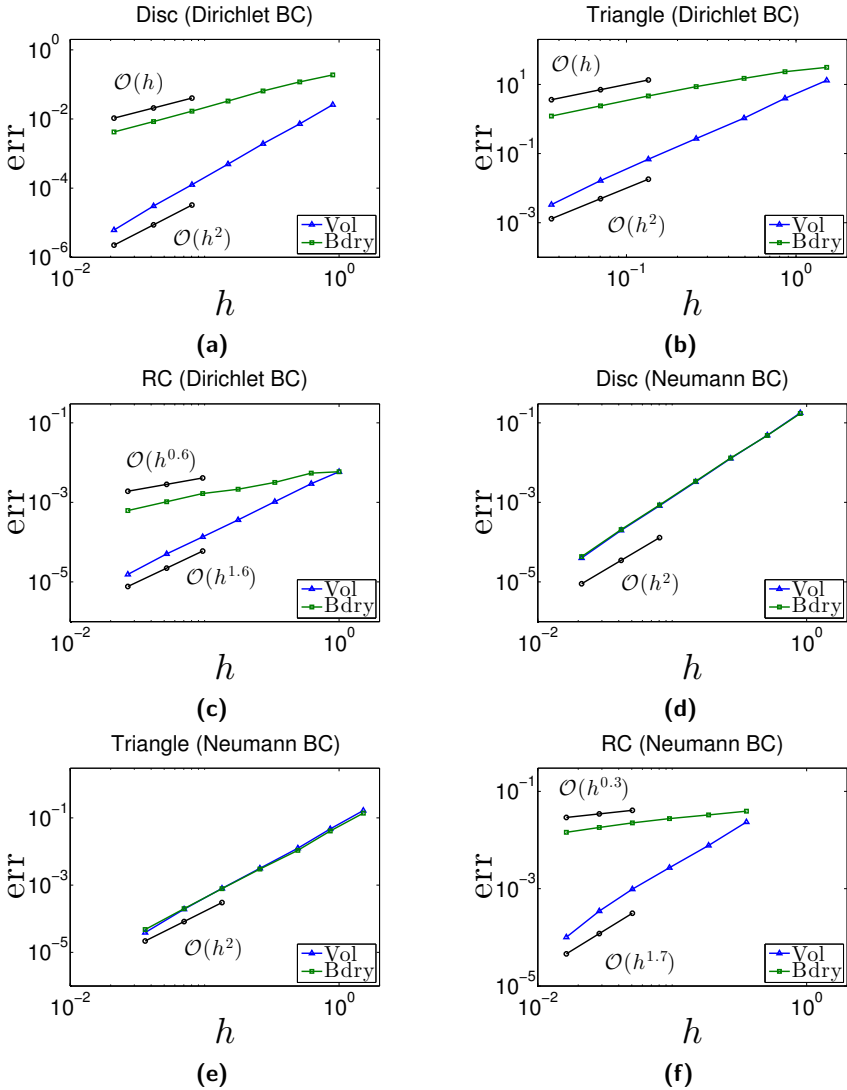


Figure 3.8: Convergence study for the (a) first, (b) second, (c) third, (d) fourth, (e) fifth and (f) sixth numerical experiment, when considering the operator norm on the subspace of multivariate polynomials of degree two. The results agree with those obtained with cubic polynomials.

4 Sensitivity analysis for scattering problems

4.1 Introduction

During the last decades, plasmonic nano particles attracted interests due to their localized field enhancement properties. The localized field can be exploited, e.g. for amplifying Raman and fluorescence scattering [37, 53, 68, 72]. The effect of the shape and the size of nano particles on the performance of the device has been studied thoroughly in literature [25, 41, 54]. Most simulations investigate only the impact of a limited number of geometric parameters.

Any change of shape can have a significant effect on the behavior of the structure. Since fabrication-based perturbations are inevitable, it is important to study the sensitivity of the performance of a structure with respect to small shape variations.

Shape sensitivity analysis studies how sensitive the output functional \mathcal{J} is with respect to variations of the domain shape. In electromagnetic scattering problems, the shape functional measures a physical quantity of the problem. It is important that the quantity has some practical meaning and can be measured. For example in most of optical experiments the field value at far distances is measured through a lens. So, we mostly use the far-field functional provided in Chapter 2 as the PDE constrained shape functional in this chapter.

The shape sensitivity is measured through the evaluation of the shape gradient of \mathcal{J} . In the previous chapter, we investigated the derivation of shape gradients for scattering problems. In this chapter, we probe the shape gradient using perturbations with local support over the surface of the scatterer to see the effect of local changes of the shape on the output functional. Sec-

ond order B-splines are used as probing perturbation fields.

To get a representation of the shape sensitivity over the surface of the scatterer, we use the Hadamard-Zolesio structure theorem to define a representative function g based on local shape gradients. We explicitly provide g for different nano particles with different shape functionals. The gold or silver nano particles are located either in free space or on a substrate.

4.2 Numerical Approximation of the Shape Gradient

To derive $d\mathcal{J}$, we need to solve the variational problems (3.35a) and (3.36) numerically. Similar to Chapter 2, we use NGSolve as a finite element solver to find solutions of state and adjoint problems. In Section 4.4, we discuss thoroughly about the procedure of using NGSolve to derive the shape sensitivity.

Another issue that we need to address is the definition of the corresponding vector field \mathcal{V} . Our aim is to examine the sensitivity of the shape functional with respect to local perturbations. Therefore, we consider only finitely many vector fields $V_n = \{\mathcal{V}_i\}_{i=1}^n$ ($n = \dim V_n$) with compact support over the surface of the scatterer $\partial\Omega_s$ as probing perturbation functions¹

$$\mathcal{V}_i = B_i \hat{\ell}_i, \quad (4.1)$$

where B_i is a tensor product B-spline of degree 2 centered on $\mathbf{r}_i \in \Omega$. By $\hat{\ell}_i$, we denote the direction of \mathcal{V}_i ($\hat{\ell}_i \in \mathbb{R}^3$ and $|\hat{\ell}_i| = 1$). Tensor product B-splines are defined within boxes which are aligned with Cartesian coordinates. Based on the Hadamard structure theorem for smooth surfaces, $d\mathcal{J}$ is uniquely determined by the normal component of \mathcal{V} on $\partial\Omega_s$ (see [21, Ch. 9]). Therefore, we center B-splines on $\mathbf{r}_i \in \partial\Omega_s$, and set $\hat{\ell}_i$ to be in the direction normal to $\partial\Omega_s$ at the point \mathbf{r}_i .

To simplify implementations, we locate \mathbf{r}_i on vertices of a mesh which is independent of the FEM mesh. The B-spline mesh covers $\partial\Omega_s$ and is adapted to the shape of the surface. The size of the B-spline mesh must

¹We assume that $\mathcal{V} = 0$ on the outer boundary $\partial\Omega$.

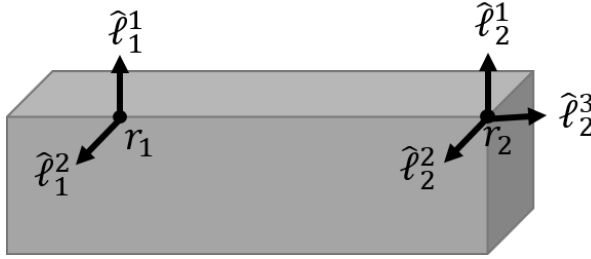


Figure 4.1: Directions of B-splines assigned to \mathbf{r}_1 and \mathbf{r}_2 located on an edge and on a corner, respectively.

be fine enough to model surface perturbations properly. In our simulations, we observe that $\max(h_B) = 3 \max(h_{\text{FEM}})$ is a good choice (h_B and h_{FEM} are element sizes of the B-spline mesh and the FEM mesh, respectively). In Section 4.5, we give detailed plots of B-spline meshes adapted to each structure.

To keep sensitivity probing local, one must choose the support of B-splines ΔS_{B_i} as small as possible. However, to be able to evaluate $d\mathcal{J}$ accurately, ΔS_{B_i} must be big enough to comprise a sufficient number of elements of FEM mesh. This means that ΔS_{B_i} is linked to the mesh width. According to our experience, we found that $\Delta S_{B_i} = 4 h_{\text{FEM}}(\mathbf{r}_i)$ is a good choice.

Another issue concerning B-spline mesh is the definition of $\hat{\ell}_i$ along edges or on corners. There are several ways to resolve this problem. One option is to avoid corners and edges, i.e. to arrange the B-spline mesh such that no vertex is located directly on the edge. Another option is to consider the direction of $\hat{\ell}_i$ as an average of normal vectors over the faces sharing the corresponding edge or corner. Our solution is a combination of two previous approaches. As shown in Figure 4.1, we assign more than one B-Spline $\{B_i \hat{\ell}_i^j\}_{j=1}^q$ at vertices which are located on edges or corners. The number of B-splines q is equal to the number of faces that share the given edge or corner. By $\hat{\ell}_i^j$, we denote the normal direction on the j -th face sharing the corresponding edge or corner.

4.3 Function Representative of the Shape Gradient

The derived values for shape gradients based on probing perturbations (4.1) are defined locally on the surface of the scatterer. To obtain a representative function $g(\partial\Omega_s)$ of $d\mathcal{J}$ on the boundary $\partial\Omega_s$, we use the Hadamard-Zolesio structure theorem [21, Ch. 9, Thm 3.6] which, for smooth $\partial\Omega_s$, guarantees the existence of a function $g : \partial\Omega_s \rightarrow \mathbb{R}$ such that

$$\int_{\partial\Omega_s} (\mathcal{V} \cdot \hat{n}) g \, ds(\mathbf{r}) = d\mathcal{J}(\Omega; \mathcal{V}) \quad \forall \mathcal{V} \in C^1(\mathbb{R}^3, \mathbb{R}^3). \quad (4.2)$$

If the output functional measures the energy flux, then the dimension of g is $[\frac{J}{m^4}]$. To compute g numerically, we discretize the function space of g and define $g_h \in Y_h$ as follows

$$g_h(\mathbf{r}) = \sum_{j=1}^m \tilde{g}_j b_j(\mathbf{r}), \quad (4.3)$$

where $\tilde{g}_j \in \mathbb{R}$, and $b_j \in Y_h$ are continuous basis functions of $Y_h \subset H^1(\partial\Omega_s)$, $j = 1, \dots, m$, with $m = \dim Y_h$.

Using (4.2) and (4.3), we have

$$\tilde{\mathbf{A}} \mathbf{g} = \mathbf{f}, \quad (4.4)$$

where $\mathbf{g} = (\tilde{g}_1, \dots, \tilde{g}_m)^\top$ and $\mathbf{f} = (d\mathcal{J}(D; \mathcal{V}_1), \dots, d\mathcal{J}(D; \mathcal{V}_n))^\top$. By $\tilde{\mathbf{A}}$ we denote a $n \times m$ matrix as follows

$$\tilde{\mathbf{A}}_{ij} = \int_{\partial\Omega_s} (\mathcal{V}_i \cdot \hat{n}) b_j \, ds(\mathbf{r}). \quad (4.5)$$

In order to be able to find g_h , we need Y_h to be large enough, i.e. $m > n$. Under this assumption, the system of linear equations in (4.4) is underdetermined. Using the least squares method, we define

$$\tilde{X} := \operatorname{argmin}_{\mathbf{x} \in \mathbb{R}^m} \|\tilde{\mathbf{A}}\mathbf{x} - \mathbf{f}\|_{\mathbb{R}^n}. \quad (4.6)$$

We must mention that \tilde{X} is a set which can contain more than one element. To obtain a unique result, we use the H^1 -regularization and define \mathbf{g} as an element of \tilde{X} which has the minimum norm

$$\mathbf{g} = \underset{\mathbf{x} \in \tilde{X}}{\operatorname{argmin}} \|\mathbf{x}\|_{\mathbf{H}}, \quad (4.7)$$

where $\|\mathbf{x}\|_{\mathbf{H}} = \mathbf{x}^\top \mathbf{H} \mathbf{x}$. By \mathbf{H} we denote a $m \times m$ matrix with $\mathbf{H}_{ij} = \int_{\partial\Omega_s} \nabla_t u_i \cdot \nabla_t b_j$ (∇_t is the tangential gradient on the surface $\partial\Omega_s$).

Remark 10. *The choice of H^1 seminorm in (4.7) is arbitrary, however, we experienced that employing L^2 -regularization creates artifacts. Employing higher order regularizations might be too strong constraint.*

4.4 NGSolve implementation

Simulations in this chapter are based on the NGSolve library. We are mainly interested in the shape functionals that measure either the far-field or the near-field pattern of gold or silver nano particles. Here, we explain the procedure for the far-field functional which is more complex than the near-field.

In experimental setups, a lens measures the power flux over Ω_{lens} which is proportional to the following functional

$$\mathcal{J}(\mathbf{E}, \Omega) = \int_{\Omega_{lens}} |\mathbf{E}_\infty(\hat{\mathbf{r}})|^2 d\hat{\mathbf{r}} \quad (r \rightarrow \infty). \quad (4.8)$$

where Ω_{lens} is the area of the objective with the opening angle of $\alpha = 74^\circ$ and centered on the z-axis. Based on Chapter 2, the far-field pattern \mathbf{E}_∞ in the direction $\hat{\ell}$ at point $\hat{\mathbf{r}}$ can be obtained in terms of the Green's function $\mathbf{G}_\infty(\hat{\mathbf{r}}, \mathbf{r}, \hat{\ell})$

$$\begin{aligned} \mathbf{E}_\infty \cdot \hat{\ell} = \int_{\Omega_f} (\nabla \times \mathbf{E}(\mathbf{r})) \cdot \nabla \times \left(\Psi(\mathbf{r}) \mathbf{G}_\infty(\hat{\mathbf{r}}, \mathbf{r}, \hat{\ell}) \right) \\ - (\nabla^{\mathbf{r}} \times \mathbf{G}_\infty(\hat{\mathbf{r}}, \mathbf{r}, \hat{\ell})) \cdot \nabla^{\mathbf{r}} \times (\Psi(\mathbf{r}) \mathbf{E}(\mathbf{r})) \, d\mathbf{r}, \end{aligned} \quad (4.9)$$

where \mathbf{E} is the electric field, Ω_f is a subregion between two closed paths Γ_i and Γ_o around the scatterer (see Figure 3.1), and $\Psi(\mathbf{r})$ is a cutoff function

4 Sensitivity analysis for scattering problems

such that

$$\Psi(\mathbf{r})|_{\Gamma_i} \equiv 1, \text{ and } \Psi(\mathbf{r})|_{\Gamma_0} \equiv 0. \quad (4.10)$$

Since in our numerical simulations we do not perform convergence analysis (see Section 3.3.2), we consider the simple cutoff function in (2.72).

To obtain $d\mathcal{J}$, we first need to solve state and adjoint problems. The procedure to solve the state problem is already explained in Section 2.5. The adjoint \mathbf{P} is the solution to the following variational problem

$$\begin{aligned} & \int_{\Omega} \nabla \times \bar{\mathbf{P}} \cdot \nabla \times \mathbf{W} - k^2(\mathbf{r}) \bar{\mathbf{P}} \cdot \mathbf{W} \, d\mathbf{r} - \int_{\partial\Omega_s} \overline{\text{DtN}^*[\mathbf{P}]} \cdot \mathbf{W} \, ds(\mathbf{r}) \\ & = \int_{\Omega_{\text{tens}}} \bar{\mathbf{E}}_{\infty} \cdot \left\langle \frac{\partial \mathbf{E}_{\infty}}{\partial \mathbf{E}}, \mathbf{W} \right\rangle_{\Omega_f} \, d\mathbf{r} \quad \forall \mathbf{W} \in H(\text{curl}, \Omega) \end{aligned} \quad (4.11)$$

Similar to the state problem, we use PML to truncate the solution domain of the adjoint problem (see Section 2.5). We also use the same finite element space $X_h \in H(\text{curl}, \Omega)$ with the basis $\{\mathbf{b}_j\}_{j=1}^N$ as in Section 2.5 to solve (4.11).

Finally, Equation (4.11) in terms of (2.77) will be

$$a_0(\mathbf{W}, \mathbf{P}) = \ell_{\text{adj}}(\mathbf{W}), \quad (4.12)$$

where $\ell_{\text{adj}} : H(\text{curl}, \Omega) \mapsto \mathbb{C}$ is the linear form

$$\ell_{\text{adj}}(\mathbf{W}) = \int_{\Omega_{\text{tens}}} \ell_d(\bar{\mathbf{E}}, \hat{\mathbf{r}}) \cdot \ell_d(\mathbf{W}, \hat{\mathbf{r}}) \, d\hat{\mathbf{r}}, \quad (4.13)$$

and by $\ell_d : H(\text{curl}, \Omega) \times \mathbb{R}^3 \mapsto \mathbb{C}$, we denote

$$\begin{aligned} \ell_d(\mathbf{u}, \hat{\mathbf{r}}) = & \int_{\Omega_f} \nabla \times \mathbf{u}(\mathbf{r}) \cdot \nabla \times \left(\Psi(\mathbf{r}) \mathbf{G}_{\infty}(\hat{\mathbf{r}}, \mathbf{r}, \hat{\ell}) \right) \\ & - \nabla \times \mathbf{G}_{\infty}(\hat{\mathbf{r}}, \mathbf{r}, \hat{\ell}) \cdot \nabla \times (\Psi(\mathbf{r}) \mathbf{u}(\mathbf{r})) \, d\mathbf{r}. \end{aligned} \quad (4.14)$$

Based on (4.12), we need to assemble the stiffness matrix of a_0 with respect to the basis $\{\mathbf{b}_j\}_{j=1}^N$ just once and use it to solve both state and adjoint problems.

To calculate (4.13), we use Gauss-Legendre quadrature rule with quadrature points $\hat{\mathbf{r}}_i$, $i = 1, \dots, M$ (M is the number of quadrature points). Then, we discretize ℓ_d at each quadrature point with respect to the bases $\{\mathbf{b}_j\}_{j=1}^N$. To obtain the vector $\mathbf{f}_d^i = (\ell_d(\mathbf{b}_j, \hat{\mathbf{r}}_i))_{j=1}^N$, we first need to rewrite (4.14) in a more suitable format which can easily be evaluated using NGSolve integrators

$$\ell_d = a_{d_1}(\Psi \mathbf{G}_\infty, \mathbf{W}) - a_{d_2}(\mathbf{G}_\infty, \mathbf{W}) - a_{d_3}(\nabla \Psi \times \nabla \times \mathbf{G}_\infty, \mathbf{W}), \quad (4.15)$$

where $a_{d_1}, a_{d_2}, a_{d_3} : H(\text{curl}, \Omega) \times H(\text{curl}, \Omega) \mapsto \mathbb{C}$ are

$$a_{d_1}(\mathbf{u}_1, \mathbf{u}_2) = \int_{\Omega} \alpha_d(\mathbf{r}) \nabla \times \mathbf{u}_1 \cdot \nabla \times \mathbf{u}_2 \, d\mathbf{r}, \quad (4.16)$$

$$a_{d_2}(\mathbf{u}_1, \mathbf{u}_2) = \int_{\Omega} \alpha_d(\mathbf{r}) \Psi(\mathbf{r}) \nabla \times \mathbf{u}_1 \cdot \nabla \times \mathbf{u}_2 \, d\mathbf{r},$$

$$a_{d_3}(\mathbf{u}_1, \mathbf{u}_2) = \int_{\Omega} \alpha_d(\mathbf{r}) \mathbf{u}_1 \cdot \mathbf{u}_2 \, d\mathbf{r},$$

$$\text{and } \alpha_d(\mathbf{r}) = \begin{cases} 1 & \mathbf{r} \in \Omega_f \\ 0 & \mathbf{r} \in \Omega/\Omega_f \end{cases}.$$

Then, we can write the vector \mathbf{f}_d^i as follows

$$\mathbf{f}_d^i = \tilde{\mathbf{A}}_{d_1} \mathbf{g}_{d_1}^i - \tilde{\mathbf{A}}_{d_2} \mathbf{g}_{d_2}^i - \tilde{\mathbf{A}}_{d_3} \mathbf{g}_{d_3}^i, \quad (4.17)$$

where $\tilde{\mathbf{A}}_{d_1}$, $\tilde{\mathbf{A}}_{d_2}$, and $\tilde{\mathbf{A}}_{d_3}$ are stiffness matrices of bilinear forms a_{d_1} , a_{d_2} , and a_{d_3} , respectively². By $\mathbf{g}_{d_1}^i$, $\mathbf{g}_{d_2}^i$, and $\mathbf{g}_{d_3}^i$ we denote coefficient vectors of $\Psi(\mathbf{r}) \mathbf{G}_\infty(\mathbf{r}, \hat{\mathbf{r}}_i, \hat{\ell})$, $\mathbf{G}_\infty(\mathbf{r}, \hat{\mathbf{r}}_i, \hat{\ell})$, and $\nabla \Psi(\mathbf{r}) \times \nabla \times \mathbf{G}_\infty(\mathbf{r}, \hat{\mathbf{r}}_i, \hat{\ell})$, respectively. Since matrices $\tilde{\mathbf{A}}_{d_1}$, $\tilde{\mathbf{A}}_{d_2}$, and $\tilde{\mathbf{A}}_{d_3}$ are independent of quadrature points $\hat{\mathbf{r}}_i$, we need to assemble them just once and use them to calculate \mathbf{f}_d^i for all integration points.

The final form of the right hand side vector for adjoint problem is obtained

²All stiffness matrices and coefficient vectors in this chapter are with respect to the basis $\{\mathbf{b}_j\}_{j=1}^N$.

4 Sensitivity analysis for scattering problems

as follows

$$\mathbf{f}_{adj} = \sum_{i=1}^M w_i (\mathbf{g}_e^T \mathbf{f}_d^i) \mathbf{f}_d^i, \quad (4.18)$$

where $\{w_i\}_{i=1}^M$ are the integration-rule weights and M is the number of quadrature points. By \mathbf{g}_e we denote the coefficient vector of \mathbf{E} which is calculated by solving the state problem.

Here is a part of our code to assemble $\tilde{\mathbf{A}}_{d_1}$, $\tilde{\mathbf{A}}_{d_2}$, and $\tilde{\mathbf{A}}_{d_3}$

```
/*Assembling the stiffness matrix of bilinear  
form a_d1.  
The bilinear form integrator bfi_a_d1 is  
CurlCurlEdgeIntegrator  
with piecewise constant coefficient "alpha"  
which is equal  
to one inside the far-field integration region  
and zero elsewhere.*/  
BilinearFormIntegrator *bfi_a_d1;  
bfi_a_d1=new  
CurlCurlEdgeIntegrator<3>(alpha);  
a_d1 -> AddIntegrator (bfi_a_d1);  
a_d1-> Assemble(lh);  
  
/*Assembling the stiffness matrix of bilinear  
form a_d2.  
The bilinear form integrator bfi_a_d2 is  
CurlCurlEdgeIntegrator  
with piecewise constant coefficient "Psi_alpha"  
which is equal  
to "\Psi" inside the far-field integration region  
and zero elsewhere.*/  
BilinearFormIntegrator *bfi_a_d2;  
bfi_a_d2=new  
CurlCurlEdgeIntegrator<3>(Psi_alpha);  
a_d2 -> AddIntegrator (bfi_a_d2);  
a_d2-> Assemble(lh);
```

```

/*Assembling the stiffness matrix of bilinear
   form a_d3.
The bilinear form integrator bfi_a_d3 is
   MassEdgeIntegrator
with piecewise constant coefficient "alpha"
   which is equal
to one inside the far-field integration region
and zero elsewhere.*/
BilinearFormIntegrator *bfi_a_d3;
bfi_a_d3=new MassEdgeIntegrator<3>(alpha);
a_d3 -> AddIntegrator (bfi_a_d3);
a_d3-> Assemble(1h);

```

Based on Section 3.3.2, the shape gradient for wave scattering problems is

$$d\mathcal{J} = \operatorname{Re} a_s(\mathbf{E}, \mathbf{P}), \quad (4.19)$$

where

$$\begin{aligned}
a_s(\mathbf{u}_1, \mathbf{u}_2) = & \int_{\Omega} \nabla \times \mathbf{u}_1 \cdot (\mathbf{D}\mathcal{V} + \mathbf{D}\mathcal{V}^{\top}) \nabla \times \bar{\mathbf{u}}_2 + \mathbf{u}_1 \cdot (\mathbf{D}\mathcal{V} + \mathbf{D}\mathcal{V}^{\top}) \bar{\mathbf{u}}_2 \\
& - \nabla \cdot \mathcal{V} (\nabla \times \mathbf{u}_1 \cdot \nabla \times \bar{\mathbf{u}}_2 + k^2(\mathbf{r}) \mathbf{u}_1 \cdot \bar{\mathbf{u}}_2) d\mathbf{r}. \quad (4.20)
\end{aligned}$$

So, after finite element discretization we have

$$d\mathcal{J}^h = \operatorname{Re} \{ \mathbf{g}_e^T \tilde{\mathbf{A}}_s \mathbf{g}_p \}, \quad (4.21)$$

where \mathbf{g}_p is the coefficient vector of \mathbf{P} which is obtained by solving the adjoint problem, and $\tilde{\mathbf{A}}_s$ is the stiffness matrix of a_s .

4.5 Numerical results

4.5.1 Nano antenna consisting two gold spheres

In the first experiment, we investigate a gold nano antenna consisting of two identical spherical particles, sph-1 and sph-2, located in free space (see Figure 4.2a). The surrounding domain is air with refractive index $n_1 = 1$. Similar to Chapter 2, we use the measured data provided by [39] to obtain the optical constants of gold at a given frequency.

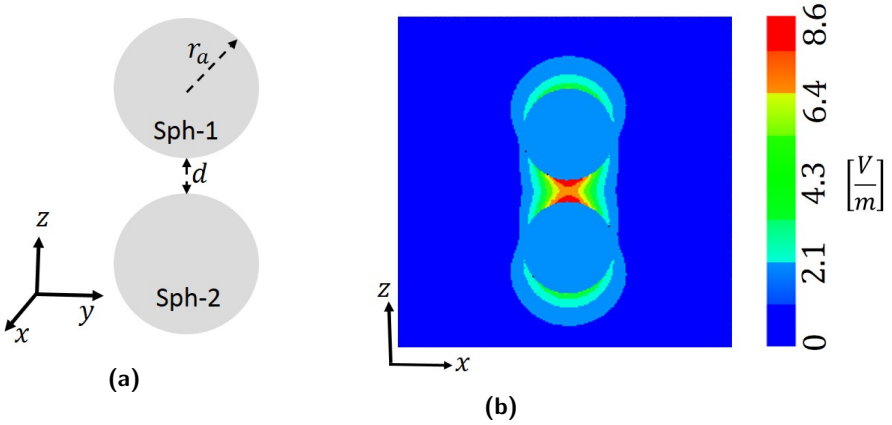


Figure 4.2: (a) Nano antenna consisting of two gold spheres with dimensions $(r_a, d) = (50, 23)nm$. (b) The absolute value of the electric field distribution at $\lambda = 640nm$.

The radii of spheres and the gap of the antenna are $50nm$ and $23nm$, respectively. In this experiment, we investigate the sensitivity of a functional that measures the energy in the near-field

$$\mathcal{J} = \int_{\Omega_m} |\mathbf{E}_s|^2 d\mathbf{r}, \quad (4.22)$$

where \mathbf{E}_s is the scattered field. The procedure for calculating shape gradients for the near-field functional is similar to the one for the far-field. Here, Ω_m is an annulus around the antenna with $r_i = 140nm$ and $r_o = 180nm$ as

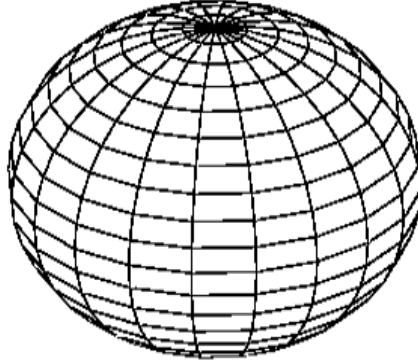


Figure 4.3: B-spline mesh over the upper arm of the nano antenna consisting of two spherical gold particles

radii of the inner and the outer spheres centered at the middle point of the gap area.

Figure 4.2b shows the absolute value of the electric field distribution at the wavelength $\lambda = 640nm$ with incident field $\mathbf{E}_i = \exp(jk_0x) \hat{z}$ (where k_0 is the wavenumber of free space and \hat{z} is the unit vector in z direction). The finite element method used to solve Maxwell's equations employs 653296 degrees of freedom (DoFs). Since the structure is symmetric, we investigate the sensitivity only over sph-1. The surface of sph-1 is covered by a B-spline mesh as shown in Figure 4.3. 1427 B-splines are located on vertices of the mesh. To derive the representative function g , we use a finite element mesh with 1971 DoFs over the surface of sph-1.

Figures 4.4a and 4.4b show the relative sensitivity $\left| \frac{g}{\mathcal{J}} \right|$ over the surface of sph-1 from bottom view and top view, respectively. As it is obvious from Figure 4.4, the bottom part of the sphere, which is in the gap area of the antenna, is more sensitive than the upper part. This means that perturbations in the gap area affect significantly the near field.

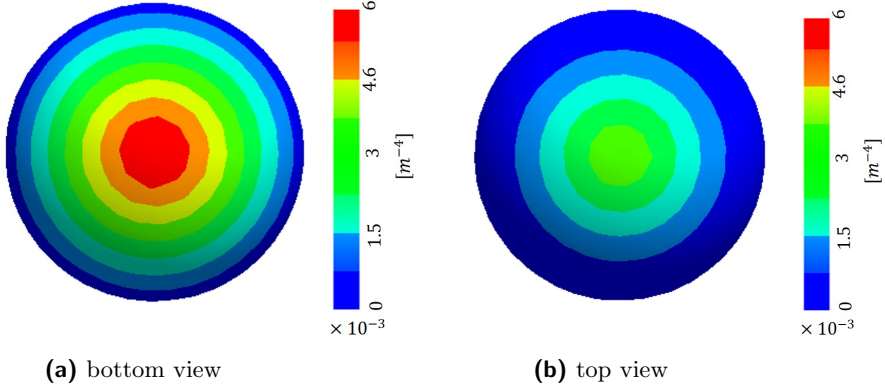


Figure 4.4: (a) The relative sensitivity representative $|\frac{g}{J}|$ over the upper arm of the antenna consisting of two spherical gold nano particles. The output functional measures the energy flux of the near-field data within an annulus around the antenna.

4.5.2 Nano antenna consisting two rectangular blocks in free space

In the second experiment, we repeat similar simulations for an antenna made of two rectangular gold blocks, brick-1 and brick-2 (see Figure 4.5a).

In our simulations we consider $\lambda = 770nm$, and $\mathbf{E}_i = \exp(ik_0(\sin(\frac{\pi}{3})x - \cos(\frac{\pi}{3})z)) \hat{y}$ (where \hat{y} is the unit vector in the direction y). The finite element method used to solve Maxwell's equations employs 604595 DoFs. Similar to the previous example, we perform the sensitivity analysis only on one of the arms of the antenna brick-1.

The B-spline mesh (see Figure 4.6) exploits 1166 B-splines over the surface of brick-1, and the finite element mesh used to discretize g has 1811 DoFs.

We solved the problem for both near-field and far-field functionals. The near-field integration region Ω_m in Equation (4.22) is shown as a region in light blue in Figure 4.5a. The far-field integration region Ω_f is the domain between two spheres with $r_i = 140nm$ and $r_o = 180nm$ as radii of the inner and the outer spheres, respectively. Figure 4.7 shows $|\frac{g}{J}|$ for both near-field and far-field functionals over the brick-1. Similar to the antenna

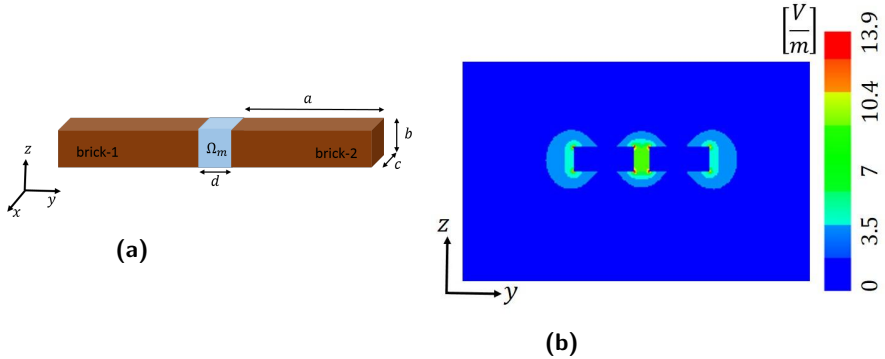


Figure 4.5: (a) Gold nano antenna consisting of two brown rectangular-blocks with dimensions $(a, b, c, d) = (98.5, 40, 40, 25) \text{ nm}$. The blue domain in the gap area Ω_m shows the near-field integration region. (b) The absolute value of the electric field distribution at $\lambda = 640 \text{ nm}$.

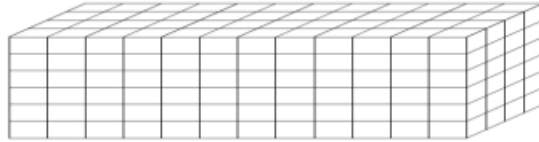


Figure 4.6: B-spline mesh over the right arm of the nano antenna consisting of two rectangular blocks.

consisting of two spheres, both near-field and far-field functionals are the most sensitive to changes in the left side of the brick-1 where is closer to the gap. An interesting observation is that the far-field functional, unlike the near-field one, is less sensitive to perturbations of edges and corners. This means that despite the high field localization around corners, they do not have significant effect on the far-field pattern, whereas the near-field is highly affected by their shape.

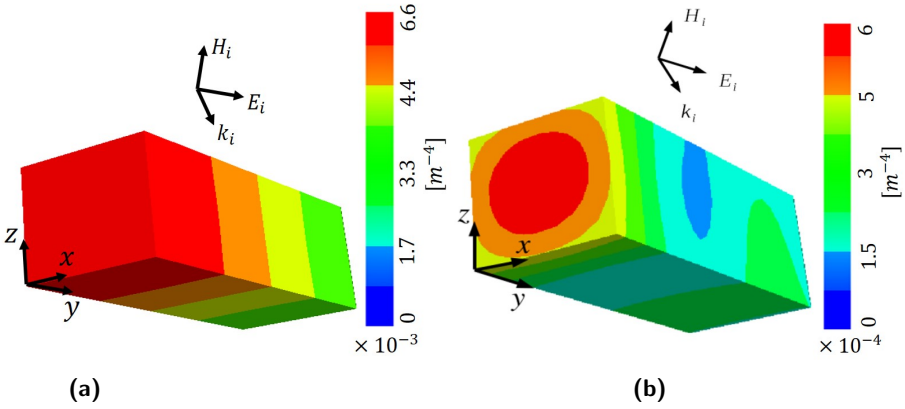


Figure 4.7: The relative sensitivity representative $|\frac{g}{J}|$ of (a) near-field (b) far-field functionals over the right arm of the gold nano antenna consisting of two rectangular blocks.

4.5.3 Nano antenna consisting two rectangular blocks over a substrate

To see the effect of a substrate on g , we mount the antenna consisting of two rectangular blocks on a glass substrate located at $z < 0$ with the refractive index $n_2 = 1.5$ (see Figure 4.8a). The size of the antenna, the wavelength, and the incident field are the same as those in the previous experiment. Let Γ_s be the face of brick-1 which touches the substrate. Probing functions located on Γ_s perturb the surface of the substrate as well. This means that the part of the substrate surface which is touching the antenna is no longer flat after deformations.

The sensitivity representative function over the surface of brick-1 for the far-field functional is shown in Figure 4.8b. As one can see, the presence of the substrate causes g to increase on Γ_s . In other words, the output functional becomes more sensitive to the shape of Γ_s .

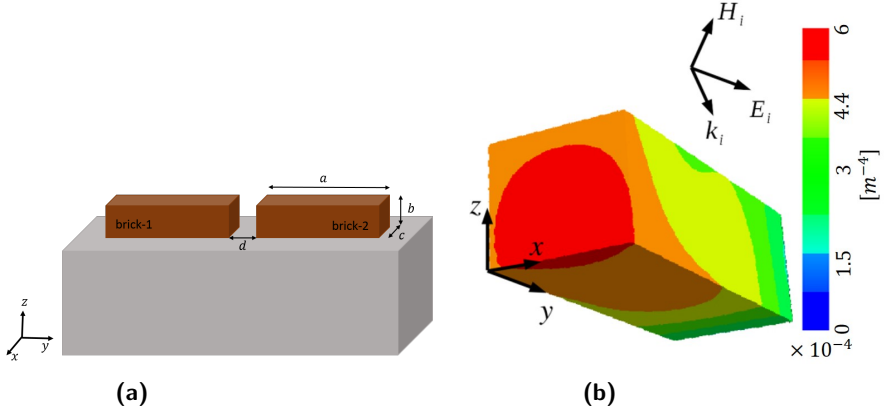


Figure 4.8: (a) Gold nano antenna consisting of two rectangular particles with dimensions $(a, b, c, d) = (98.5, 40, 40, 25)nm$ on a glass substrate with refractive index $n_2 = 1.5$. (b) The relative sensitivity representative $|\frac{g}{J}|$ over brick-1. The output functional measures the energy flux of the far-field.

4.5.4 Nano antenna consisting two rectangular blocks with displaced arms

Now, we displace brick-2 by $\Delta x = 20nm$ in the \hat{x} direction (see Figure 4.9a). The size of the antenna, the incident field, the working frequency, the output functional, and the material of the substrate are the same as those in the previous experiment. As shown in Figure 4.9b, the relative sensitivity profile is also displaced in the direction \hat{x} . Which means the position of the antenna gap and the substrate are key elements in forming the sensitivity representative for nano antennas.

4.5.5 Nano antenna consisting two rectangular blocks with gap along the longer edge

For further experiments, we change the direction of the gap and put it along the longer edge of bricks (see Figure 4.10). Dimensions, excitation, B-spline

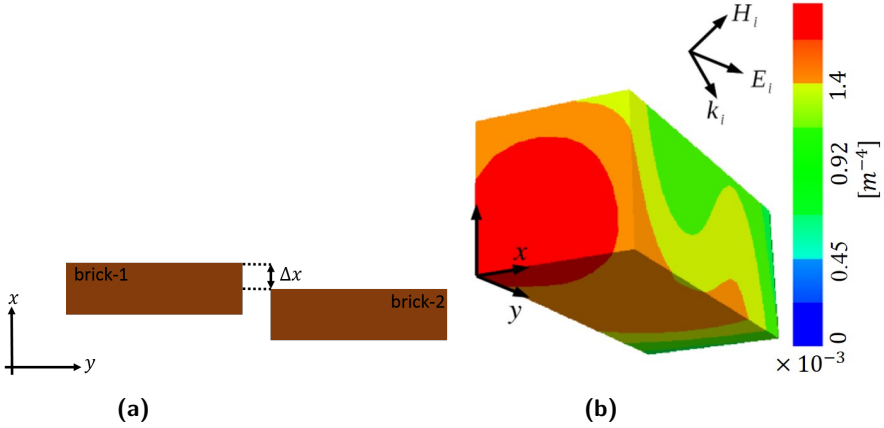


Figure 4.9: (a) Gold nano antenna, consisting of two rectangular blocks, with left arm displaced in \hat{x} direction. The dimensions are $(a, b, c, d) = (98.5, 40, 40, 25)nm$, and $\Delta x = 20nm$. The substrate material is glass with refractive index $n_2 = 1.5$. (b) The relative sensitivity representative $|\frac{\partial g}{\partial x}|$ over brick-1. The output functional measures the energy flux of the far-field.

mesh and mesh used for discretizing g are similar to those in previous experiments. The finite element mesh used to discretize the state and the adjoint problem has 631395 DoFs.

Figure 4.10b shows the sensitivity profile over the surface of brick-1. Similar to previous results the face which is closer to the gap area is the most sensitive part of the antenna.

4.5.6 Groove antenna

We now repeat the previous experiment by making a short circuit between two arms of the antenna and generating a V-groove nano-particle (see Figure 4.11a)[62]. The dimension of the antenna is $(a, b, c) = (50, 150, 10)nm$ and $(d_1, d_2, d_3) = (6, 6, 6)nm$. The material of the nano-particle is silver, and the excitation wavelength is $\lambda = 500nm$. The optical constants of the silver at the given frequency is obtained using the data provided by [39]. The nano-particle is mounted on a glass substrate with $n_2 = 1.5$. The incoming wave

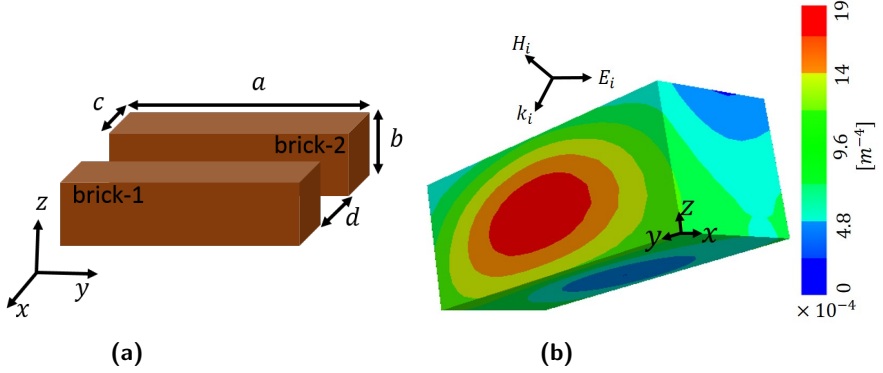


Figure 4.10: (a) Gold nano antenna, consisting of two rectangular blocks. The gap area is along the longer edge a . The dimensions are $(a, b, c, d) = (98.5, 40, 40, 25)nm$. The substrate material is glass with refractive index $n_2 = 1.5$. (b) The relative sensitivity representative $|\frac{dJ}{dz}|$ over brick-1. The output functional measures the energy flux of the far-field.

is similar to the incident field in previous experiments. The finite element method used to solve Maxwell's equations employs 901860 DoFs.

The experiment investigates the sensitivity of far-field functional (4.8). The B-spline mesh consists of 1225 B-splines over the surface of the groove $\partial\Omega_s$. To discretize g over $\partial\Omega_s$, we exploit a finite element discretization with 3862 DoFs. Figure 4.11b shows the normalized sensitivity profile over the surface of the groove. As we were expecting, the area around the channel is the most sensitive part. Based on [62], the V-groove behaves like a waveguide based on Channel Plasmon Polariton (CPP) effect. The end parts of the channel have less effect on the far-field pattern.

4.5.7 Silver brick

To see the effect of the channel on the sensitivity profile of the V-groove, we remove the channel and simulate the single brick (see Figure 4.12a). The dimensions and the excitation of the brick are the same as the V-groove waveguide. The finite element mesh to solve the state and the adjoint

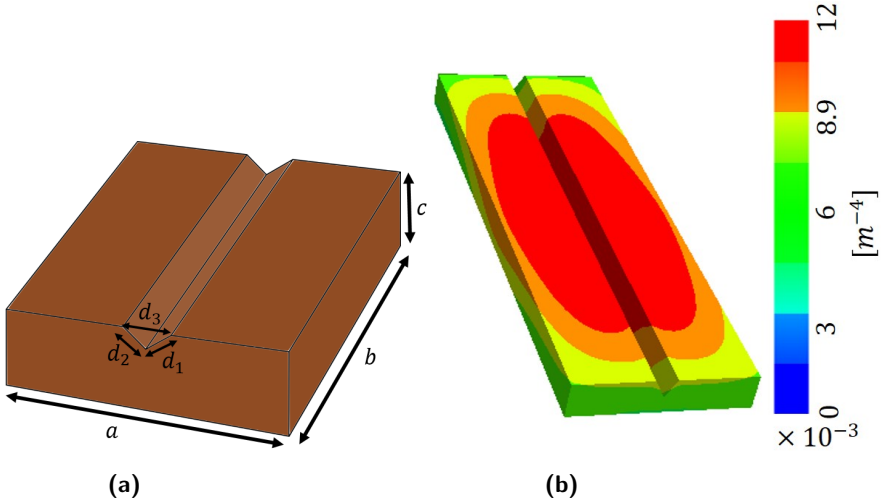


Figure 4.11: (a) The silver V-groove waveguide. The dimensions are $(a, b, c) = (50, 150, 10)nm$ and $(d_1, d_2, d_3) = (6, 6, 6)nm$. The substrate material is glass with refractive index $n_2 = 1.5$. (b) The relative sensitivity representative $|\frac{g}{J}|$ over the V-groove. The output functional measures the energy flux of the far-field.

problems has 469405 DoFs. The B-spline mesh consists of 1116 B-splines and the finite element mesh to discretize g over the surface of the brick has 3646 DoFs. As depicted in Figure 4.12b, the far-field pattern is mostly sensitive to the central part of the brick. In the V-groove experiment, the sensitivity representative g is extended along a greater distance over the upper face of the brick. This can be due to the waveguiding characteristic of the channel.

The effect of the finite element mesh on the sensitivity pattern is investigated in the next experiment. We repeat the previous experiment using two finer meshes with 886890 and 1163595 DoFs to discretize the state and the adjoint problems. We keep all the other settings the same as in the previous experiment. As shown in Figure 4.13, the sensitivity representative is not affected significantly by the mesh resolution.

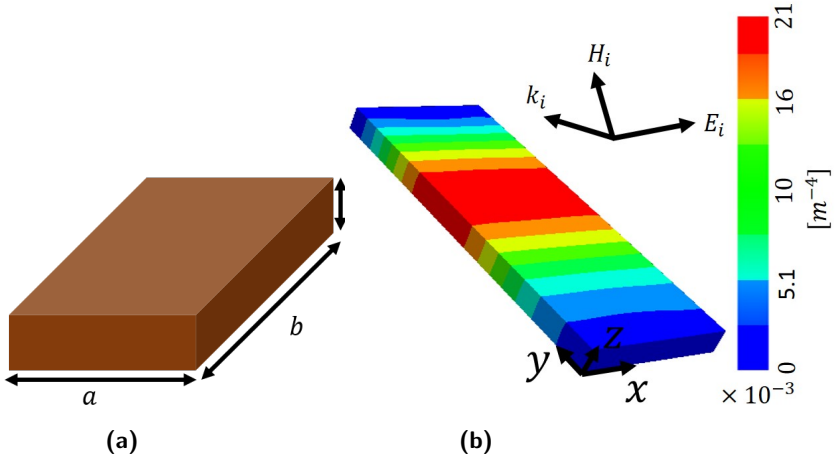


Figure 4.12: (a) The silver brick. The dimensions are $(a, b, c) = (50, 150, 10)nm$. The substrate material is glass with refractive index $n_2 = 1.5$. (b) The relative sensitivity representative $|\frac{dJ}{dg}|$ over the silver brick. The output functional measures the energy flux of the far-field.

The effect of the B-spline mesh resolution on g is investigated in the last experiment. We increase the number of B-splines to 2126, and use the finite element mesh with 469405 DoFs to solve state and adjoint problems. Based on the result shown in Figure 4.14, the sensitivity pattern remains almost the same when increasing the number of B-splines.

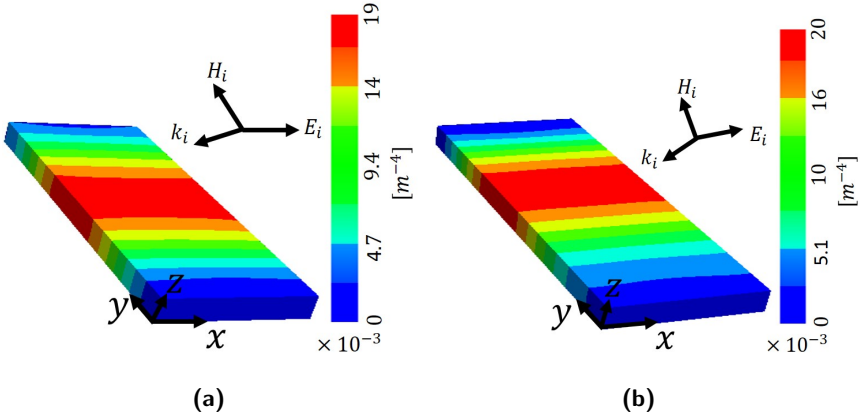


Figure 4.13: The relative sensitivity representative $|\frac{g}{J}|$ over the silver brick obtained using meshes with (a)886890, and (b)1163595 DoFs. The number of B-splines used to investigate the sensitivity is 1116. The output functional measures the energy flux of the far-field.

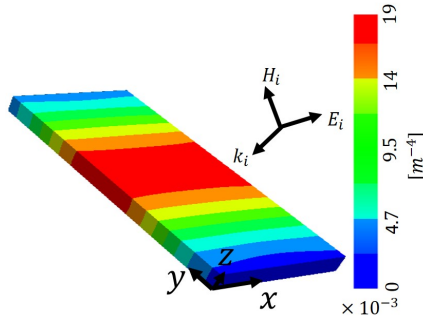


Figure 4.14: The relative sensitivity representative $|\frac{g}{J}|$ over the silver brick. The number of B-splines used to investigate the sensitivity is 2126. The finite element mesh used to solve state and adjoint problems has 469405 DoFs. The output functional measures the energy flux of far-field.

4.6 Conclusion

In this chapter we used the shape gradient formula obtained in Chapter 3 to find a sensitivity representative function over the surface of the structure. B-Splines were used to deform the object locally.

Several numerical experiments were lunched to investigate the shape sensitivity of different plasmonic nano antennas. Based on the obtained results, the gap area is the most sensitive part, which means small perturbations introduced in this region affects the performance of the nano-particle significantly.

Shaping edges and corners is one of the main challenges during fabrication process. However, our results showed that the far-field functional is not highly sensitive to the shape of corners and edges.

The presence of a substrate is also another issue that can affect the sensitivity of the particle. We also showed that the far-field pattern gets more sensitive to perturbations of the face touching the substrate.

5 Conclusion

5.1 Summary

In this dissertation, we have investigated the sensitivity of the performance of plasmonic nano-particles with respect to fabrication-based perturbations. The Maxwell equations were solved numerically using NGSolve, a C++ library based on finite elements method.

The performance of optical nano-particles is usually measured by field values at far distances. Near-field to far-field mapping is a technique to indirectly evaluate the values of electromagnetic fields at far distances. For objects located in free space there is a closed formulation. The procedure gets more challenging for layered media and had remained unsolved for a long time. In Chapter 2, we presented a rigorous asymptotic study for the Green's function in semi-infinite half space, and we derived a closed form far-field mapping technique. The mapping can be expressed either as a volume integration or as a boundary integration. It is advisable to use the volume integration when the finite element method is used. Our numerical experiments also show a very good agreement with other methods.

To investigate the sensitivity of the far-field or of any other output functional with respect to the shape of the structure, one needs to do shape sensitivity analysis. Shape calculus is a technique to obtain the shape gradient of an output functional with respect to the shape of the domain. The shape gradient of shape differentiable PDE constrained shape functionals can be expressed either as an integration over the volume or as an integration on the boundary. In Chapter 3, we derived both formulations for scalar second order elliptic problems with Dirichlet and Neumann boundary conditions. Theorems in Section 3.4 and numerical experiments in Section 3.5 confirm that it is advisable to evaluate the shape gradient through volume integrals, when the finite element method is used. We also investigated the

derivation of the shape gradient for 3D scattering problems. Since electromagnetic fields are vectors, the procedure gets rather complicated. Given that the solution of the state problem is complex valued whereas the shape functional is real valued, we used the generalized Lagrangian approach to find the shape gradient. Covariant transformations were used to map from the reference domain to the perturbed domain. Based on theorem 9, the formulation based on volume integrals for Maxwell problem also enjoys superb convergence, i.e. the error decays as h^2 . We investigated the proof by extensive employment of duality technique.

In Chapter 4, we used shape gradients obtained for Maxwell's equations to perform sensitivity analysis. To perturb the domain locally, we used tensor product B-splines. In the end, we derived a sensitivity representative function over the surface of the scatterer based on local sensitivity measurements. Various numerical experiments were conducted to investigate the sensitivity of different nano particles located in free-space or on the substrate. Numerical experiments, showed that the far-field pattern of nano-antennas is highly sensitive to the gap area. The sensitivity profile changes significantly if we displace the gap. Another interesting observation was that the presence of the substrate in the structure affects the sensitivity profile. The far-field pattern gets more sensitive to the face of the antenna touching the substrate. Based on our results, perturbations on corners or along edges do not change far-field significantly.

5.2 Outlook

The research carried out under the scope of this dissertation can be continued in several directions. Some ideas are described here

- Conducting numerical experiments based on Maxwell's equations to compare convergence rates of volume-based and boundary-based shape gradients. We expect that the results of numerical experiments also verify the faster convergence of the volume-based approach.
- Performing shape optimizations for 3D electromagnetic scattering problems based on shape gradients obtained in Chapter 3. To achieve a better performance for optical components, a concrete 3D optimization is advantageous.

- It will be interesting to insert the shape gradients obtained in Chapter 3 into the shape optimization algorithm explained in [33].

List of Figures

1.1	Lycurgus cup (British Museum [26]) which is made by adding nano particles of gold and silver to the glass. Due to the interaction of light with tiny metal nano particles, the color of the glass changes under the natural light illumination. . . .	1
1.2	Magnified SEM images of four particles with different observation angles [59].	5
1.3	Domain definition for the scattering problem.	8
2.1	Integration contour in the complex k_ρ plane (avoiding singularity of Hankel function).	17
2.2	Integration contour in the complex w plane, avoiding the branch cut singularity of Hankel function.	18
2.3	Dipole located over a semi-infinite dielectric domain.	19
2.4	TM wave incidence on a semi-infinite dielectric half space. $(\mathbf{E}^i(\mathbf{r}), \mathbf{H}^i(\mathbf{r}))$, $(\mathbf{E}^r(\mathbf{r}), \mathbf{H}^r(\mathbf{r}))$, and $(\mathbf{E}^t(\mathbf{r}), \mathbf{H}^t(\mathbf{r}))$ are the incident, reflected, and transmitted fields, respectively.	20
2.5	Integration path in the complex k_ρ plane for a (a) loss-less (b) lossy material.	24
2.6	Different choices of branch cuts in the complex k_ρ plane. (a) Branch cuts are along $\text{Im } k_{z_1} = 0$. So, $\text{Im } k_{z_1} > 0$ on the entire top Riemann sheet, $\text{Re } k_{z_1} > 0$ on unshaded regions, $\text{Re } k_{z_1} < 0$ on shaded regions. (b) Branch cuts are along $\text{Re } k_{z_1} = 0$. So, $\text{Re } k_{z_1} > 0$ on the entire top Riemann sheet, $\text{Im } k_{z_1} > 0$ on shaded regions, $\text{Im } k_{z_1} < 0$ on unshaded regions.	25
2.7	Integration path in the complex (a) k_ρ plane (b) w plane goes around branch cuts to avoid singularities and to guaranty that integrands are analytic.	26

2.8	The scatterer Ω_s is shown as a shaded region bounded by $\partial\Omega_s$. The integral in (2.32) is calculated over the contour Γ	27
2.9	Integration contours in the complex w plane. \bar{P}_s is the steepest descent path (SDP).	30
2.10	Integration contours in the complex w plane. w_b is the branch point and \bar{P}_b surrounds the branch cut.	33
2.11	Volume-based far-field integration region.	40
2.12	A typical solution domain used to model scattering problems.	42
2.13	An electric dipole located at $z' = 0.5\lambda$, perpendicular to the substrate. $\frac{\epsilon_1}{\epsilon_0} = 1$ and $\frac{\epsilon_2}{\epsilon_0} = 2$ are the relative permittivities for $z > 0$ and $z < 0$, respectively. (a) The finite element solution to the electric field component in the \hat{x} direction. (b) The far-field pattern for $\phi = 0$ and $0 < \theta < \frac{\pi}{2}$	49
2.14	Comparison of the far-field pattern calculated within two different finite element meshes. The electric dipole is perpendicular to the substrate ($\frac{\epsilon_1}{\epsilon_0} = 1$ and $\frac{\epsilon_2}{\epsilon_0} = 2$).	50
2.15	The far-field pattern calculated using three different integration regions. Integration domains are annuli with inner radius r_i and the outer radius r_o . The electric dipole is perpendicular to the substrate ($\frac{\epsilon_1}{\epsilon_0} = 1$ and $\frac{\epsilon_2}{\epsilon_0} = 2$), and the mesh has 226246 DoFs.	51
2.16	An electric dipole in free-space, located at $z' = 0.5\lambda$ and oriented in direction \hat{z} . (a) The finite element solution to the electric field component in the \hat{x} direction. (b) The far-field pattern for $\phi = 0$ and $0 < \theta < \frac{\pi}{2}$	52
2.17	(a) Cylindrical nanoparticle mounted on a glass substrate with (b) 3 principal axes a , b , and h	53
2.18	Skin depth of gold.	54
2.19	The absolute value of the scattered field of a cylindrical NP with elliptical footprint $(a, b, h) = (132, 95, 110)nm$. The incident electric field is parallel to (a) a-axis (b) b-axis.	54
2.20	Normalized energy flux of a cylindrical NP with an elliptical footprint $(a, b, h) = (132, 95, 110) nm$. The incident electric field $\mathbf{E}^i(\mathbf{r})$ is either parallel to the a -axis or b -axis. The measurement results are obtained from [27, Figure 3.1].	55

2.21	Normalized energy flux of a cylindrical NP with an elliptical footprint (a) $(a, b, h) = (132, 132, 110)$ nm and (b) $(a, b, h) = (132, 160, 110)$ nm. The incident electric field $\mathbf{E}^i(\mathbf{r})$ is either parallel to the a -axis or b -axis.	56
2.22	Normalized energy flux of a cylindrical NP with elliptical footprint $(a, b, h) = (132, 95, 110)$ nm calculated (a) using different databases for optical constants of gold (b) by lenses with different opening angle (α) and centered at different angles with respect to the z -axis (β)	57
2.23	Dependence of the resonance frequency on the size of principal axis. The footprint is elliptical and $(a, b, h) = (80 : 190, 120, 20)$ nm. The incident electric field is parallel to (a) b -axis and (b) a -axis. The measurement results are from [27, Figure 6.1].	58
3.1	The general setting of electromagnetic scattering problem. The far field integration region Ω_f is shown in orange. The outer region shown in white is Ω_o , and by Ω_i we denote the interior part which consists of blue and gray regions. The scatterer is depicted by gray color.	71
3.2	Plot of the solution u of the state problem in the computational domain Ω for the (a) first and the (b) second numerical experiment.	97
3.3	Convergence study for the (a) first and the (b) second numerical experiment. Obviously, Formula (3.8) is better suited for a finite element approximation of the Eulerian derivative $d\mathcal{J}(\Omega; \mathcal{V})$ than Formula (3.23).	98
3.4	(a) Plot of the solution u of the state problem in the computational domain Ω for the third numerical experiment, and (b) corresponding convergence study. Due to the poor regularity of the functions u and p , the convergence rate of $d\mathcal{J}(\Omega, u_h, p_h; \mathcal{V})^{\text{Vol}}$ and $d\mathcal{J}(\Omega, u_h, p_h; \mathcal{V})^{\text{Bdry}}$ deteriorate.	99
3.5	Plot of the solution u of the state problem in the computational domain Ω for the (a) fourth and the (b) fifth numerical experiment.	99

3.6	Convergence study for the (a) fourth and (b) fifth numerical experiment. The quadratic convergence of $d\mathcal{J}(\Omega, u_h, p_h; \mathcal{V})^{\text{Bdry}}$ is unexpected.	100
3.7	(a) Plot of the solution u of the state problem in the computational domain Ω for the sixth numerical experiment, and (b) corresponding convergence study. Due to the poor regularity of the functions u and p , the convergence rate of $d\mathcal{J}(\Omega, u_h, p_h; \mathcal{V})^{\text{Vol}}$ and $d\mathcal{J}(\Omega, u_h, p_h; \mathcal{V})^{\text{Bdry}}$ deteriorate.	101
3.8	Convergence study for the (a) first, (b) second, (c) third, (d) fourth, (e) fifth and (f) sixth numerical experiment, when considering the operator norm <i>on the subspace of multivariate polynomials of degree two</i> . The results agree with those obtained with cubic polynomials.	102
4.1	Directions of B-splines assigned to \mathbf{r}_1 and \mathbf{r}_2 located on an edge and on a corner, respectively.	105
4.2	(a) Nano antenna consisting of two gold spheres with dimensions $(r_a, d) = (50, 23)nm$. (b) The absolute value of the electric field distribution at $\lambda = 640nm$	112
4.3	B-spline mesh over the upper arm of the nano antenna consisting of two spherical gold particles	113
4.4	(a) The relative sensitivity representative $ \frac{g}{\mathcal{J}} $ over the upper arm of the antenna consisting of two spherical gold nano particles. The output functional measures the energy flux of the near-field data within an annulus around the antenna.	114
4.5	(a) Gold nano antenna consisting of two brown rectangular blocks with dimensions $(a, b, c, d) = (98.5, 40, 40, 25)nm$. The blue domain in the gap area Ω_m shows the near-field integration region. (b) The absolute value of the electric field distribution at $\lambda = 640nm$	115
4.6	B-spline mesh over the right arm of the nano antenna consisting of two rectangular blocks.	115
4.7	The relative sensitivity representative $ \frac{g}{\mathcal{J}} $ of (a) near-field (b) far-field functionals over the right arm of the gold nano antenna consisting of two rectangular blocks.	116

4.8 (a) Gold nano antenna consisting of two rectangular particles with dimensions $(a, b, c, d) = (98.5, 40, 40, 25)nm$ on a glass substrate with refractive index $n_2 = 1.5$. (b) The relative sensitivity representative $|\frac{g}{\mathcal{F}}|$ over brick-1. The output functional measures the energy flux of the far-field. 117

4.9 (a) Gold nano antenna, consisting of two rectangular blocks, with left arm displaced in \hat{x} direction. The dimensions are $(a, b, c, d) = (98.5, 40, 40, 25)nm$, and $\Delta x = 20nm$. The substrate material is glass with refractive index $n_2 = 1.5$. (b) The relative sensitivity representative $|\frac{g}{\mathcal{F}}|$ over brick-1. The output functional measures the energy flux of the far-field. . 118

4.10 (a) Gold nano antenna, consisting of two rectangular blocks. The gap area is along the longer edge a The dimensions are $(a, b, c, d) = (98.5, 40, 40, 25)nm$. The substrate material is glass with refractive index $n_2 = 1.5$. (b) The relative sensitivity representative $|\frac{g}{\mathcal{F}}|$ over brick-1. The output functional measures the energy flux of the far-field. 119

4.11 (a) The silver V-groove waveguide. The dimensions are $(a, b, c) = (50, 150, 10)nm$ and $(d_1, d_2, d_3) = (6, 6, 6)nm$. The substrate material is glass with refractive index $n_2 = 1.5$. (b) The relative sensitivity representative $|\frac{g}{\mathcal{F}}|$ over the V-groove. The output functional measures the energy flux of the far-field. . 120

4.12 (a) The silver brick. The dimensions are $(a, b, c) = (50, 150, 10)nm$. The substrate material is glass with refractive index $n_2 = 1.5$. (b) The relative sensitivity representative $|\frac{g}{\mathcal{F}}|$ over the silver brick. The output functional measures the energy flux of the far-field. 121

4.13 The relative sensitivity representative $|\frac{g}{\mathcal{F}}|$ over the silver brick obtained using meshes with (a)886890, and (b)1163595 DoFs. The number of B-splines used to investigate the sensitivity is 1116. The output functional measures the energy flux of the far-field. 122

4.14 The relative sensitivity representative $\left| \frac{g}{J} \right|$ over the silver brick. The number of B-splines used to investigate the sensitivity is 2126. The finite element mesh used to solve state and adjoint problems has 469405 DoFs. The output functional measures the energy flux of far-field. 122

Bibliography

- [1] Traité de la lumière. *Journal of the Röntgen Society*, 16(65):151–151.
- [2] M. J. Ablowitz and A. S. Fokas. *Complex variables: Introduction and applications*. Cambridge University Press, 2003.
- [3] Allaire and Grégoire. *Conception optimale de structures*. Springer-Verlag, 2007.
- [4] A. Alparslan and C. Hafner. Layered geometry green’s functions in the multiple multipole program. *J. Comput. Theor. Nanosci.*, 8(8):1600–8, 2011.
- [5] E. A. Ash and G. Nichols. Super-resolution aperture scanning microscope. *Nature*, 237:510–512, 1972.
- [6] R. Becker and R. Rannacher. An optimal control approach to a *posteriori* error estimation in finite element methods. *Acta Numerica*, 10:1–102, 2001.
- [7] N. Bleistein. *Mathematical methods for wave phenomena*. Academic Press, 1984.
- [8] D. Bohm and D. Pines. A collective description of electron interactions. i. magnetic interactions. *Physical Review*, 82(5):625, 1951.
- [9] D. Bohm and D. Pines. A collective description of electron interactions: ii. collective vs. individual particle aspects of the interactions. *Physical Review*, 85(2):338, 1952.
- [10] D. Bohm and D. Pines. A collective description of electron interactions: iii. coulomb interactions in a degenerate electron gas. *Physical Review*, 92(3):609, 1953.

- [11] D. Braess. *Finite elements. Theory, fast solvers, and applications in elasticity theory*. Cambridge University Press, third edition, 2007.
- [12] D. Bucur and G. Buttazzo. *Variational methods in shape optimization problems*. Birkhäuser Boston Inc., 2005.
- [13] J. Cagnol, J. P. Marmorat, and J. P. Zolesio. Shape sensitivity analysis in the maxwell's equations. In *LECTURE NOTES IN PURE AND APPLIED MATHEMATICS*, pages 27–36, 2001.
- [14] I. R. Capoglu, A. Taflove, and V. Backman. A frequency-domain near-field-to-far-field transform for planar layered media. *IEEE Trans. Antennas Propag*, 60(4):1878–85, 2012.
- [15] N. Chaulet and H. Haddar. Electromagnetic inverse shape problem for coated obstacles. *Adv. Comput. Math*, 41(6), 2015.
- [16] W. C. Chew. *Waves and fields in inhomogeneous media*, volume 522. New York: IEEE press, 1995.
- [17] F. Collino and P. Monk. The perfectly matched layer in curvilinear coordinates. *SIAM Journal on Scientific Computing*, 19(6):2061–2090, 1998.
- [18] M. Costabel, M. Dauge, and S. Nicaise. Singularities of Maxwell interface problems. *M² AN*, 33(3):627–649, 1999.
- [19] O. Darrigol. *A history of optics from Greek antiquity to the nineteenth century*. Oxford University Press, 2012.
- [20] P. Day. *The philosopher's tree: a selection of Michael Faraday's writings*. CRC Press., 1999.
- [21] M. C. Delfour and J. P. Zolésio. *Shapes and Geometries. Metrics, analysis, differential calculus, and optimization*, volume 22. Society for Industrial and Applied Mathematics (SIAM), 2011.
- [22] K. Eppler. Boundary integral representations of second derivatives in shape optimization. *Discussiones Mathematicae, Differential Inclusions, Control and Optimization*, 20(1):63–78, 2000.

- [23] K. Eppler. Second derivatives and sufficient optimality conditions for shape functionals. *Control Cybernet.*, 29(2):485–511, 2000.
- [24] L. B. Felsen. *Radiation and scattering of waves*, volume 31. John Wiley and Sons, 1994.
- [25] H. Fischer and O. J. F. Martin. Engineering the optical response of plasmonic nanoantennas. *Optics express*, 16(12):9144–9154, 2008.
- [26] I. Freestone, N. Meeaks, M. Sax, and C. Higgitt. The lycurgus cup — a roman nanotechnology. *Gold Bulletin*, 40(4):270–277, 2007.
- [27] R. Giannini. *Shape dependence of LSPRs and their applications in nanoemitters*. Dissertation ETH No. 21936, Zurich, 2014.
- [28] D. J. Griffiths. *Introduction to electrodynamics*, volume 3. Prentice Hall, 1999.
- [29] H. Harbrecht. On output functionals of boundary value problems on stochastic domains. *Math. Methods Appl. Sci.*, 33(1):91–102, 2010.
- [30] R. F. Harrington and J. L. Harrington. *Field Computation by Moment Methods*. Oxford University Press, 1996.
- [31] J. Hecht. *City of Light, The Story of Fiber Optics*. Oxford University Press on Demand, 2004.
- [32] R. Hiptmair. Finite elements in computational electromagnetism. *Acta Numerica*, 11, 2002.
- [33] R. Hiptmair and A. Paganini. Shape optimization by pursuing diffeomorphisms. *Comput. Methods Appl. Math.*, 15(3):291–305, 2015.
- [34] R. Hiptmair, A. Paganini, and S. Sargheini. Comparison of approximate shape gradients. *BIT Numer Math*, 55:459–485, 2015.
- [35] R. Hiptmair and S. Sargheini. Scatterers on substrate: Far field formulas. *SAM-Report*, 2015-02, 2015.
- [36] K. Iizuka. History of optics. *In Engineering Optics*.

- [37] J. B. Jackson and N. J. Halas. Surface-enhanced raman scattering on tunable plasmonic nanoparticle substrates. *Proc. Nat. Acad. Sci. USA*, 101(52):17930–17935, 2004.
- [38] C. Jerez Hanckes and J. C. Nédélec. Asymptotics for helmholtz and maxwell solutions in 3d open waveguides. *Commun. Comput. Phys.*, 11(2):629–46, 2012.
- [39] P. B. Johnson and R. W. Christy. Optical constants of the noble metals. *Physical review B*, 6(12):4370–9, 1972.
- [40] E. C. Jordan and K. G. Balmain. *Electromagnetic Waves and Radiating Systems*. Prentice Hall, 1968.
- [41] K. L. Kelly, E. Coronado, L. L. Zhao, and G. C. Schatz. The optical properties of metal nanoparticles: The influence of size, shape, and dielectric environment. *The Journal of Physical Chemistry B*, 107(3):668–677, 2003.
- [42] A. Kirsch. The domain derivative and two applications in inverse scattering theory. *Inverse Problems*, 9(1):81–96, 1993.
- [43] K. Kreutz Delgado. The complex gradient operator and the cr-calculus. *arXiv preprint arXiv:0906.4835*, 2009.
- [44] D. C. Lindberg. *Theories of Vision from al-Kindi to Kepler*. University of Chicago Press, 1981.
- [45] J. C. Maxwell. *A treatise on electricity and magnetism*, volume 1. Clarendon Press, 1892.
- [46] S. McFee, J. Webb, and D. Lowther. A tunable volume integration formulation for force calculation in finite-element based computational magnetostatics. *IEEE Trans. Magnetism*, 24(1):439–442, 1988.
- [47] W. McLean. *Strongly Elliptic Systems and Boundary Integral Equations*. Cambridge University Press, Cambridge, UK, 2000.
- [48] P. Monk. *Finite element methods for Maxwell's equations*. Oxford University Press, 2003.

- [49] C. Müller. *Foundation of the mathematical theory of electromagnetic waves*, volume 155. Springer Science and Business Media, 2013.
- [50] J. D. Murray. *Asymptotic analysis*, volume 48. Springer Science and Business Media, 2012.
- [51] J. C. Nédélec. *Acoustic and electromagnetic equations: integral representations for harmonic problems*, volume 144. Springer Science and Business Media, 2001.
- [52] I. Newton. *Opticks: or, a treatise of the reflexions, refractions, inflexions and colours of light. Also two treatises of the species and magnitude of curvilinear figures*. London, Sam. Smith and Benj. Walford, 1704. Culture et civilisations, 1704.
- [53] S. Nie and R. N. Zare. Optical detection of single molecules. *Annual review of biophysics and biomolecular structure*, 26(1):567–596, 1997.
- [54] P. Nordlander and F. Le. Plasmonic structure and electromagnetic field enhancements in the metallic nanoparticle-film system. *Applied Physics B*, 84(1-2):35–41, 2006.
- [55] L. Novotny and B. Hecht. *Principles of nano optics*. Cambridge University Press, 2012.
- [56] E. D. Palik. *Handbook of optical constants of solids*, volume 3. Academic Press, Boston., 1998.
- [57] O. Pironneau. *Optimal shape design for elliptic systems*. Springer, 1982.
- [58] D. W. Pohl, W. Denk, and M. Lanz. Optical stethoscopy: Image recording with resolution $\lambda/20$. *Applied physics letters*, 44(7):651–653, 1984.
- [59] T. Sannomiya. *Optical biosensing based on localized surface plasmon resonance*. Dissertation ETH No. 18747, Zürich, 2009.
- [60] O. Scholder. *Fabrication, simulation and characterization of tunable plasmonic nano antennas*. Dissertation ETH No. 21847, Zürich, 2014.

- [61] J. Simon. Differentiation with respect to the domain in boundary value problems. *Numerical Functional Analysis and Optimization*, 2(7-8):649–687, 1980.
- [62] J. Smajic and C. Hafner. Plasmonic v-groove waveguides: building blocks for optical transistor. *Journal of Computational and Theoretical Nanoscience*, 7(8):1616–1622, 2010.
- [63] J. Sokolowski and J.-P. Zolésio. *Introduction to shape optimization: Shape sensitivity analysis*. Springer Ser. Comput Math, 1992.
- [64] A. Sommerfeld. Ueber die ausbreitung der wellen in der drahtlosen telegraphie. *Annalen der Physik*, 333(4):665–736, 1909.
- [65] A. Sommerfeld and E. G. Straus. *Partial differential equations in physics*. New York: Academic Press., 1964.
- [66] O. Steinbach. *Numerical Approximation Methods for Elliptic Boundary Value Problems-Finite and Boundary Elements*. Springer Science and Business Media, 2007.
- [67] E. H. Synge. A suggested method for extending the microscopic resolution into the ultramicroscopic region. *The London, Edinburgh, and Dublin Philosophical Magazine and Journal of Science*, 6(35):356–362, 1928.
- [68] C. E. Talley, J. B. Jackson, C. Oubre, N. K. Grady, C. W. Hollars, S. M. Lane, T. R. Huser, P. Nordlander, and N. J. Halas. Surface-enhanced raman scattering from individual au nanoparticles and nanoparticle dimer substrates. *Nano Lett.*, 5(8):1569–1574, 2005.
- [69] F. L. Teixeira, K. P. Hwang, W. C. Chew, and J. M. Jin. Conformal pml-fdtd schemes for electromagnetic field simulations: A dynamic stability study. *Antennas and Propagation, IEEE Transactions*, 49(6):902–907, 2001.
- [70] B. van der Pol and K. F. Niessen. über die ausbreitung elektromagnetischer wellen ueber einer ebenen erde. *Annalen der Physik*, 398(3).

- [71] H. Von Hoerschelmann. Ueber die wirkungsweise des geknickten marconischen senders in der drahtlosen telegraphie. *Konigl. Bayr. Ludwig-Maximilians-Universität zu München*, 1911.
- [72] T. Vosgröne, A. J. Meixner, A. Anders, H. Dietz, G. Sandmann, and W. Plieth. Electrochemically deposited silver particles for surface enhanced raman spectroscopy. *Surface Science*, 597(1):102–109, 2005.
- [73] H. Weyl. Ausbreitung elektromagnetischer wellen ueber einem ebenen leiter. *Annalen der Physik*, 365:481–500, 1919.
- [74] R. W. Wood. On a remarkable case of uneven distribution of light in a diffraction grating spectrum. *Proceedings of the Physical Society of London*, 18(1):269, 1902.
- [75] R. W. Wood. Diffraction gratings with controlled groove form and abnormal distribution of intensity. *he London, Edinburgh, and Dublin Philosophical Magazine and Journal of Science*, 23(134), 1912.
- [76] J. Zenneck. Fortpflanzung ebener elektromagnetischer wellen laengs einer ebenen leiterflaeche. *Annalen der Physik*, 23:848–866, 1907.

